Solar Monte Carlo Radiative Transfer Simulations in Saharan Dust Plumes

Dissertation
zur Erlangung des Doktorgrades
an der Mathematisch-Naturwissenschaftlichen Fakultät
der Christian-Albrechts-Universität zu Kiel
vorgelegt von

Dipl.-Math.
Antje Torge
Kiel, 2013

Referent: Prof. Dr. Andreas Macke
Korreferent: Prof. Dr. Manfred Wendisch

Tag der mündlichen Prüfung: 18.01.2013
Zum Druck genehmigt: 04.02.2013

gez. Prof. Dr. Wolfgang J. Duschl, Dekan

Abstract Radiative fields of three-dimensional inhomogeneous Saharan dust clouds have been calculated at solar wavelengths by means of a Monte Carlo radiative transfer model. Scattering properties are taken from measurements in the SAMUM campaigns, from light scattering calculations for spheroids based on the MISCHKA code, from Mie Theory for spheres and from the Geometric Optics Method assuming irregular shaped particles. Optical properties of particles with different projected area equivalent shapes are compared. Large differences in optical properties are found especially in the phase functions.
Modelled scattering properties are compared to laboratory measurements with good agreement.
Results of radiative transfer calculations based on the Monte Carlo Method are shown exemplarily for one dust cloud simulated by the cloud resolving atmospheric circulation model COSMO-MUSCAT.
Shape induced differences in the radiation fluxes are pronounced, for example, the domain averaged normalized radiance is about 20% lower in the case of a dust plume consisting of spheroids or irregular particles compared to spheres.
Further the modelled radiative fields are compared to simulated fields from COSMO-MUSCAT and to satellite measurements with the SEVIRI instrument onbord the MSG satellite. In some cases the patterns of the radiative fields agree quiet well, especially with the simulated fields from COSMO-MUSCAT. But because by uncertainties in particular in the input data, the modelled radiative fields do not agree very well with most of the satellite measured fields.
The satellite measurements are also used to compare with the measured radiances from an aircraft. There good agreements are found.
In the Monte Carlo radiative transfer calculations the horizontal photon transport can be switched of, which was used for investigations on its effect (3D-effect) on the reflected radiance fields. The 3D-effect is only notable at the largest gradients in optical thickness. For example, the reflectance at low sun position differs locally about 25% when horizontal photon transport is accounted for. 'Sharp edges' due to 1D calculations are smoothed out in the 3D case.

Zusammenfassung Die solaren Strahlungsfelder einer dreidimensionalen Saharastaubwolke wurden mit einem Monte Carlo Strahlungstransportmodellberechnet. Die benötigten Streueigenschaften wurden aus Messungen in den SAMUM Kampangen ermittelt und durch Lichtstreuberechnungen, für Spheroide basierend auf dem MISCHKA Code, für Kugeln mithilfe von Mie Theorie und mit der Methode der geometrischen Optik für irregulär geformte Teilchen ergänzt. Die optischen Eigenschaften von Partikeln mit unterschiedlichen Formen aber gleichen Projektionsflächen wurden verglichen und es wurden besonders in den Streufunktionen deutliche Unterschiede fest gestellt.
Modellierte Streueigenschaften wurden mit Labormessungen verglichen und gute Übereinstimmungen konnten festgestellt werden.
Die Ergebnisse der Strahlungstransportrechnungen mit der Monte Carlo Methode wurden exemplarisch für eine Staubwolke gezeigt, die vom Wolken auflösenden athmosphärischen Zirkulationsmodell COSMO-MUSCAT simuliert wurde.
Ausgeprägte forminduzierte Unterschiede in den Strahlungsflüssen sind beispielsweise in den normierten Strahldichten, die über das Modellgebiet gemittelt wurden, vorhanden. Bei einer Staubwolke aus elliptischen oder unregelmäßigen Teilchen sind diese ungefähr 20% kleiner als bei Staubwolken, die aus kugelförmigen Teilchen bestehen.
Weiterhin werden die modellierten Strahlungsfelder mit simulierten Feldern aus COSMO-MUSCAT und Satelliten-Messungen des MSG-Satelliten verglichen. Vor allen mit den den simulierten Strahlungsfeldern aus COSMO-MUSCAT stimmen die Monte Carlo modellierten Felder gut überein. Durch Unsicherheiten, insbesondere in den Eingabedaten, stimmen die modellierten Strahlungsfelder jedoch nicht sehr gut mit den vom Satelliten gemessenen Feldern überein.
Die Satelliten-Messungen werden auch verwendet, um sie mit den Radianzen aus Flugzeugmessungen zu vergleichen, wobei sich gute Übereinstimmungen ergaben.
In den Monte Carlo Strahlungstransportrechnungen kann der horizontale Photonentransport aus geschaltet werden. Dies wurde für Untersuchungen seines Einflusses (3D-Effekt) auf die reflektierten Strahldichtefelder eingesetzt. Der 3D-Effekt ist nur an den größten Gradienten der optischen Dicke relevant. Zum Beispiel unterscheidet sich das Reflexionsvermögen bei niedrigen Sonnenstand lokal um etwa 25%, wenn der horizontale Photonentransport berücksichtigt wird. "Scharfe Kanten" aufgrund der 1D Berechnungen werden in der 3D-Variante geglättet.

Contents

1 Introduction

1.1 Overview and aim of this work

The topic of this thesis is the simulation of the radiative transfer through a Saharan dust plume. Therefore a Monte Carlo model called MC-UniK (Macke et al. (1999)) is used. The Monte Carlo method is a statistical method to solve mathematical problems approximately, where analytical solutions are not available or too much effort is needed to get them. In radiative transfer the way of each photon is simulated, including each scattering and absorption process occurring when a photon interacts with a dust particle. To implement these simulations the modelled area was discretized into a three dimensional grid box. The COSMO-MUSCAT model (Heinold et al. (2011b)) provides particle size distributions for each grid box. COSMO-MUSCAT simulates the spatial and temporal distribution of dust particles in 5 size classes. (see chapter 2)
Based on the measurements at the field campaigns of SAMUM (Saharan mineral dust experiment, chapter 1.2) and with the help of several methods for different shaped particles, the scattering properties of spherical, spheroidal and irregular shaped particles are calculated. The methods are described in chapter 5 and there also the results are compared. These scattering properties are used as input for the 3D Monte Carlo radiative transfer simulations with the model MC-UniK. With MC-UniK the radiative fields were simulated with an observing angle corresponding to the view of the MSG satellite for better comparability.
One focus of this work was to look at the scattering properties of different shaped particles and the deviations they cause in the simulated radiative fields. Another point was to figure out how the horizontal photon transport affects the results of radiative transfer calculations in dust clouds. (chapter 6.3) Further the results of the calculations of the particle scattering properties are compared to laboratory measurements. (chapter 5.6) Also the simulated radiative fields are compared to the radiative fields measured by the SEVIRI instrument on board the MSG satellite. Some of the results in this thesis are already published in Torge et al. (2011).

1.2 The Saharan Mineral Dust Experiment - SAMUM

Dust research is a field where a wide variety of disciplines come together, including geomorphology, soil physics, meteorology, fluid dynamics, air chemistry and ocean biology. It has also involved diverse methodologies, ranging from field campaigns, Geographical Information System (GIS) analyses, remote sensing, numerical modelling, data assimilation as well as field and laboratory experiments. (Shao et al. (2011))
Therefore interdisciplinary research projects are funded. One of the biggest research campaigns on the topic of mineral dust is the SAMUM campaign. SAMUM stands for Saharan Mineral Dust Experiment. It was funded by the Deutsche Forschungsgesellschaft (DFG) and several German research institutes are involved in this project.
The aim of SAMUM is to understand the connections between the properties of the dust particles like their chemical composition, shape, size distribution and optical effects and thus the impact on radiative transfer through the dusty atmosphere. Feedbacks of radiative effects on dust emission and aerosol transport are also discussed.
Two field campaigns with the aim of gaining data to greate a detailed picture of a Saharan dust cloud were realized. The location of the field campaigns is pictured in figure 1. The first one took place in Morocco in 2006. This area is close to the Saharan desert and data of dust aerosol near the source regions were collected. The second field campaign in 2008 focused on the mixed desert dust with biomass burning aerosol at Cape Verde.
For the two campaigns a wide range of measurement equipment was used, like multi-wavelength Raman/polarization lidars and an airborne high spectral resolution lidar. Profiles of the particle size distribution, volume extinction coefficients or the particle shape sensitive optical properties at several wavelengths were measured. Field observations from ground-based stations, airborne measurement devices, and remote sensing, also with the help of satellite observations gave a comprehensive picture of the dust clouds.
These data were used to build up a dust cloud model which simulates the transport of the dust cloud through the model domain and in radiative transfer models whose results were compared to satellite measurements. (Heintzenberg (2009), Ansmann et al. (2011)) The last part is one focus of this study.

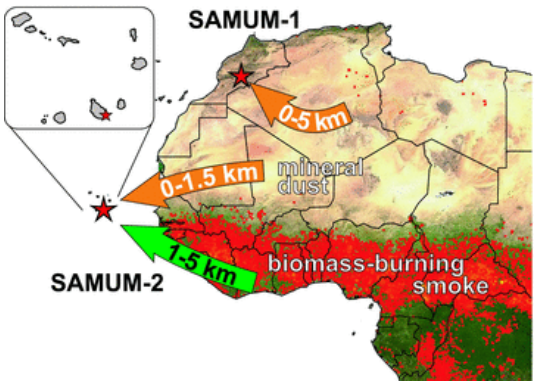

Figure 1: SAMUM-1 and SAMUM-2 field sites (stars) in southern Morocco and at Cape Verde. Pure dust conditions prevailed during SAMUM-1 with a dust layer from the surface to about 5km height above ground level (agl) advected from the Sahara (orange, 0−5km). In contrast, during SAMUM-2 (winter campaign) a shallow dust layer up to about 1.5km height agl (orange arrow, 0−1.5km) and an extended lifted aerosol layer from about 1−5km height agl (green arrow, 1−5km) consisting of biomass-burning smoke and mineral dust were frequently observed. The underlying fire map derived from MODIS observations (http://rapidfire.sci.gsfc.nasa.gov) shows all fires (red spots) detected during the 21-30 January 2008 period. (Ansmann et al. (2011))

1.3 The global dust cycle

A schematic view on the role of dust in the Earth system is given in figure 2 from Shao et al. (2011). Change in land use, changing climatological terms or meteorological conditions, for example, are influencing the global dust cycle. The main cycle starts with dust emission from an adequate dust source. Wind shear and turbulence lift the dust particles up and into the atmosphere. By turbulence and convection the dust is moved higher into the atmosphere. Further synoptic and global circulation are able to transport the dust plume over long distances. During their way the particles can react and mix with other airborne pollutants and influence atmospheric processes. The removal of the dust particles can occur by dry deposition when particles fall down by force of gravity or wet deposition caused by precipitation.

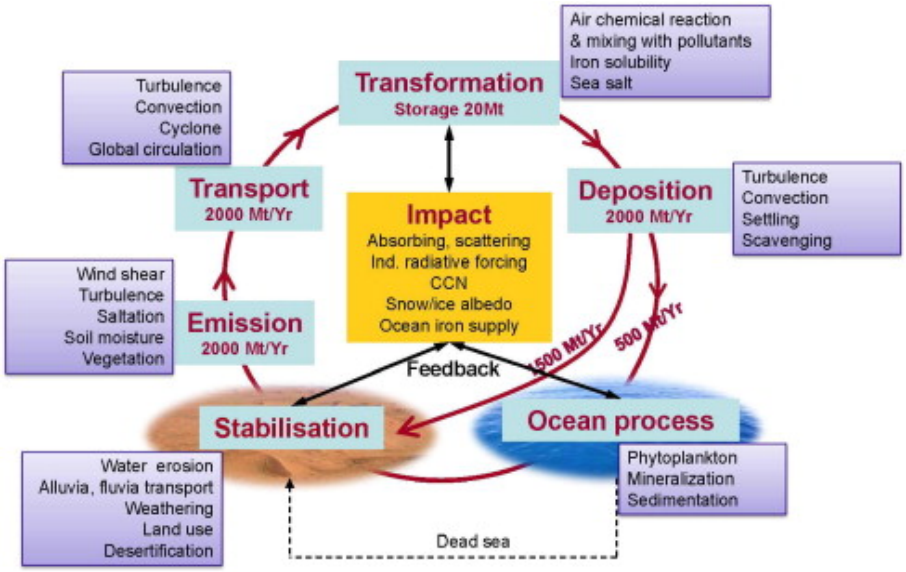

Figure 2: An illustration of the dust cycle in the Earth system and the main processes in which dust plays an important role. (Shao et al. (2011))

Figure 3: Satellite composite of the solar channels with a view on Africa (EUMETSAT)

Dust sources The properties of atmospheric dust are mainly defined by their size, shape and chemical composition which vary depending on dust source regions and the travelled distance. There are some very potential dust sources around the globe. Several studies deal with dust sources and some results are listed in Tanaka and Chiba (2006) and Shao et al. (2011). All listed studies agree that the main global dust source is the Sahara in North Africa. The Saharan dust contribution to the global dust emission is suggested by all compared studies around 50-70%.

Almost whole North Africa is covered by the Sahara (see figure 3). It is the world's largest warm desert and is with a size of 9 million km^2 round about as big as Europe. The Sahara was formed about 6000 years ago, since after a wet period in the mid Holocene dry conditions came up in North Africa. Proofs of earlier dry periods are strongly discussed. Some suggestions are 86,000 years ago (Schuster et al. (2006)) or more than 300,000 years ago (Kroepelin (2006)). There are even some indications for dry periods lying back more than 7 million years (Schuster et al. (2006)).

Before the dry period the Sahara was abundant with water and leafy, proofed by over 1000km long dried river beds (wadi). These wadis are preferential dust sources for aeolian dust. Also mineral resources like salt, coal, cooper, gold, mangan, iron, uran, lead, wolfram, titan, tin and phosphates can be found in the Sahara. They influence the dust composition. See figure 4 which shows the big variety of soil type.

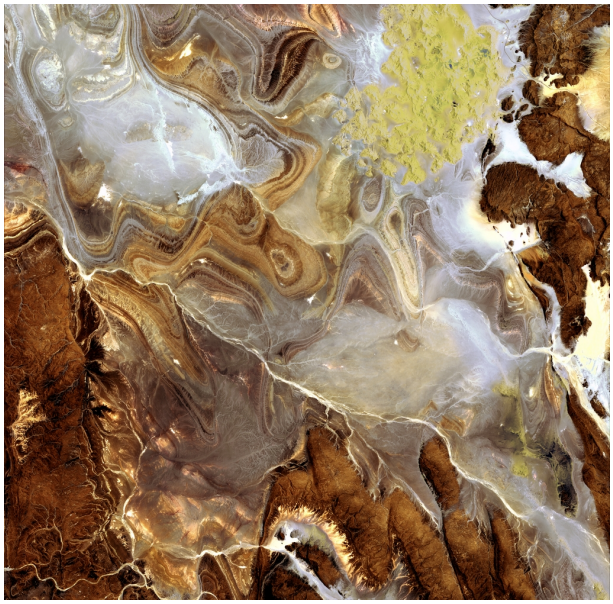

Figure 4: Tanezrouft Basin (land of terror) in Algeria. This region is characterized by dark sandstone hills, steep canyon walls, salt flats (white), stone plateaus, sandstone outcrop patterns of concentric loops and sprawling seas of multi-storey sand dunes known as ergs. Satellite: ALOS Instrument: AVNIR-2 Acquisition: 05-Mar-2009 Center coordinates: lat. 26.00, lon. 9.50 Credit: JAXA, ESA

Within the Sahara there is a special place, where most of the airborne dust originates; the Bodélé Depression in Chad. It is the largest single source of dust on Earth. Main reason for its productivity are special geological and meteorological conditions.
The Bodélé is surrounded on two sides by magmatic formations which lead and focus the surface winds towards the Bodélé (Koren et al. (2006)). It is a paleolake with an area of $133,532\text{km}^2$, possibly the largest Holocene freshwater lake on Earth. Only one part, which is now known as lake Chad still carries water.
$24,049\text{km}^2$ of the Bodélé are covered with the siliceous sediments of the dried lake bed as can be seen in figure 5. Diatomite can easily be powdered into a fine white substance consisting of particles in a size range for less than 1μm up to 1mm. The powder is very light an can easily be lifted up by wind. Thus in less than 2400 years up to 4m of sediment have been eroded from the Bodélé, that corresponds to a deflation rate of 1.4mm/yr. In the past 1000 years some $61,000\text{km}^3$ have been removed from the Bodélé Depression (Bristow et al. (2009)).

Lifting the dust up Surface winds have to exceed a the local threshold velocity to lift the dust particles into the atmosphere. Dust production arises from saltation or sandblasting, when soil grains are transported horizontally by winds as seen in figure 6. These processes depend on rainfall, wind, surface roughness, temperature, topography, and vegetation cover, which are independent factors linked to aridity and climate in a highly non-linear way.
Wind tunnel studies as seen in figure 7 show dust production to be proportional to the cube

Figure 5: Bodélé Depression covered with diatomite (Giles (2005))

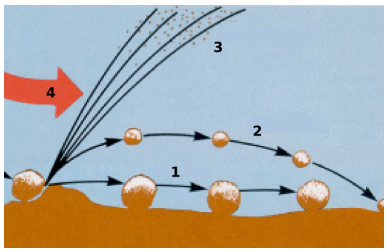

Figure 6: Internationalization of the diagram showing the mechanics of aeolian transport. 1 Creep 2 Saltation 3 Suspension 4 Wind current (Information Description Diagram showing the mechanics of w:saltation (geology). Source http : //exploration.nasa.gov/articles/06dec_dunes.html Date December 6, 2002 Author NASA Permission US Government, public domain)

of wind speed. (Jickells et al. (2005)) The most important processes leading to such surface wind speeds are the Nocturnal Low-Level Jet, the Mediterranean Cyclone and convective activity. The Nocturnal Low-Level Jet leads to maximum wind speeds in the lowest few kilometres of the atmosphere and occurs mainly at night-time. Also convective activity leading to haboobs is related to dust emission. In mountain areas occurs deep moist convection, what can lead to high surface wind speeds and can cause dust emissions. But also dry convection related to the Saharan heat low can cause dust source activation. (Schepanski et al. (2009))
In figure 8 a map of dust source activation of the Sahara is shown. The most active dust source is the Bodélé Depression (BO) indicated with yellow to orange color.

Figure 7: Saltating dune sand in a wind tunnel. (Photo credit: Wind Erosion Research Unit, USDA-ARS, Manhattan, Kansas)

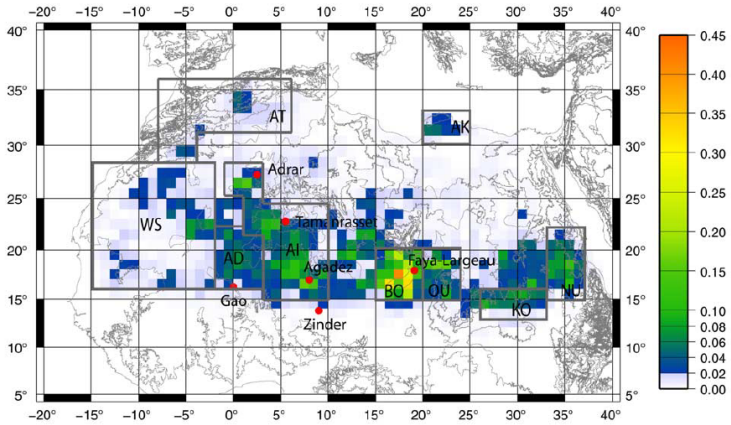

Figure 8: Fraction of dust source activations per day during March 2006 to February 2008 except August 2007 derived from MSG IR dust index. Red dots represent the location of synoptic stations considered. (Schepanski et al. (2009))

What happens with the aeolian dust in the atmosphere? Figure 9 shows the global pattern of dust transport. In the northern summer the Saharan dust comes mainly from the north-west and central-west parts and is transported to the Caribbean Sea and North America.

To the Amazon most dust gets transported in northern winter time originating from the south of the Sahara with the Bodélé depression.

About 25% of the Saharan dust emissions are transported to the Atlantic, 10% are going northward directed to Europe, 5% move westward to the Middle East and the main part of 60% is transported southward over the Sahel to the Gulf of Guinea.

The amount of transported dust varies with different large-scale climatic cycles such as El Niño Southern Oscillation and North Atlantic Oscillation (Prospero and Lamb (2003), Moulin and Chiapello (2004)).

Typically the dust transit through the atmosphere lasts from some hours to about a period of

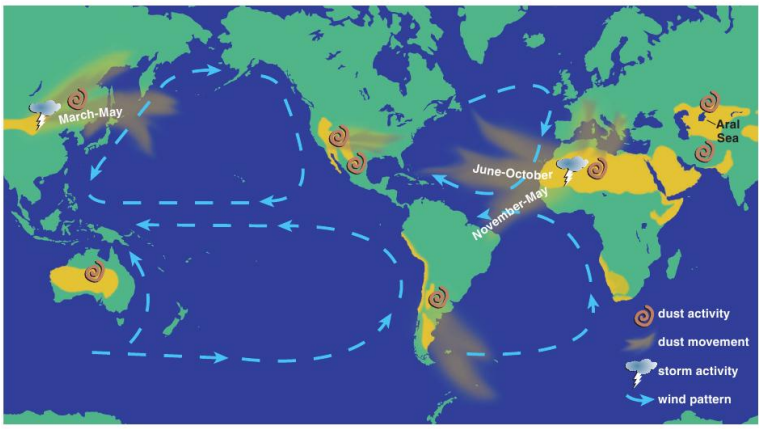

Figure 9: The world's arid regions (yellow) are the primary sources of the sediments in the Earth's atmosphere. (Griffin et al. (2002))

weeks. This long transport time is possible because it occurs at altitudes of several kilometres. (Prospero (1999), Jickells et al. (2005)) This allows long-range transport over distances of thousands of kilometres. In the pictures from figure 10 seasonal variations in dust transport can be constituted. In spring and summer, especially in the month June and July more dust is heading towards the Atlantic ocean. The formation, mixture and structure can vary substantially within one day, because of atmospheric dynamics and size dependend deposition. The majority of the airborne dust particles vary in size between $0.5-75\mu$m with a median diameter smaller than 10μm and the mean size being around 2μm. As the removal from the atmospheres by gravitation preferentially happens at larger particles, the size distribution shifts to smaller particles with transport distance.

Dust can be removed from the atmosphere by dry and wet deposition. The dust in altitudes of several kilometres is able to move over long distances without significant changes in size distribution. This long range transported dust is mainly removed by wet deposition caused by precipitation, several studies suggest a portion of wet deposition of 30 to 95%. Wet deposition rates changes with climatic conditions, particle size distribution, rainfall patterns and transport altitude. Thus there are big uncertainties in estimating the contribution of wet deposition to total deposition. (Shao et al. (2011)) The part of atmospheric dust deposited on land is about 75% and to the ocean about 25%. The local distribution of dust deposition is depicted in figure 11.

What are the impacts of dust in the atmosphere? In view of the IPCC report (Solomon et al. (2007)) aeolian dust is a big uncertainty in environmental research. Dust in the atmosphere can influence a variety of physical, chemical and bio-geochemical processes in the Earth system.
Many studies are dealing with the impact of mineral dust in the atmosphere. With the carried organic and mineral material it impacts visibility, climate, bio-geochemical processes, human

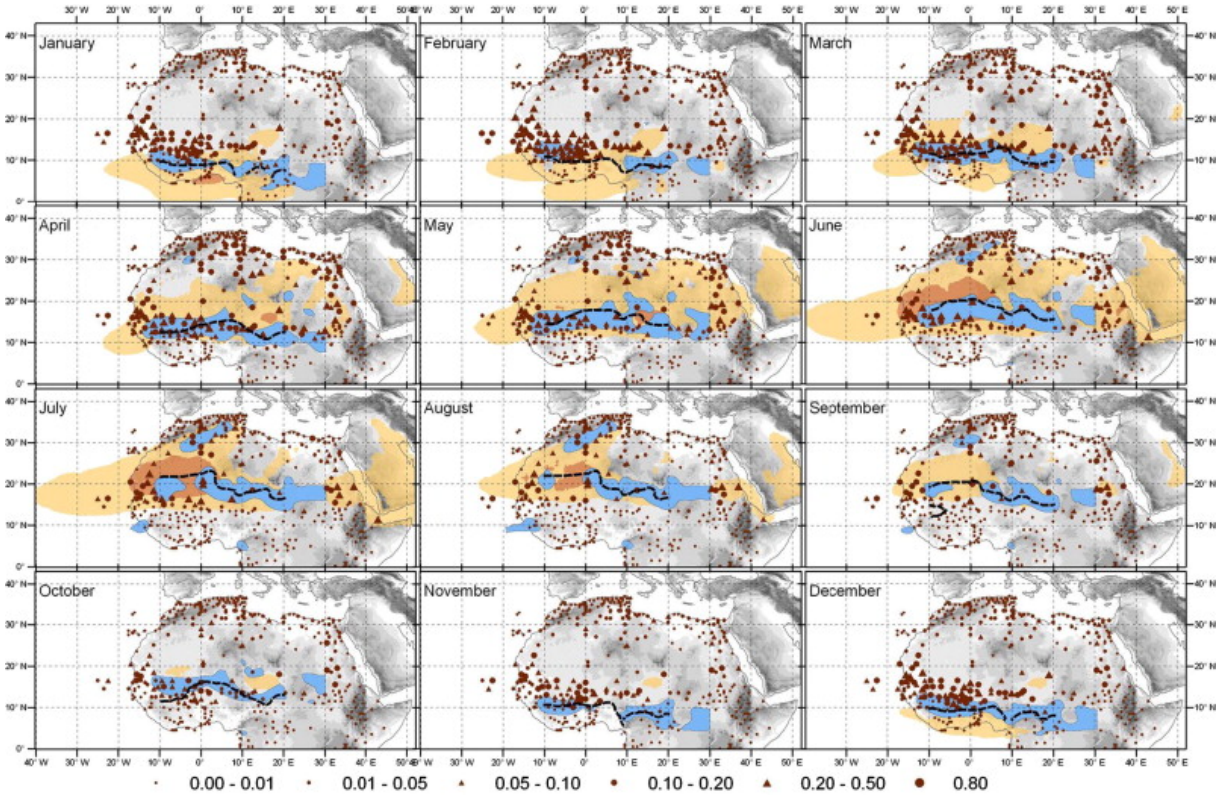

Figure 10: Relative frequency of dust events over the 26 year period from 1983 to 2008 calculated separately for individual months. The topographic height is shaded in black. Yellow and orange areas indicate regions of monthly averaged TOMS/OMI AI exceeding 1.8 and 3. (Shao et al. (2011))

health, the energy distribution in the atmosphere, the global radiation budget, the cloud life cycle, the formation of tropical cyclones, deep-sea sediments, precipitation, animals, vegetation and human health. (e.g. Tegen et al. (1996), Kaufman et al. (2005), Evan et al. (2006))

Radiation effects of dust clouds are important for modelling regional and global climate. The radiative effect of aerosols can be parted into two contributors, the direct and the indirect radiative effect.
Dust as an aerosol scatters and absorbs incoming solar radiation which is the direct radiative effect. The indirect radiative effect caused by dust is the modification of the optical properties of clouds like enhancing cloud reflectivity by increasing the number concentration of cloud droplets. A thin layer of dust on snow or ice surfaces can darken them and cause faster melting. (Solmon et al. (2008), Balkanski et al. (2006)) Thus dust profoundly affects the energy balance of the Earth system.
Estimates of the radiative forcing due to mineral dust vary widely from +0.09 to –0.46 Wm^{-2}. Even the sign of the radiative forcing is not well established due to the competing effects of solar and terrestrial radiative forcing. (Haywood and Boucher (2000))
The radiative forcing depends on the surface albedo, the presence of clouds and the dust

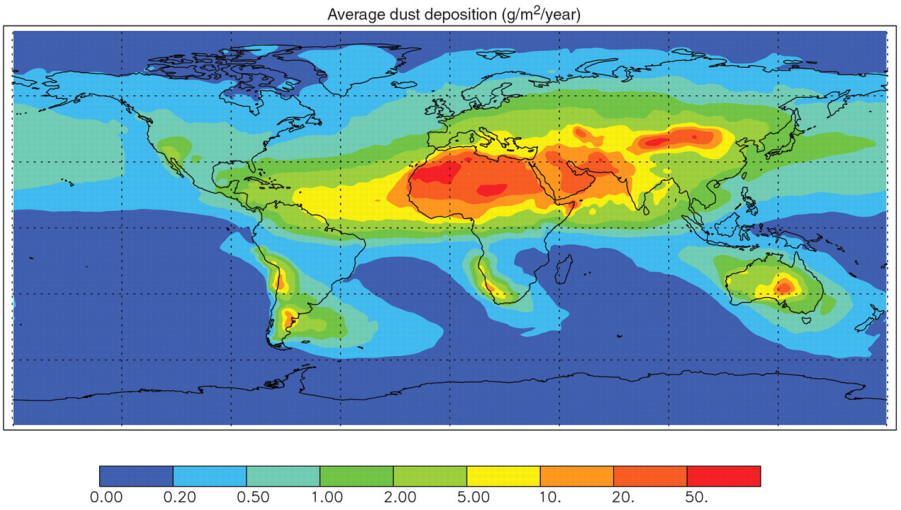

Figure 11: Total atmospheric dust inputs to the oceans: 450Tg/year. Percentage inputs to ocean basins based on this figure are as follows: North Atlantic, 43%; South Atlantic, 4%; North Pacific, 15%; South Pacific, 6%; Indian, 25%; and Southern Ocean, 6%. (Jickells et al. (2005))

spatial distribution and optical properties. Dust optical properties themselves depend on particle size distribution, particle shape and absorbing and scattering properties like the refractive index. Different measurements show that these factors are extremely variable and hence very difficult to represent in climate models. (Kandler et al. (2009))
The dust source mineralogy (iron oxide content), dust coating by absorbing aerosol (e.g. biomass burning), size distribution of particles and measurement techniques are all factors that contribute to the variability of observations.
Aerosols have a direct negative radiative forcing in the solar part of the spectrum which has a cooling effect on the climate system. They tend to scatter solar radiation and reflect it back into space instead of allowing it to pass through and reach Earth's surface. Its importance in the Earth system has been emphasized by the IPCC 4th Assessment Report (Solomon et al. (2007)) which highlighted the net global cooling effect of aerosols that in part compensates for the global warming effect of the greenhouse gases.
The dust from Africa carries viable micro-organisms, macro and micro nutrients, trace metals and some organic contaminants. Deposited in the ocean and on land, dust may play an important role in the complex changes in some ecosystems for example in coral reefs worldwide (Garrison et al. (2003), Griffin et al. (2001)).
Huge dust events create an atmospheric bridge over land and sea for bacteria, fungi, viruses and pollen. With the transport over the Atlantic additional marine micro-organisms aerosolized by wave action can be picked up. Uplifted bacteria are usually transported downwind less then one kilometre from their source, but within a dust cloud it can be transported over 5000km.
In contrast to the popular opinion that micro-organisms are rapidly killed by the solar UV-radiation, lack of nutrients and desiccation, heat, radiation and nutrient-poor conditions lots of bacteria and fungi survive with the protection from clouds, fog, smoke and desert dust

particles or they are highly pigmented which helps shield the microbes from UV radiation. Thus the possibility is given that big dust events enhancing the spread of plant and animal diseases. $5-25\%$ of the micro-organisms identified in African dust aerosols have the potential to be plant pathogens. (Kellogg and Griffin (2006)) In figure 12 some bacteria from a dust cloud can be seen.

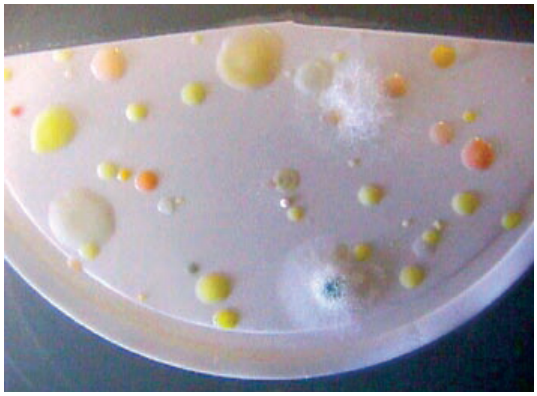

Figure 12: This half of an air filter represents 40 litres of air sampled during a dust storm in Mali, Africa. The filter is placed on nutrient media for 48 hours so the viable microbes can grow. The shiny, colourful circles are bacterial colonies. The fuzzy patches are fungi. These colonies range in size from about 1 to 5 millimetres. (Kellogg and Griffin (2006))

Also human health is affected by aerosol particles. Short term exposures to highly aerosol polluted air can cause a higher susceptibility to mortality and serious morbidity effects to weaker humans and less serious health effects such as transient increases in respiratory symptoms, decreased lung function, or other physiologic changes to otherwise healthy people.
Especially the particles smaller than 2.5μm form a great risk to human health because they are small enough to be breathed deep into the lungs and, in some cases, enter the blood stream. (Pope (2000))
Dust in the atmosphere can act as cloud condensation nuclei influencing the internal structure of the cloud, the number of droplets and their size. Different sized droplets fall through the atmosphere at different rates, which means that changing aerosols in the atmosphere can change the frequency of cloud occurrence, cloud thickness, their rain-making potential, rainfall amounts and the optical properties of clouds. A cloud with high aerosol concentration will have more, small droplets. Smaller droplets also reflect more sunlight back into space, thus adding to the cooling effect of the system. This topic is demonstrated in figure 13. Clouds forming with small droplets produce little precipitation by drop coalescence. (Voiland and Simmon (2010))
The impact of dust on rainfall is smaller than that caused by smoke from biomass burning or anthropogenic air pollution, but the large abundance of desert dust in the atmosphere renders it important.
The reduction of precipitation from clouds affected by desert dust can cause drier soil, which in turn raises more dust, thus providing a possible feedback loop to further decrease pre-

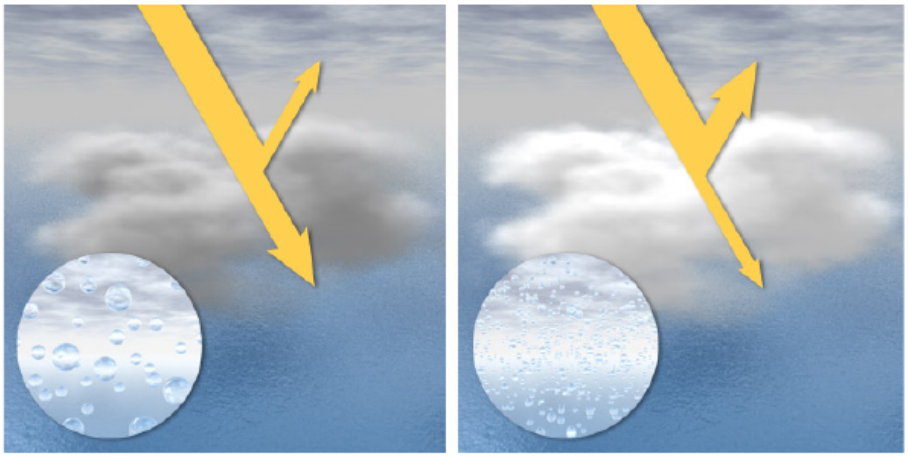

Figure 13: Clouds in clean air are composed of a relatively small number of large droplets (left). As a consequence, the clouds are somewhat dark and translucent. In air with high concentrations of aerosols, water can easily condense on the particles, creating a large number of small droplets (right). These clouds are dense, very reflective, and bright white. (NASA image by Robert Simmon.)

cipitation. Furthermore, anthropogenic changes of land use exposing the topsoil can initiate such a desertification feedback process (Rosenfeld et al. (2001)).
Solmon et al. (2008) shows that the patterns of precipitation anomalies caused by desert dust are very sensitive to the dust absorbing properties.
Mineral dust carries iron and with dust deposition into the ocean it influences the ocean chemistry and biology. Changes in the dust flux to the ocean result in changes in the availability of iron in the water. Iron is an essential nutrient for all organisms, used in a variety of enzyme systems, including those for photosynthesis, respiration, and nitrogen fixation. Iron supply is a limiting factor on phytoplankton growth over vast areas of the modern ocean. Thus dust can cause a shift in species and in phytoplankton size distribution or a change in oceanic CO_2 uptake by altering the efficiency of organic carbon export to deep water. Jickells et al. (2005))
Figure 14 shows a phytoplankton bloom caused by the desert dust deposed into the ocean off West Africa.

40 million tons of Saharan dust are transported to the Amazon basin each year, about half of it originates from the Bodélé Depression. The Saharan mineral dust acts as a fertilizer for the Amazon rain forest, hence the health and productivity of the rain forest depends on the dust from Africa. 140Tg are transported in the summer towards the Amazon and 100Tg in winter. 140 ± 40Tg are deposed in the Atlantic ocean and 50 ± 15Tg reach the Amazon basin (Koren et al. (2006)). By fertilizing the the equatorial Atlantic Ocean dust influences indirectly the CO_2 cycle (Bristow et al. (2010)).
Dust in the atmosphere has also historic scientific advantages. Studies of paleoclimate use size distribution measurements of aeolian dust in marine sediments to infer climatic conditions over geologic time (Maring et al. (2003)).

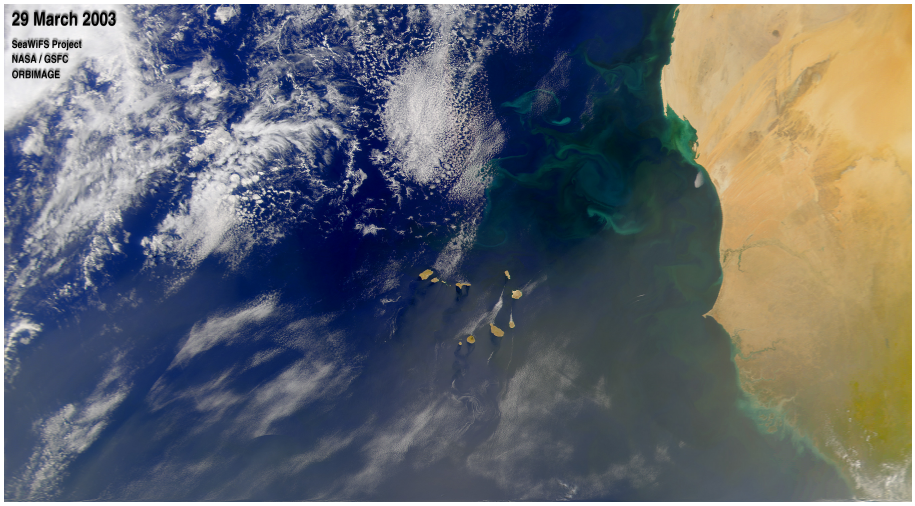

Figure 14: Phytoplankton blooms are visible in this SeaWiFS image of the Atlantic Ocean off of western Africa, collected on March 29, 2003.(NASA)

2 The regional model system COSMO-MUSCAT

The COSMO MUSCAT model is a regional model system to simulate the emission, transport, deposition and the radiative effects of Saharan dust.
Within the SAMUM-2 field campaign in January and February 2008 the spatial and temporal evolution of the dust plumes was modelled. For a detailed description see Heinold et al. (2011b) and Heinold et al. (2011a). In figure 15 the model domain is shown. The regions covered in the simulations are the Sahara, parts of the Atlantic and Europe.

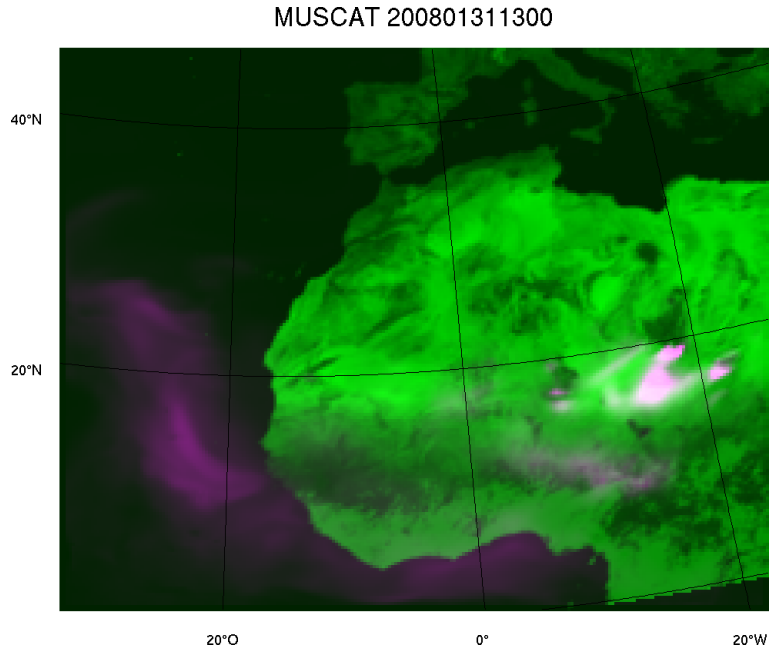

Figure 15: The area covered in simulations by the COSMO-MUSCAT model. The surface albedo is shown in green shades and pink color stands for the dust cloud. Modelled dust cloud from 31. January 2008 at 13:00 UTC.

The major features of COSMO-MUSCAT are the radiative forcing and the size resolved dust concentrations with a flexible module technology to provide the possibility of a variety of sensitivity studies.
The high grid resolution (28km horizontal resolution) allows to study regional effects. With the regional modeling it is possible to compute surface properties and transport processes on smaller scales and thus can resolve local meteorological procedures controlling dust processes.
One part of the parallelized multi-scale regional model system COSMO-MUSCAT is the non-hydrostatic model COSMO (formerly named Lokal-Modell, LM) which is an operational weather prediction model of the DWD (German Weather Service). It is the meteorological driver and it is coupled online with the 3D chemistry tracer transport model called MUltiScale chemistry Aerosol Transport model (MUSCAT). The micro-physical processes and chemical reactions are described here by time dependent mass balance equations.

The dust emission in desert regions depends on surface wind friction velocity, surface roughness, soil texture and soil moisture. With the surface winds and the soil moisture the dust emission is calculated with the dust emission scheme by Tegen et al. (2002).
The modelled dust is transported as a passive tracer in five independent size classes with a diameter range from 0.2 to 48μm. The dust leaves the atmosphere caused by dry or wet deposition. In SAMUM 2 a scheme for vegetation fire emissions of smoke particles was developed to study the dust and biomass-burning aerosol mixed clouds. The model results are validated with ground based and space-borne remote sensing, lidar profiles, sun photometer measurements and local field measurements.
The dust plumes are represented passably well in time and space in some cases, but strong dust outbreaks are underestimated. The problems in the modelled aerosol distribution are discussed in Heinold et al. (2011b).
The COSMO-MUSCAT model allows for radiative transfer calculations. For a detailed description of the realization in the model see Heinold et al. (2011a).
In COSMO-MUSCAT the interaction of the computed aerosol load with the solar and terrestrial radiation and with the atmospheric dynamics are included. To compute the radiative fluxes a modified COSMO radiation scheme is is used. Here the variations in the modelled size-resolved aerosol fields are considered. The radiative effects can influence the COSMO meteorology and feed back on dust emission and aerosol transport.
Mie theory (see chapter 5.2) was used to provide the optical properties for each size bin using the refractive indices from laboratory measurements reported by Sokolik and Toon (1999). The assumed imaginary refractive indices represent the lower end of the range of the measurements taken in the frame of the SAMUM campaigns.
A map from MODIS measurements is used as surface albedo. The same map also describes the surface albedo in the MC-UniK radiative transfer calculations performed in this study.

3 Radiance measurements

The radiance fields of Saharan dust clouds are measured by different measurement devices. In this chapter the measurements from the MSG satellite and from a pyranometer on board an aircraft are compared. The MSG satellite also provides the possibility to build an infra red (IR) dust index to detect dust clouds even over land surface. The IR index is compared to the spatial distribution of the modelled dust cloud from the COSMO-MUSCAT model.

3.1 MSG satellite measurements

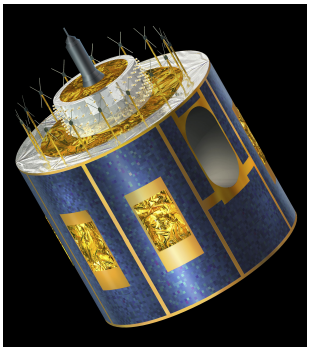

Figure 16: Artist view of MSG (Meteosat Second Generation) satellite being developed by ESA in co-operation with EUMETSAT. (http : / / eumetsat.int / Home / index.htm)

Meteosat Second Generation (MSG) is a joint project between ESA and the European Organization for the Exploitation of Meteorological Satellites (EUMETSAT). In 1977 the first Meteosat geostationary spacecraft was launched and since then ESA has been building Europe's orbital weather satellites.
Meteosat-9 (see figure 16) is now the prime observational satellite at 0 degrees longitude, in geostationary orbit, 35800km above the Gulf of Guinea. The older satellite Meteosat-8 became the in-orbit spare, positioned at 3.4 degrees West. Meteosat-8 acquires improved information and imagery for weather forecasting as well as other applications such as hydrology, agriculture, environmental studies as well as risk prevention and disaster warnings. The MSG satellite is equipped with the SEVIRI (Spinning Enhanced Visible and Infrared Imager) instrument shown in a photograph in figure 17. The instrument provides measurements in 12 spectral channels which are presented in table 1.

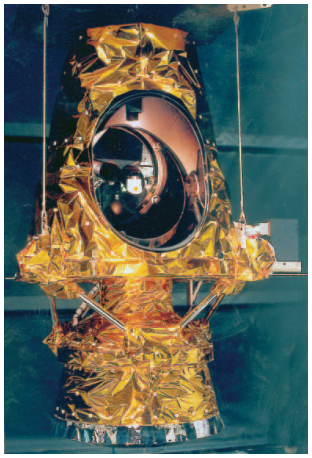

Figure 17: SEVIRI (Spinning Enhanced Visible and Infrared Imager) instrument (http : / / www.eumetsat.int/Home/index.htm)

Channel No.	Spectral Band (μm)	Characteristics of Spectral Band (μm)			Main observational application
		cen	min	max	
1	VIS0.6	0.635	0.56	0.71	Surface, clouds, wind fields
2	VIS0.8	0.81	0.74	0.88	Surface, clouds, wind fields
3	NIR1.6	1.64	1.50	1.78	Surface, cloud phase
4	IR3.9	3.90	3.48	4.36	Surface, clouds, wind fields
5	WV6.2	6.25	5.35	7.15	Water vapour, high level clouds, atmospheric instability
6	WV7.3	7.35	6.85	7.85	Water vapour, atmospheric instability
7	IR8.7	8.70	8.30	9.1	Surface, clouds, atmospheric instability
8	IR9.7	9.66	9.38	9.94	Ozone
9	IR10.8	10.80	9.80	11.80	Surface, clouds, wind fields, atmospheric instability
10	IR12.0	12.00	11.00	13.00	Surface, clouds, atmospheric instability
11	IR13.4	13.40	12.40	14.40	Cirrus cloud height, atmospheric instability
12	HRV	0.4−1.1μm			Surface, clouds

Table 1: Spectral channel characteristics of SEVIRI in terms of central, minimum and maximum wavelength of the channels and the main application areas of each channel. (Schmetz et al. (2011))

The resolution from 35800km altitude is 1km for the high-resolution visible channel and 3km for the infra-red and the 3 other visible channels.
With that covering in wavelengths, the high spatial resolution and the small time passing between two measurements provide new and, in some cases, unique capabilities for cloud imaging and tracking, fog detection, measurement of the Earth-surface and cloud-top temperatures, tracking of ozone patterns, as well as many other improved measurements. The view of MSG from http : //www.eumetsat.int/Home/index.htm is presented in figure 18.

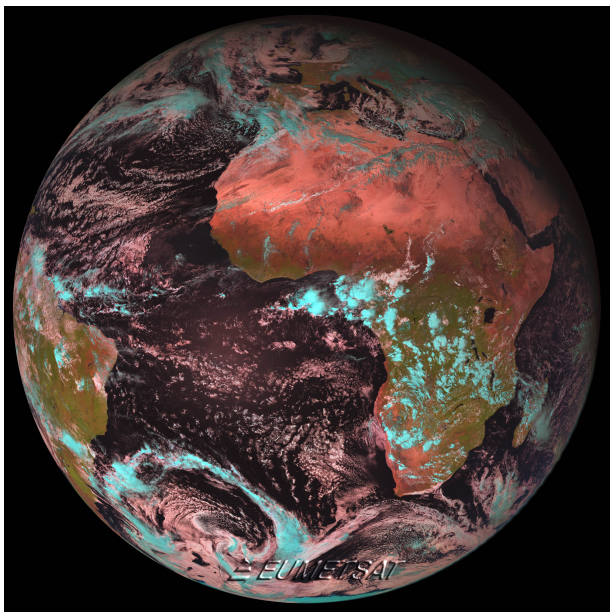

Figure 18: First colour image of the Earth acquired by the MSG-2 satellite on 25 January 2006. Credits: EUMETSAT 2006

The satellite radiances are obtained by reading in the satellite pictures from each channel and then convert them to radiances by an IDL progam based on the calibration algorithm from Lars Klüser (2006), modified by Timo Hanschmann in 2007. They used the parameters mentioned in Clerbaux (2006).
For this study the applicability on the detection of dust was very useful. It is possible to detect the dust with the help of the brightness temperature differences (BTD). For the dust detection the SEVIRI channels with the center wavelengths 8.7, 10.8 and 12.0μm in the IR are used. The IR dust index is a composite of the channels and their differences at 12.0μm-10.8μm [BTD(12, 10.8)] and 10.8μm-8.7μm [BTD(10.8,8.7)], as well as 10.8μm. In this composites the dust can be seen in red to pink color. (e.g. Ackerman (1997), Sokolik (2002))
There are some effects which allow the dust detection in the infra red wavelength region. Thermal emission of the desert surface is higher at a wavelength of 10.8μm compared to the emissivity at 8.7μm. In case of dust the BTD decreases between the 10.8μm and 12.0μm wavelengths compared to clear sky conditions. The same holds for the BTD at the wave-

lengths 8.7μm and 10.8μm.
The IR dust index benefits from the different particle sizes from airborne and surface dust. The thermal infrared spectrum of silicate and carbonate minerals show strong differences between the thermal properties of the smaller dust particles (diameter of $2-5$μm) and the larger sand particles (diameter larger than 70μm). The emissivity of quartz around the wavelength of 11μm increases with the particle size and decreases at a wavelength of 8.6μm. (Wald et al. (1998)) The BTD(12, 10.8) for dusty atmosphere decreases in comparison to clear sky conditions.
The dust index may be biased by variations in brightness temperature differences for dust at different heights. (Schepanski et al. (2007)) The IR index only is a qualitative index which only provides information about the presence or absence of dust.
In figure 19 some examples of the dust events this work covered are shown. The scenes are from the 19., 25. and 31. August around noon. The figure provides a comparison between the IR dust index and the modelled dust cloud from the COSMO-MUSCAT model. The day where the modelled and the measured dust cloud pattern agree best is on 31. August. That's why this day was used for most examples and calculations in this thesis in order to minimize differences due to different dust transport patterns in models and observations.

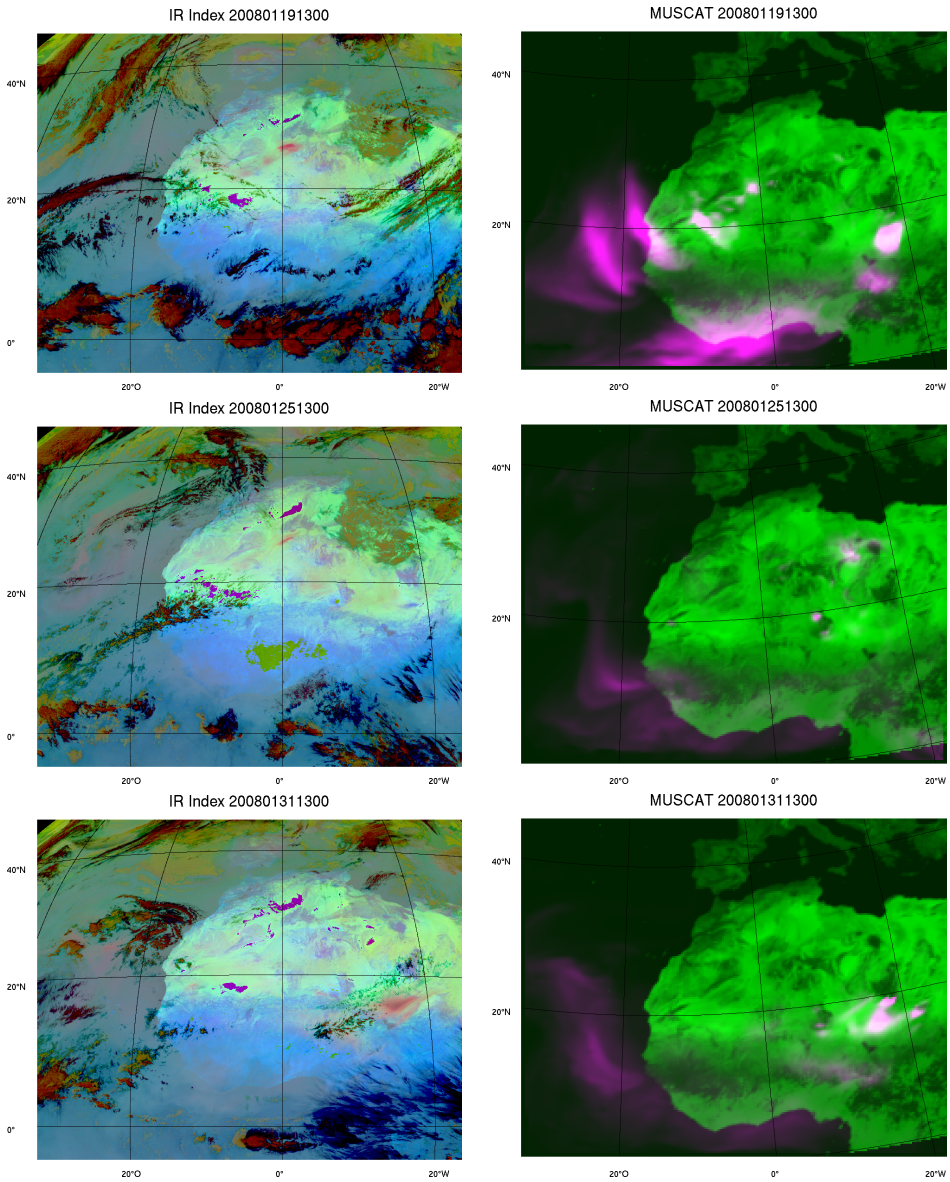

Figure 19: Comparison of three different dust scenes: on the left the IR dust index and on the right the modelled dust cloud by COSMO-MUSCAT. The dust is coloured pink and the surface albedo of the model domain is shaded in green. For more pictures from other dust scenes see the appendix in chapter 8.

3.2 Aircraft measurements

During the second field campaign of SAMUM airborne measurements of upward spectral irradiance were made. The field campaign was based in Praia on the Cape Verde Islands in January 2008. A more detailed description of the aircraft measurements are given in Bauer et al. (2011).
The investigating aircraft was Falcon from the German Aerospace Center (DLR) which performed nine flights during the campaign. The flights were carried out over the Atlantic ocean at different altitudes. Upward spectral irradiance was measured with the Modular Airborne Radiation Measurement System (SMART) Albedometer in the wavelength range of 0.4–2μm (Bauer et al. (2011)).
For better comparability with the satellite measurements only flight heights above 5000 metres were considered.
For comparison the aircraft measurement days 22 and 25 January and February the 4th were chosen. According to the time and the position of the aircraft the corresponding satellite images were taken. As the temporal resolution of the satellite measurements is 15 minutes and the aircraft measurement device has a temporal resolution of 2 seconds, always the best fitting satellite picture was used. A larger problem poses the different spatial resolution of the measurements. The aircraft measurements are performed by a pyranometer. The measured radiance is integrated over the entire half space. And the satellite measurements resolution is about 3km at nadir, so that the satellite pixel including the Aircraft position were chosen. Following from that the comparison between Aircraft and satellite measurements is done for differing spatial resolutions which may result in bigger deviations. To obtain a comparable spectral range of both measurements, the spectral radiances from the aircraft were interpolated and multiplied with the spectral weighting function of SEVIRI channel 1 with a center wavelength at 0.6μm. Figures 20, 21 and 22 show the comparison of the measurements for the three selected measurement days.
Both satellite and aircraft measurements pattern fit good but because of small scale differences the resulting correlation of about 0.4 is non satisfying. In most cases the satellite measurement values are a little lower than the aircraft measurements, also the radiance peaks are more pronounced for the Aircraft measurements. One possible explanation can be that there are water clouds contaminating either the Aircraft or the satellite measurements. The different spatial and temporal resolution can also cause the deviation of the values. The different measurement hights might also contribute to the aberrations. The satellite measures at a hight of 38500km and for comparison only Aircraft measurements above 5km hight were considered. Although 55% of the atmosphere are below 5 km, there still is absorbing atmosphere with aerosol particles above the aircraft which may cause the lower radiance values in the satellite measurements.
For January 22 in figure 20 the pattern of the measurements fit good, but the satellite measurements are a little smaller in general. The peaks mainly caused by clouds are captured in nearly the same time by both measurement devices, but they are less pronounced by the satellite measurements. They may be caused by the averaged pixels from satellite of about 3×3km.
On January 25 in figure 21 it looks the same. On this day the measurements are more

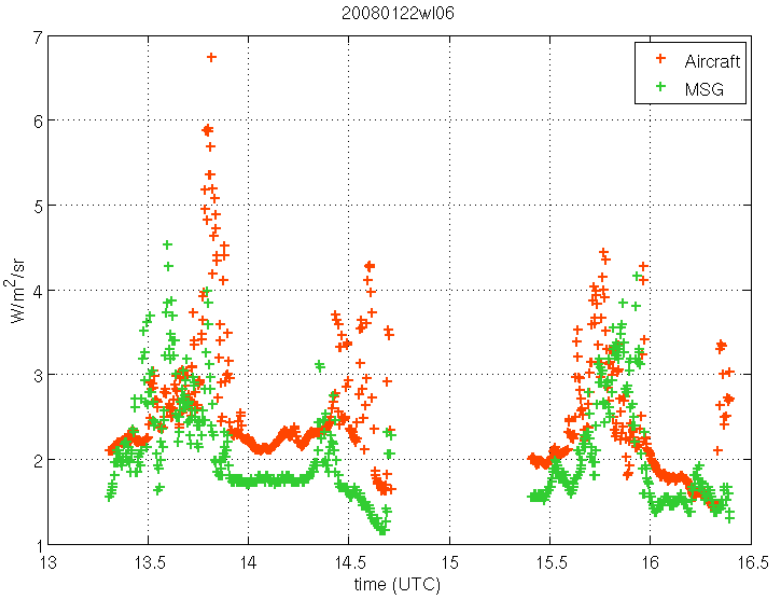

Figure 20: Measurements of aircraft and MSG on 22nd of January 2008; correlation coefficient 0.3779

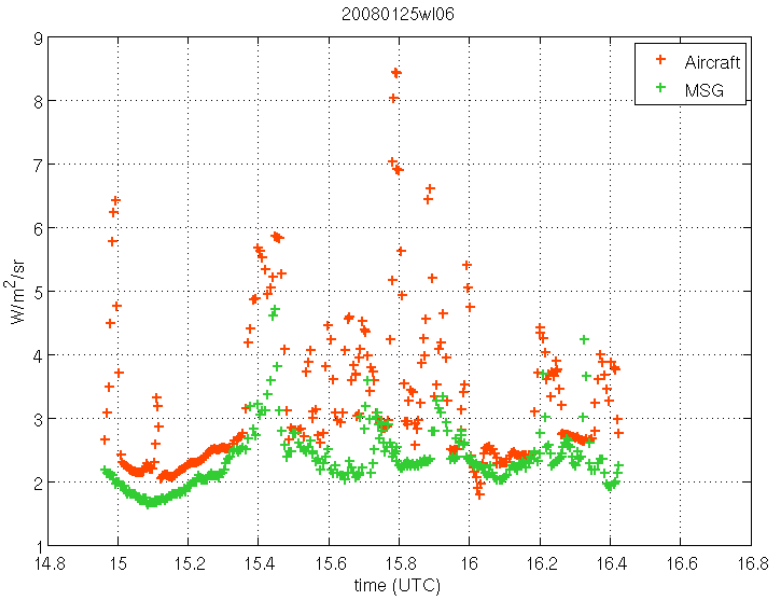

Figure 21: Measurements of aircraft and MSG on 25th of January 2008; correlation coefficient 0.4185

varying and some peaks are not captured by the satellite.
On February 4 shown in figure 22 it looks a bit different. The radiance is not varying so much and there are few big peaks. These peaks only occur in the aircraft measurements and they

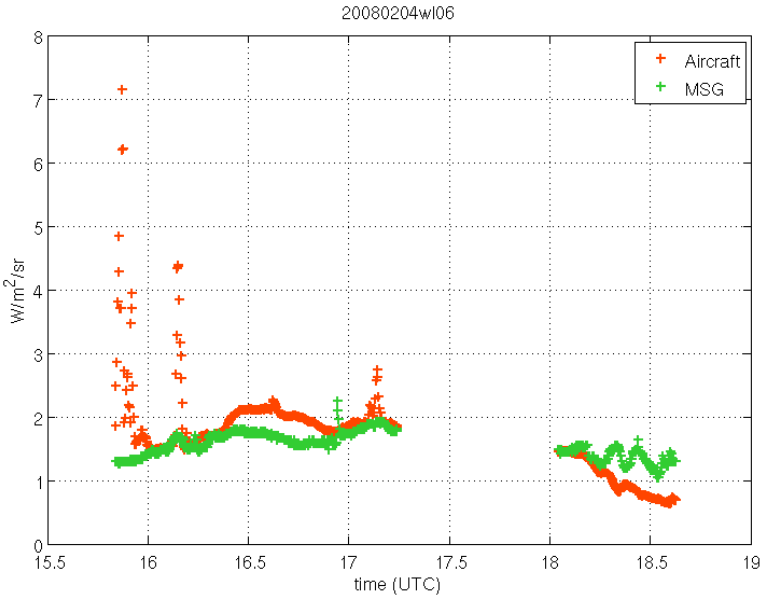

Figure 22: Measurements of aircraft and MSG on 4th of February 2008; correlation coefficient 0.3587

are averaged out due to the spatial resolution of the satellite.

4 Radiative transfer in the atmosphere

The radiative transfer through the atmosphere plays an important role for climate dynamics. Thus the understanding of these processes is essential for understanding the climate system.
The radiative transfer through the atmosphere describes the way of the photons from the Sun through the atmosphere towards the detector.
On their way the photons can be absorbed or scatterd by aerosols, molecules or cloud droplets. The processes are described in radiative transfer theory and modelled in radiative transfer simulations. This chapter gives a brief introduction into the interactions of photons with the atmosphere.

4.1 Theory

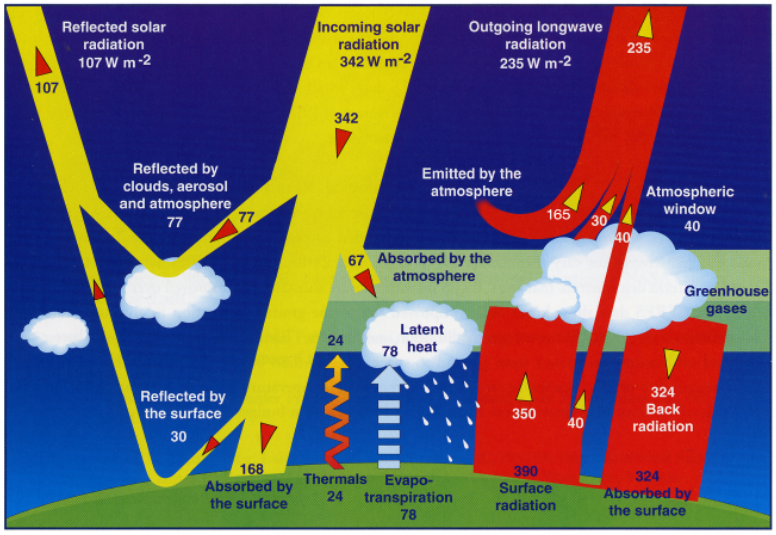

Figure 23: Kiehl and Trenberth (1997)

The major processes in atmospheric radiative transfer are shown in figure 23. The incoming solar radiation is reflected by clouds or aerosols and by the surface and can be absorbed by atmospheric gases, clouds, aerosol or the surface. Roughly summarized about 30% of the incoming solar radiation are reflected at the top of atmosphere, 20% are absorbed in the atmosphere and 50% are absorbed by the Earth's surface. The long-wave radiation is emitted by the surface an the atmosphere and can be reflected in the atmosphere or emitted to space. The radiative transfer is the only way in which the Earth exchanges energy with the universe.
The radiation differs locally and in time for example because of the temporal an spatial variation of incoming solar radiation due to the moving of the Earth and the sun, the Earth's rotation and the gravitational forces. But thermodynamic processes are always acting to balance the energy budget. On longer time scales the Earth's energy budget is balanced

towards equilibrium.

Incoming solar radiation The emitted radiant flux density at the sun's surface is $F_s = 63.2 * 10^6 W/m^2$. But with the travelled distance to the Earth's atmosphere the radiant flux density is decreasing. The sun's radius is $r_s = 696 * 10^6 m$ and $r = 149.6 * 10^9$ is the mean distance from sun to Earth. With

$$F(r) = F_s \frac{r_s^2}{r^2} \tag{4.1}$$

this results in the solar constant $F_0 = 1367 W/m^2$ as the incoming solar radiant flux density at the top of atmosphere. The spatial and temporal mean of the incoming radiation referred to the Earth's surface is one fourth of the solar constant, $342 W/m^2$, because the area of the solar radiation field shadowed by the Earth's Volume is πr_e^2 where r_e is the Earth's radius. Figure 24 shows the incoming solar radiation at the top of the atmosphere (yellow) and at

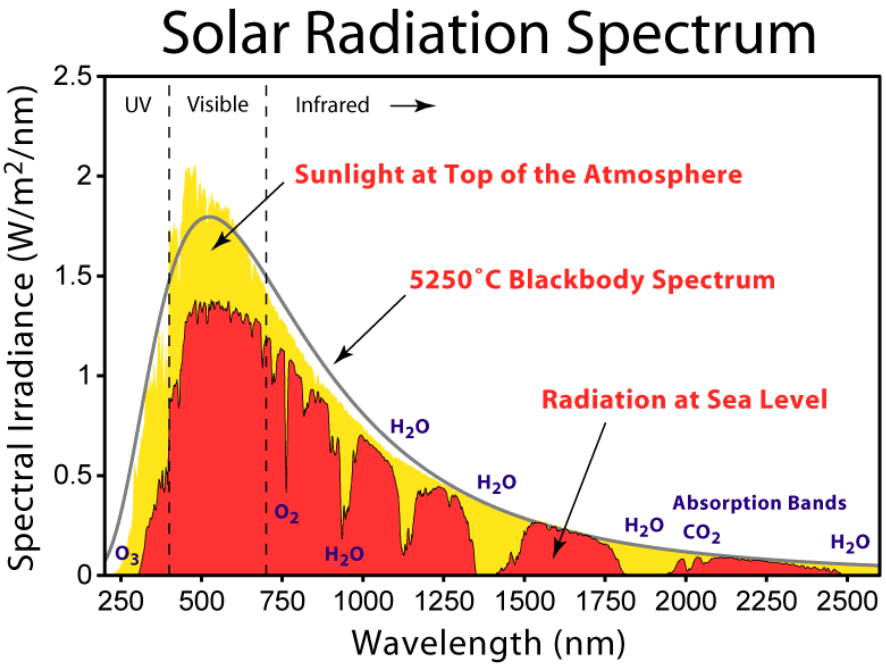

Figure 24: http://www.globalwarmingart.com/wiki/File:Solar_Spectrum_png

sea level (red).

Radiative transfer in the atmosphere The theory of radiative transfer describes the propagation of electromagnetic waves trough the atmosphere. In this work calculations with the Monte Carlo radiative transfer program MC-UniK (Chapter 6, Macke et al. (1999)) were performed.

For applications on dust clouds the radiation field is interesting. Thus the scattering properties of individual molecules or particles are averaged over certain volume parts of the dust cloud for the radiative transfer calculations.
The radiation transported through the atmosphere has to pass several obstacles. The photons can interact with molecules from the atmospheric gases, with aerosols like dust particles or with cloud droplets on their way through the atmosphere.
The process of radiative transfer through the atmosphere can be described in the following simplified form: A ray of light with a specific wavelength and an intensity is heading towards a medium with a volume and a cross section. When the ray hits the volume element, the intensity of the light beam decreases and radiation is scattered according to a scattering angle. The intensity is decreasing by extinction, which is the sum of the above mentioned scattering and absorption. The radiative transfer through the atmosphere is summarized in the following equation (Scheirer (2001)).

$$L(s_2) = L(s_1)e^{-\int_{s_1}^{s_2}\beta_x ds} + \int_{s_1}^{s_2} J(s)e^{-\int_{s_1}^{s_2}\beta_x ds}\beta_x ds \tag{4.2}$$

s_1, s_2 = starting and ending point
L = radiance in $Wm^{-2}sr^{-1}$
β_x = volume extinction coefficient in m^{-1}
s = travelled way in m
$J(t)$ = source term in $Wm^{-2}sr^{-1}$

The equation 4.2 describes the changing of the radiance L along the optical path from point t_1 to point t_2 through an absorbing and emitting medium. The red part in equation 4.2 describes the attenuation of the radiance caused by absorption and scattering. The blue part describes the increase caused by emission and diffuse scattering. The problem in solving the radiative transfer equation 4.2 is the source term J. The detailed form of J is:

$$\begin{aligned} J = & \frac{\omega_0}{4\pi}\int_0^{2\pi}\int_0^{\pi} P(\vartheta,\varphi,\acute{\vartheta},\acute{\varphi})L(\acute{\vartheta},\acute{\varphi})\sin(\acute{\vartheta})d\acute{\vartheta}d\acute{\varphi} \\ & + \frac{\omega_0}{4\pi}P(\vartheta_0,\varphi_0,\vartheta,\varphi)(\pi F_0)e^{-\frac{\int_z^\infty \beta_x dz}{\cos\vartheta_0}} + (1-\omega_0)B(T) \end{aligned} \tag{4.3}$$

w_0 = single scattering albedo

P = scattering phase function in sr^{-1}

ϑ, φ = direction of the considered radiation

$\acute{\vartheta}, \acute{\varphi}$ = angle of incidence of diffuse radiation

ϑ_0, φ_0 = angle of incoming solar radiation

F_0 = solar radiant flux density in Wm^{-2}

B = Planck function in $Wm^{-2}sr^{-1}$

The red part of equation 4.3 is part of the diffuse radiation, which propagates by scattering into the considered direction of radiation (ϑ, φ) and thus has to be added. In the blue part of equation 4.3 is described the part of the direct radiation, which is scattered along the considered direction. And finally the green part stands for thermal emission and thus is the only true source.
The problem in solving the radiative transfer equation is caused by the red part of equation 4.3 because there the searched term of radiance is involved. (Thomas and Stamnes (1999)) In the case of scattering also influences from the whole atmosphere have to be considered. With the spatial variables (x, y, z) and the angle dependent Parameter (Θ, Φ) the radiative transfer equation is a five dimensional system. Hence this differential equation can not be solved analytically without big simplifications in the scattering phase function. And even in numerical solutions the phase function hinders especially in 3D inhomogeneous clouds. (Meyer (2006))

Solutions of the radiative transfer equation There are several numeric methods to solve the radiative transfer equation. For example, for vertical inhomogeneous, plane-parallel clouds in the atmosphere the Doubling/AddingMethod from Hansen and Travis (1974) can be used. The vertical inhomogeneous atmosphere is approximated by a finite number of plane-parallel, adequate thin layers. The reflection and transmission of each layer have to be calculated exactly and then are added to a total reflection and total transmission. For that the layers have to be sufficiently thin that only one scattering process can occur while the photon passes one layer (single scattering approximation).
By adding or doubling one layer, vertical inhomogeneous clouds can be constructed. The Doubling/AddingMethod is versatile for the 1D radiative transfer and can be used for any vertical layered atmosphere with any optical thickness. But this method is only suitable for 1D radiative transfer and the computing time is increasing drastically with high vertical inhomogeneity on small scales, high optical thickness and desired higher accuracy.
Another method to approximate the radiative transfer equation is the method of successive order of scattering. It also works only for vertical inhomogeneous atmospheric cloud fields. But in this method multiple scattering is iteratively embedded. The scattered intensities are build from multiple scattered parts. This method is not limited in 1D radiative transfer. The

sum is build over the number of scattering processes from single photons.
First the radiative transfer equation is solved for single scattering, then the result is inserted in the source term for double scattering. This results in the part of radiative intensity created by two times scattering transmission or reflection. Going on like this in an iterative way leads to a numerical approximation for the intensity after multiple scattering. The method of successive order of scattering has low speed of convergence. Especially for atmospheres with high optical thickness there are more scattering events and the computing time is increasing. Also with low absorbing layers iterating lasts longer because multiply scattered photons still have a significant impact on the results and more iteration steps have to be performed.
To handle 3D inhomogeneous atmospheric structures Evans (1998) has developed another method. It is called the *Spherical Harmonics Discrete Ordinate Method* (SHDOM). SHDOM calculates spatial variable radiance fields. It is based on the *Discrete Ordinate Method* (Stamnes and Swanson (1981)) and some elements from the *Spherical Harmonic Method* (Zdunkowski and Korb (1974)). The radiative transfer equation 4.2 is solved along discrete ordinates in the spatial grid. It is an iterative procedure with the four following steps:

- the source functions are given in extension in spherical harmonics and are transformed into discrete ordinates. They are determined for discrete solid angles.
- radiant fields are calculated with integration of the source function
- backward transformation from the radiance fields to the spherical harmonics
- the source functions are obtained from the surface spherical harmonics

The convergence criterion is that the difference of the root mean square of two successive source function fields is lower than a certain threshold. The iteration breaks when the convergence criterion is achieved, if not, the cells where the gradients in the source function field are biggest, are refined. With the smaller cells the iteration starts again. Thus the spatial resolution in the parts with high gradients in the source function field is refined as long until the radiance fields go together well with the source function field. For big cloud fields the SHDOM is not recommendable because of long computing time and the big amount of memory needed.
The method to solve the radiative transfer problem used in this work is the *Monte Carlo Method*. It is described in House and Avery (1969) or Hansen and Travis (1974). Here the scattering function is treated as a probability density function for the scattering into a certain scattering angle. From the probability to go through an optical thickness the free path length is derived. The radiance field is obtained by the location and the character of the interaction of the photon with the molecules or particles in the medium.
The scheme in general is very simple and it is suitable to perform radiative transfer calculations in highly inhomogeneous atmospheric clouds. The accuracy is increasing with the number of photons. The method is explained in detail in the following part.

4.2 MC-UniK model description

The *Monte Carlo Method* is a widespread method to solve mathematical problems. A lot of single spot test experiments yield to an approximation for a numerical problem. The accuracy of the solution is increasing with the number of experiments and thus high accuracy can be reached if sufficient computing time is provided. In the last years Monte Carlo methods are getting more and more important because substantial progress is made in computer technics.
The path of photons through an inhomogeneous atmosphere is simulated with the Monte Carlo method. Transmission, reflection and scattering processes are simulated for photon packages getting into the model region from the Sun's direction. The packages are tracked on their way through the atmosphere to the detector. Finally all simulated photon packages are summed and the radiance fields are obtained.
The photon package enters the model domain from the Sun direction. By comparing the optical thickness of the travelled way $\acute{\tau}$ with an available optical thickness τ^* which depends on a random number, the step size between two scattering processes is obtained. Thus it depends on the probability for transmission according to the *Bourgert-Lambert-Beer's law* (4.4).

$$L_\lambda(l) = L_\lambda(0)e^{-\tau_l} \tag{4.4}$$

L = radiance
λ = wavelength
τ = optical thickness
l = path length trough the medium

For the available optical thickness the following equation is applied:

$$\acute{\tau} = -\ln(d) \tag{4.5}$$

with a random number $d \in [0,1]$ and:

$$\acute{\tau} = \sum ls_i\beta(x,y,z) = -\ln(d) \tag{4.6}$$

If equation (4.6) is satisfied a scattering process takes place. The step size stands for the step within a homogeneous box.
If the summed optical thickness is larger than the available $\acute{\tau}$, the photons jump backwards to the point where they have the same value.
This is the new scattering location. The probabilities for the scattering, transmission and absorption processes are given in equations (4.7), (4.8) and (4.9).

$$P(\text{transmission}) = e^{-\beta(x,y,z)s} \tag{4.7}$$

$$P(\text{absorption}) = 1-\omega_0(x,y,z) \tag{4.8}$$

$$P(\text{scattering}) = P(\Theta) \tag{4.9}$$

β = extinction coefficient in considered model area box

s = step size

$w_0(x,y,z)$ = single scattering albedo in considered model area box

The absorption in the scattering location is obtained by equation (4.8). The absorption is defined through the local single scattering albedo. The original photon package weight, that was determined when the package enters the model domain is decreased by multiplying the photon weight with the local single scattering albedo. When a photon package is scattered, the new direction is obtained from the scattering phase function and a random process as shown in equation (4.9).

$$F = \frac{I}{\cos(\vartheta_i) F_{in}} \tag{4.10}$$

with

$$I(x,y,\Theta_0,\Phi_0,\Theta,\Phi) = \sum Nw(x,y,z)\omega_0(x,y,z)P_{det}(\Theta,\Phi)e^{-\tau_{det}} \tag{4.11}$$

F_{in} = incoming radiant flux

(Θ_0, Φ_0) = solar zenith and azimuth angle

(Θ, Φ) = zenith and azimuth angle of the detector

w = photon package weight

P_{det} = part of the scattering phase function in detector direction

τ_{det} = optical thickness along the way to the detector

By accumulating the parts of the energy from the photons scattered along a special solid angle interval $\Delta\Omega(\vartheta,\varphi)$, the reflected normalized radiance is gained in equation (4.11). If enough photons are traced, a statistical sufficient energy distribution leads to the radiance field.
Because of the method, that each photon package is traced, it is possible to simulate the way through any structure of cloud. Also highly complex scattering phase functions can be considered. Another advantage is, that intermediate results can be called.

For this study the Monte Carlo model of the University of Kiel (MC-UniK) (Macke et al. (1999)) was used. It was validated within the I3RC project (Intercomparison of 3D Radiation Codes (http://i3rc.gsfc.nasa.gov/) (Cahalan et al. (2005)). MC-UniK is a forward model for efficient calculations of radiances at discrete directions. MC-UniK simulates directly the path of photons through the dust cloud. Accuracy increases with the number of photons.
The model domain is separated into grid boxes which are characterized by their optical properties. The input data required for MC-UniK for each model grid box are the coordinates in x, y and z direction, the extinction coefficient β_{ext}, the single scattering albedo ω_0 and the

scattering phase function $P(\vartheta)$ depending on the scattering angle ϑ. Furthermore, the sun position, observer position, number of photons and surface albedo are required.

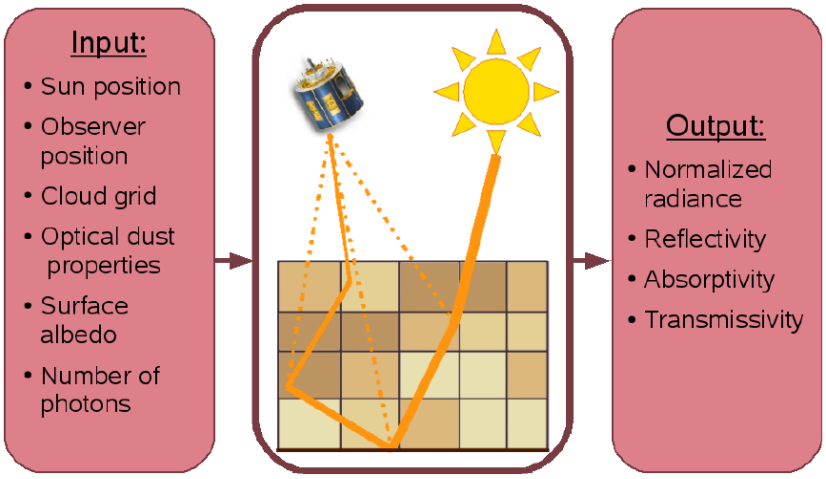

Figure 25: Scheme of MC-UniK

The illustration in figure 25 visualizes the general performance of the MC-UniK Model. The photons from the sun direction reach the 3D Cartesian cuboidal model domain. Different colours symbolize different optical properties of the dust cloud grid boxes. Photons are transmitted, absorbed and scattered on their way through the domain. One speciality of MC-UniK is that the radiance is not achieved by summing over the photons leaving the model domain, but with the help of the *Local Estimate Method* (Marshak and Davis (2005)). The *Local Estimate Method* considers the part of photons directly scattered into the satellite's viewing angle at each scattering process. This is demonstrated in the scheme in figure 25 by the dotted lines towards the satellite detector.
For calculating the radiance field the *Local Estimate Method* is more efficient than the common Monte Carlo photon counting method, because no photons get lost. Additional to each scattering process the part of the local photon energy which is directly scattered along the path towards the detector is considered. This part is attenuated at the length of the way to the detector and according to the probability of scattering into that direction registered. The free path length is based on *Beers Law* (equation (4.4)) and gives the step size between two successive scattering processes (equations (4.5) and (4.6)). A random process weighted with the scattering phase function results in the scattering angle. Absorption is taken into account with the photon weight multiplied by the local single scattering albedo.

4.3 Realization of MC-UniK calculations with data from SAMUM

To perform the MC-UniK calculations, the given size distribution from a COSMO-MUSCAT cloud is converted into optical properties. Because of the amount of data the boxes were grouped into scattering classes with similar scattering properties as described in chapter 5.7.
Resulting from that simplification, there are 14 different scattering classes. Each has one averaged phase function and one averaged extinction efficiency. Further the atmospheric molecules are considered by Rayleigh scattering (see chapter 5.1). The radiance calculated by MC-UniK is normalized with the unit $[\mu m^{-1} ster^{-1}]$. The results from the MC-UniK calculation with spherical particles for the chosen part of the dust cloud from 31 January 2008 13:00 UTC are plotted in figure 26.
The pictures are sorted by their wavelength in the columns. In the first column the results at 0.6μm, in the second at 0.8μm and in the third at 1.6μm are presented.
For the calculations of the shown results spherical particle shape is assumed. The first row shows the optical thickness. Here can be seen clearly that especially at the largest wavelength of 1.6μm the optical thickness is smaller. This is caused by lower extinction efficiencies for the larger wavelength as shown in figure 33 in chapter 5.2. There the scattering properties for spherical particles are presented depending on their size. The amount of small particles is bigger, thus the particles from the size class bin1 (effective radius 0.166μm) and bin2 (effective radius 0.501 μm) dominate the optical properties.
The second row shows the normalized radiance, the third the absorption, the fourth the reflection and the transmission is presented in the fifth row. The differences in the fields are most pronounced for the high wavelength of 1.6μm. There the absorption is lower, also the reflection is lower and the transmission is is higher than at 0.6 and 0.8μm wavelength. These differences lead to a higher radiance at 1.6μm. The radiative fields at 0.6μm and 0.8μm do not differ very much.
In the diagrams the spatial distribution of the radiative fields can be seen. Thus in comparison with the inhomogeneous cloud structure the relation between radiative fields and optical thickness can be seen. For example the absorption is higher in regions with high optical thickness, the same can be concluded for the reflection. The transmission is lower in the regions with high optical thickness.

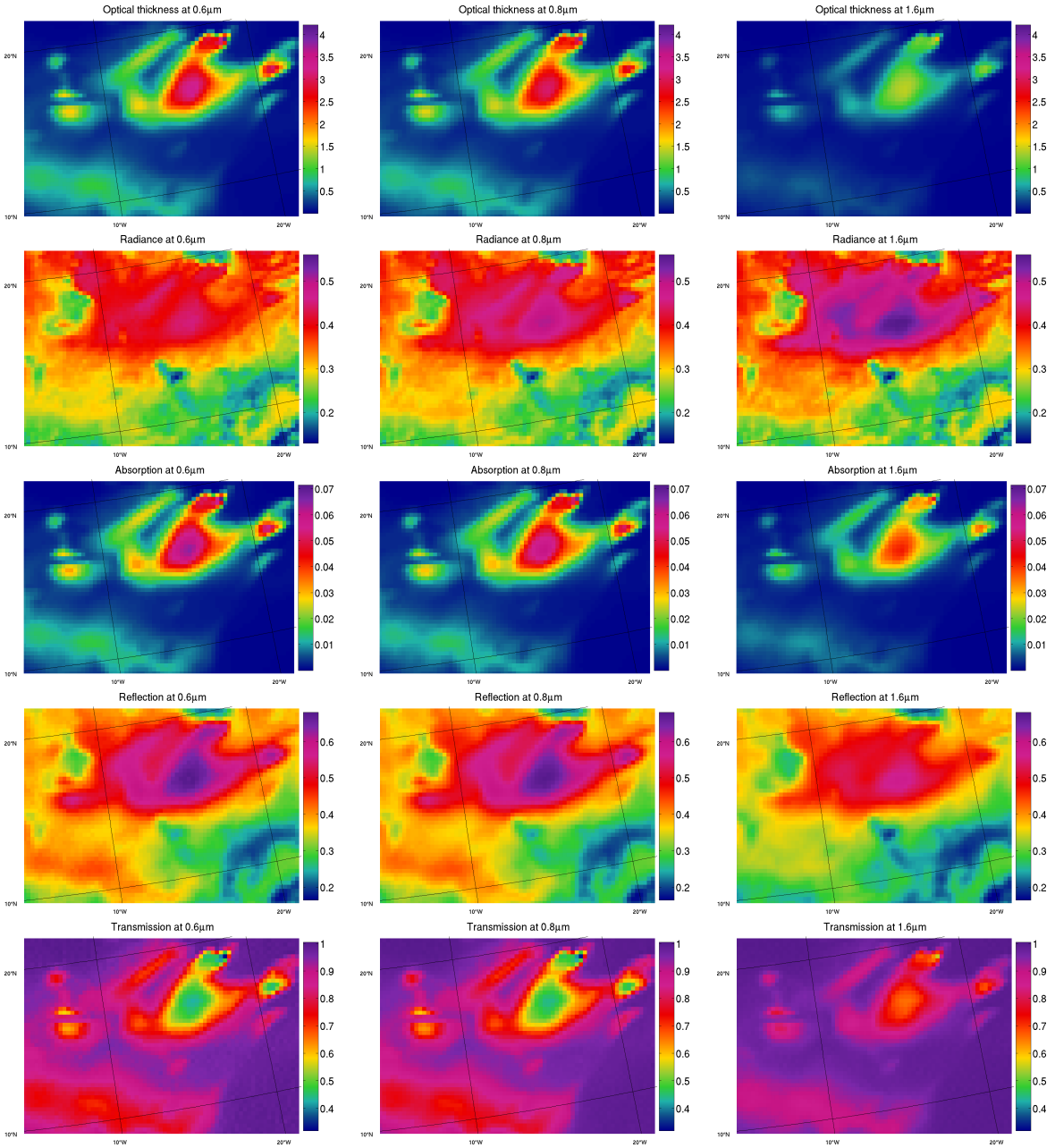

Figure 26: Results from Monte Carlo calculations: fields of optical thickness, radiance, absorption, reflection and transmission in the rows sorted by three columns for three wavelengths 0.6 μm, 0.8 μm and 1.6 μm. (spherical particles)

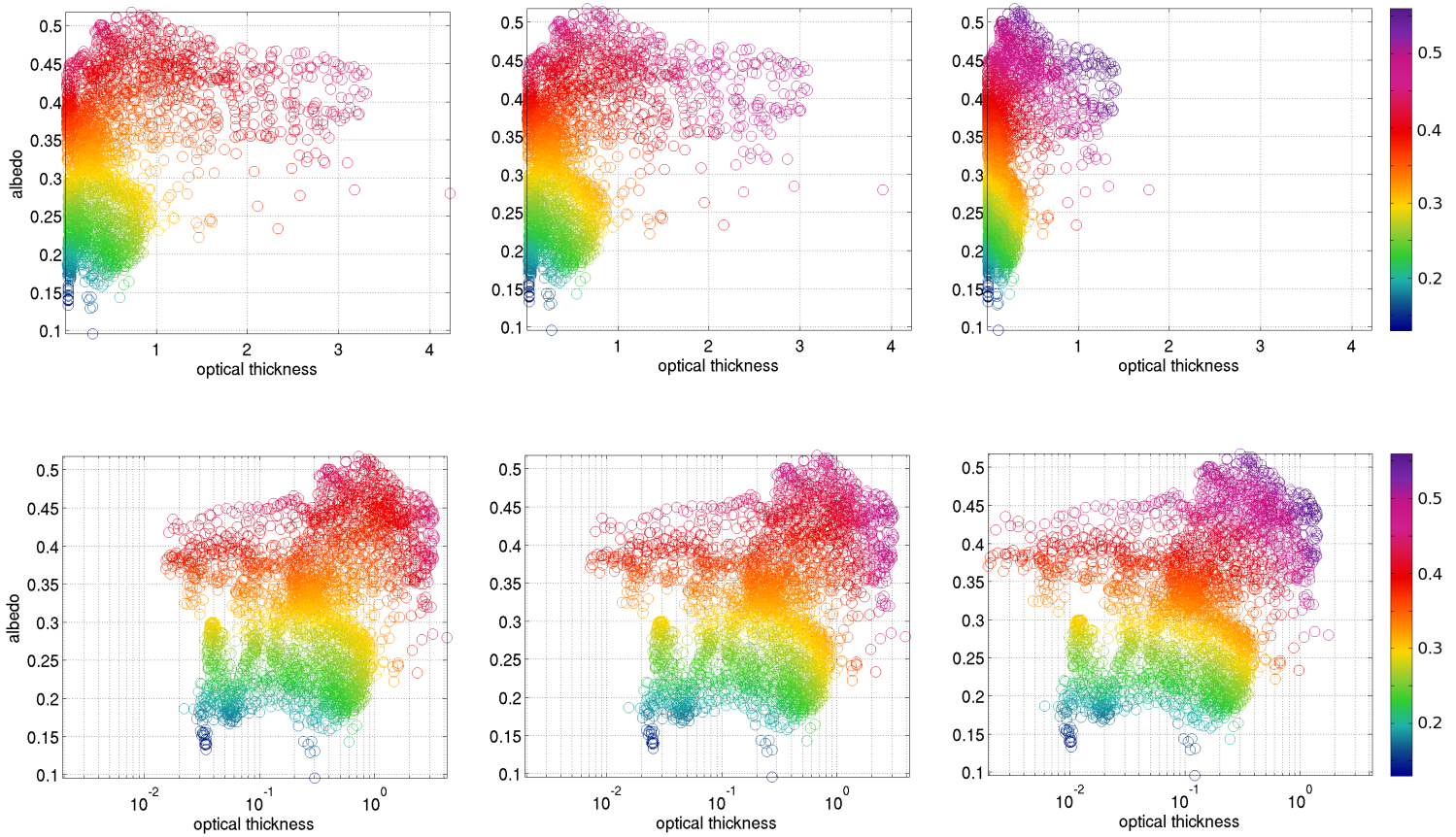

Figure 27: Normalized radiance in the color shown depending on the underlying surface albedo and on the optical thickness of the dust cloud.

In figure 27 the normalized radiance from the former spatial resolved pictures is shown dependent from the underlying surface albedo and the optical thickness of the dust cloud. In the second row the optical thickness is plotted in logarithmic scale. Here is indicated that esspecially the dust cloud pixels with high optical thickness are located over pixels with high surface albedo.
The areas with high surface albedo usually are the dust sources. The major dust sources are old dried lake beads as the Bodélé depression which is covered by the modelled area. The concentration of dust particles is highest next to the dust sources. This dust is not very old, therefore it carries a bigger proportion of large particles. The bigger particles fall out by gravity depending on their size and weight, within the regions next to the dust sources.
In figure 27, especially in the second row with logarithmic optical thickness can be seen that the normalized radiance is not directly increasing with the optical thickness. It seems that the surface albedo is dominatly influencing the values of normalized radiance, but for optical thicknesses above 1 also the normalized radiance is higher, thus is more influenced by the optical thickness than the low density cloud parts.

5 Aerosol scattering as realized in radiative transfer calculations

To perform radiative transfer calculations through the aerosol contaminated atmosphere the scattering properties of the aerosols are needed. Therefore the type of aerosol is very important as they have a big variety in the optical properties. The composition, the size and the shape of the particles are the main factors determining the optical properties. The photons passing the atmosphere can face for example gas molecules, dust particles or water droplets.
To describe the changes that can happen to a photon passing different types of particles, different methods are needed to obtain their scattering properties. To implement the radiative transfer, the scattering phase function, the single scattering albedo and the extinction coefficient are needed to fully describe the changes happen to the passing photons. Further description of these variables are given in chapter 4.
On the following pages different methods which are used to obtain the scattering properties of a variability of airborne particles are described.

5.1 Rayleigh scattering

For particles with a size parameter smaller than 0.1 the Rayleigh theory is used to calculate the scattering properties. This is necessary for example for scattering at gas molecules. The scattering phase function for Rayleigh scattering is described by the following equation and a polar plot is given in figure 28:

$$P(\Theta) = \frac{3}{4}\left(1+\cos(\Theta)^2\right) \tag{5.1}$$

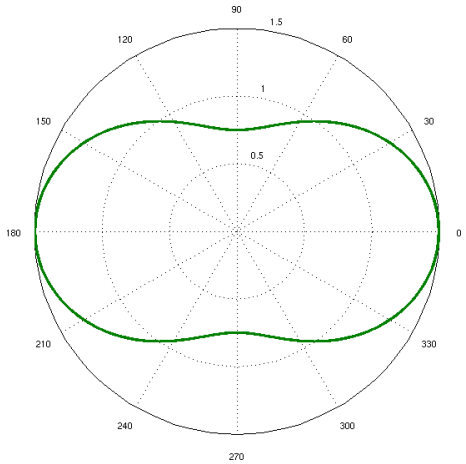

Figure 28: Rayleigh scattering phase function (Θ is the scattering angle)

The extinction coefficient is obtained from the extinction efficiency and the number of particles in the considered area.

The extinction efficiency itself can be calculated with the help of the refractive index.
The Edlén Equation (EDLÉN (1953)) is commonly used to get the refractive index of air. But since there are improved data available for density of air and refractivity of water vapour, in Birch and Downs (1993) an updated version of the Edlén Equation is presented:

$$(n-1)_s \cdot 10^8 = 8343.05 + \frac{2406294}{(130-\frac{1}{\lambda^2})} + (\frac{15999}{38.9-\frac{1}{\lambda^2})} \tag{5.2}$$

n = refractive index
s = index for standard air
λ = wavelength in μm

Equation (5.2) gives the dispersion equation for standard air at 15°C and 1atm. Taking into account the pressure p and the temperature t leads to following equation:

$$(n-1)_{tp} = \frac{p(n-1)_s}{96095.43} \cdot \frac{1+(0.601-0.00972t)10^{-8}p}{1+0.0036610t} \tag{5.3}$$

t = temperature in °C
p = pressure in Pa

Additionally involving the water vapour pressure f leads to the equation (5.4) for the difference of the refractive index of moist air and dry air at the same total pressure.

$$n_{tpf} - n_{tp} = -\left(3.7345 - 0.0401\frac{1}{\lambda^2}\right) f 10^{-10} \tag{5.4}$$

f = water vapour pressure in Pa

The uncertainty of these equations in the range of 350 to 650 nm wavelength is $\pm 3 \cdot 10^{-8}$ mainly due to pressure, temperature and humidity measurements.
This equations were used to simulate the Rayleigh atmosphere for Monte Carlo radiative transfer calculations. The meteorological conditions are obtained from the COSMO-MUSCAT model. The atmospheric conditions like specific humidity, atmospheric pressure and temperature averaged over the model domain columns are shown in figure 29.
The refractive indices are calculated with the help of the equations 5.2 to 5.4. They are presented in figure 30. The refractive index of the atmosphere without aerosols correlates most with the averaged pressure field which depends mainly on the geological surface pattern

of the underlying landscape. From the refractive indices for the Rayleigh atmosphere the extinction efficiencies are calculated according to Hirsch (2005):

$$Q_{ext}(\lambda) = \frac{8\pi^3 \left[n^2(\lambda) - 1\right]^2}{3N\lambda^4} \tag{5.5}$$

Q_{ext} = extinction efficiency
λ = wavelength
n = refractive index
N = number of paricles per m^3

The extinction efficiencies are shown in figure 31 for the three wavelengths 0.6μm, 0.8μm and 1.6μm. The pattern looks the same as for the refractive index, but the absolute values are decreasing with higher wavelength.
As the extinction coefficients are needed as input for the radiative transfer calculations, thus they are calculated from the extinction efficiencies. This is done with the following equation from van de Hulst (1958):

$$\beta_{ext}(\lambda) = \int_0^\infty pr^2 Q_{ext}(r) N(r)\, dr \tag{5.6}$$

β_{ext} = extinction coefficient in m^{-1}

The scattering properties of the Rayleigh atmosphere were embedded in the COSMO-MUSCAT dust cloud to perform the Monte Carlo radiative transfer calculations.

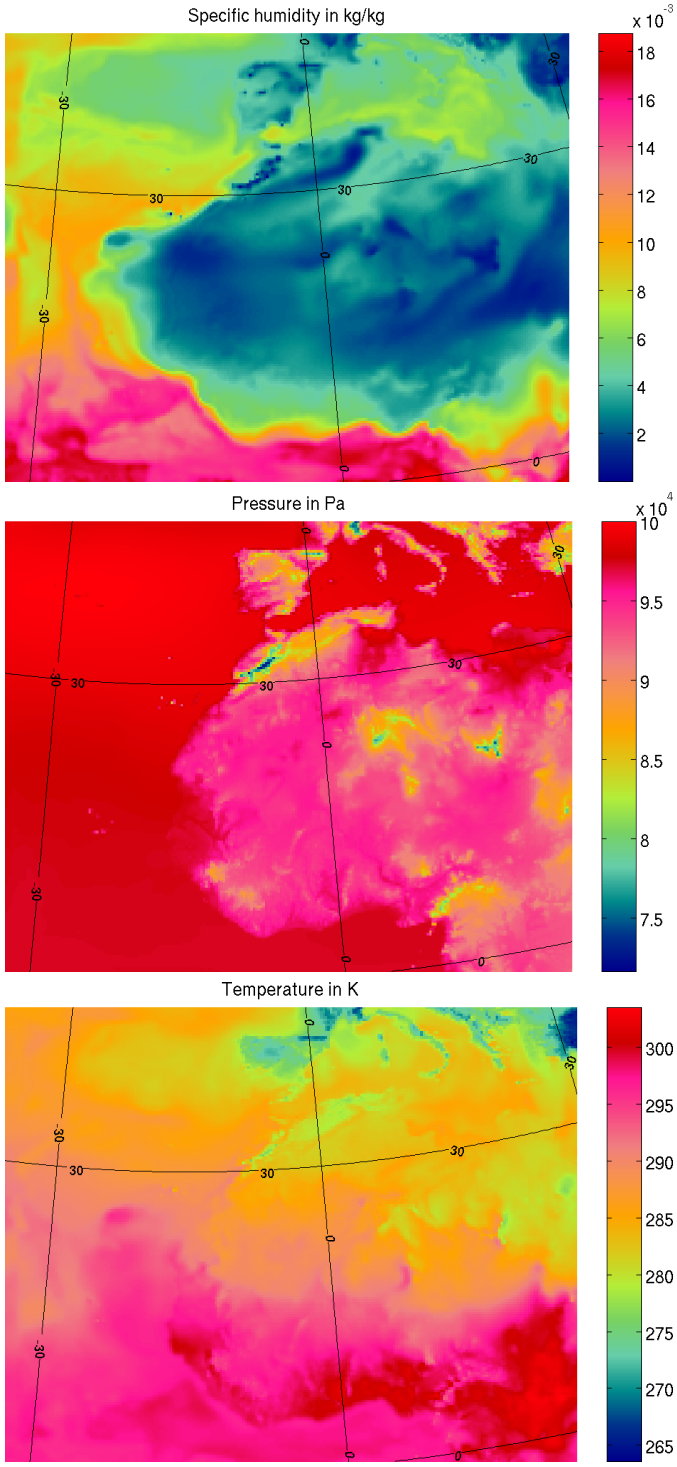

Figure 29: Conditions over the Saharan region at 31 January 2008 13:00 UTC

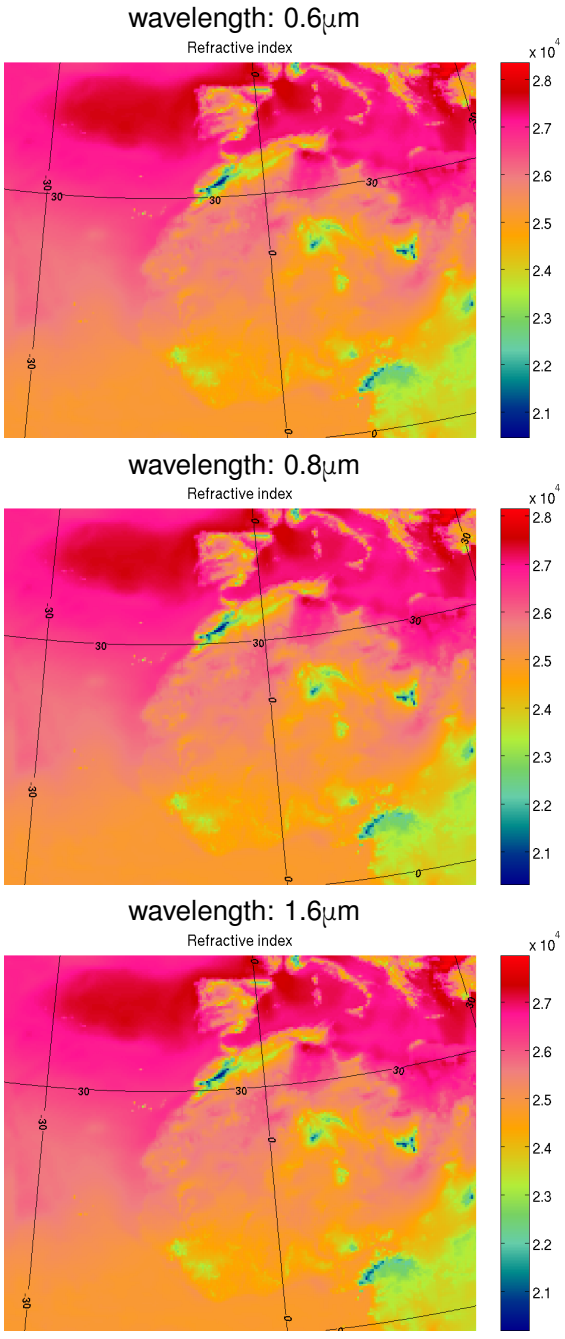

Figure 30: Rayleigh refractive indices

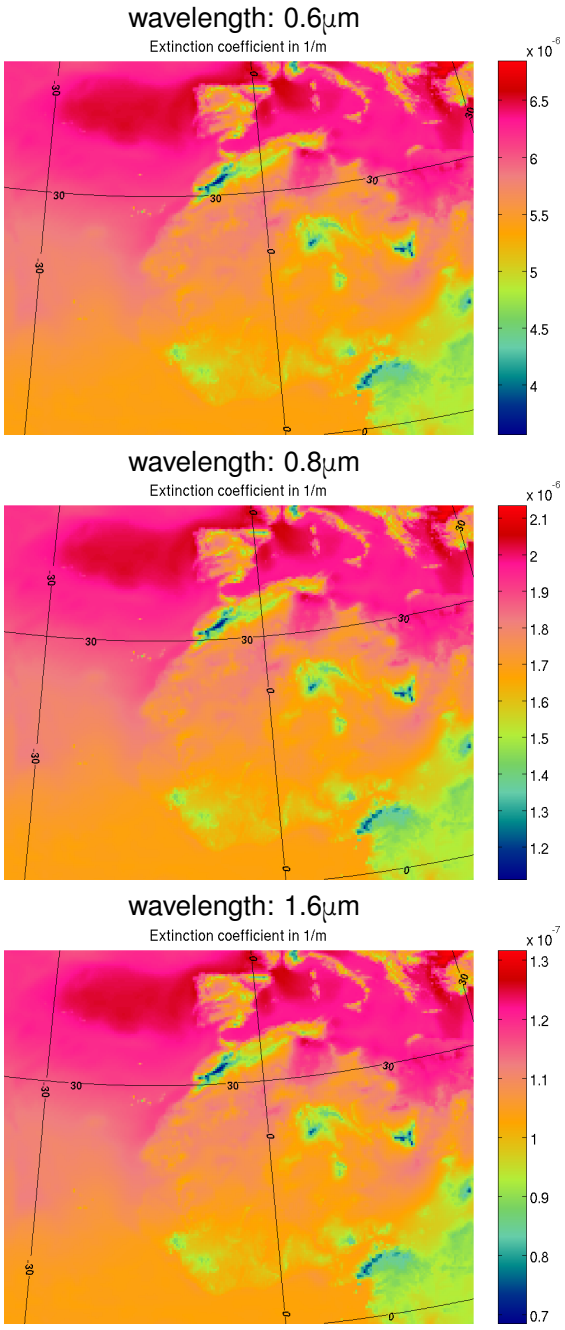

Figure 31: Rayleigh extinction efficiencies in m^{-1}

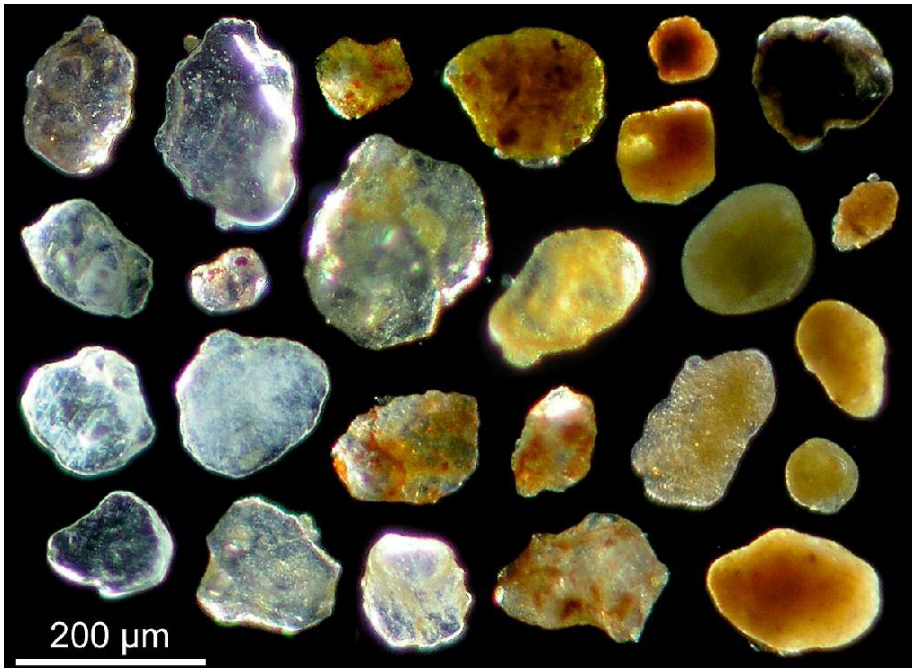

Figure 32: Variety of particle shape and color of airborne Saharan dust. (Kandler et al. (2009))

The variety of shape and color of Saharan dust particles is shown in figure 32. They are naturally formed and their shape varies from compact and rounded to thin flakes, fibres, nearly pristine crystals, and angular as well as agglomerates or aggregates.
Airborne dust plumes change their composition with live time towards smaller, less dense, and flatter (large surface-area-to volume ratio) particles. Traditionally airborne dust is treated as randomly oriented, but this might also not be true. It is possible that the particles have a preferred orientation depending on the wind direction. For that reasons the modeling of light scattering is very challenging. One big problem is, that there are no methods available to model reliable and accurately light scattering properties of irregular shaped particles at different size parameters. There are some methods which work well for small particles, but unfortunately the scattering properties are more influencing and differing for larger particles with irregular shapes. But there are models that can be tuned to agree well with with the laboratory measured reference scattering matrices.
The commonly used Mie theory should be restricted to spherical particles. (Timo and Nousiainen (2009)) It is hard to treat the physical particle properties like composition and morphology in a realistic matter. No exact analytical solution for light scattering by irregular shaped particles exist. There have to be made assumptions and simplifications to get solutions with non exact methods, but the biggest limitation of numerical methods might be the wide range of relevant particle sizes and shapes.
Thus one have to use different methods with different simplifications at different size parameters.
Testing different model approaches is difficult due to the lack of reliable and accurate scat-

tering references.
One focus of this study is the comparison of the results from the radiative transfer Monte Carlo calculations for Saharan dust clouds consisting of particles with different shapes. Also in this study different methods to calculate the single scattering properties of spherical, spheroidal and irregular shaped particles were combined. The used methods are summarized in table 7 and will be briefly explained in the following sections.

Shape	bin 1 0.166 μm	bin 2 0.501 μm	bin 3 1.514 μm	bin 4 4.571 μm	bin 5 13.804 μm	Aspect ratio
Sphere	Mie Theory					1
Spheroid	MIESCHKA			Geometric optics		1.6
Irreg. particle	Mie Theory	Geometric optics				1.6

Table 7: Used methods to calculate scattering properties for different shapes and particle sizes (extinction efficiency for Geometric Optics method was always assumed to be the same as for the corresponding sphere calculated with Mie Theory).

The Mie calculations and all following calculations are performed at 0.6μm with an refractive index of $1.574 + i0.0011$, at 0.8μm with an refractive index of $1.571 + i0.00038$ and 1.6μm wavelength with an refractive index of $1.564 + i0.00062$. But one should keep in mind that the scattering properties of dust particles are very sensitive to the refractive index and even small uncertainties on this value can have big influences on the scattering properties and thus on the calculated radiance fields. To quantify these influences more calculations with different refractive indices have to be performed, which - however - is beyond the scope of the present study.

5.2 Mie Theory

To solve the scattering problem at spheres there exists an exact method, the Mie Theory developed by Gustav Mie, a German physicist born in Rostock in 1868. In the year 1908 he published his famous work, where he described in detail how an electromagnetic wave interacts with a spherical particle. (Mie (1908))
The Mie theory is an exact method suitable for all particle sizes and refractive indices, which means that in the atmosphere it is used for aerosol particles and cloud droplets. Because the sphere is a very symmetric form, there exists an exact solution of the single scattering problem. It is the solution of the wave equations with radial symmetric boundary conditions describing the electromagnetic field vectors by spherical harmonics.
According to the Mie Theory the extinction coefficient is vise versa proportional to the wavelength with an exponent of 1.3. Thus, Mie scattering depends only weakly on the wavelength and this dependency vanishes for particles bigger than 10μm. Then the scattering is grey like in a fog or in clouds. The resulting single scattering properties for spherical particles at the wavelengths 0.6μm, 0.8μm and 1.6μm are presented in figure 33.

5.3 Geometric optics

As the Mie theory can only be used to calculate the single scattering properties of spherical particles, one has to use another method if differing forms are treated.
The numerical method of geometric optics can be used for particles in which the smallest expansion of the particle is much bigger than the wavelength of the incoming light. Thus this method can be used for large particles with shapes that are nonspherical.
With the precondition of large particles the incoming light can be treated as a light ray and the reactions with the particle is described by the particle geometry. The ray follows Snell's law and the Fresnell's equations. The result depends on reflection and refraction of the light ray in the particle. Furthermore, diffraction at the particles projected area needs to be taken into account.
The used geometric optics ray tracing model was build by Andreas Macke (**?**). This model was applied to calculate the single scattering properties of large spheroidal and irregular shaped particles. The results are presented in figure 34 and 36. The extinction efficiencies are always defined to be 2 for the paticle properties calculated with the method of Geometric Optics. But as they are required to perform the Monte Carlo radiative transfer calculations and we want to see scattering phase function dependent radiances, we assumed that they have the same values as spherical particles.

5.4 MIESCHKA

The Scattering Database for spheroidal particles (Schmidt et al. (2009)) provides scattering properties for a wide range of different particles. But as the particles properties measured in the SAMUM Campaign can not be found there with adquate acurracy, scattering at spheroidal particles has been calculated with the code MIESCHKA (Wauer et al. (2004)) via the Virtual Lab (*http://vl.nz.dlr.de/VL*) environment.
The Virtual Lab provides a variety of codes which are embedded in a comfortable user interface. There are several codes that can be used to calculate the scattering properties of different shaped particles or to perform radiative transfer calculations. MIESCHKA solves Maxwell's equations and is based on a generalization of the separation of variables method. It can be used for particles up to a size parameter of 40 where the geometry is axisymmetric. A detailed description of MIESCHKA can be found in Wauer et al. (2004).

5.5 Spherical, spheroidal and irregular shaped dust particles

Figure 33 shows the Mie scattering phase functions for 5 particle size classes with effective radius 0.166 (bin1), 0.501 (bin2),1.514 (bin3), 4.571 (bin4) and 13.804 μm (bin5). With larger radius the phase function becomes more irregular shaped and the peak in forward scattering direction is getting more pronounced.
As shown in table 7 the MIESCHKA code was used for spheroidal particles corresponding to a scattering cross section equivalent sphere with an effective radius of 0.166 (bin1), 0.501 (bin2) and 1.514 μm (bin3). The method of ray tracing with geometric optics was applied for the large spheroidal particles of bin4 with an effective radius of 4.571μm and bin5 with an

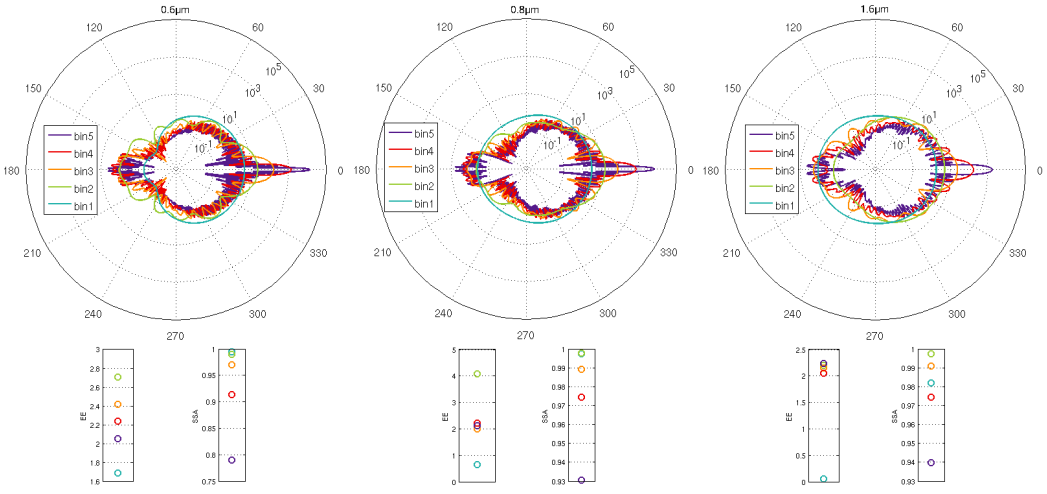

Figure 33: Mie scattering phase function, extinction efficiency [EE] and single scattering albedo [SSA] for 5 particle sizes

effective radius of 13.804 µm.

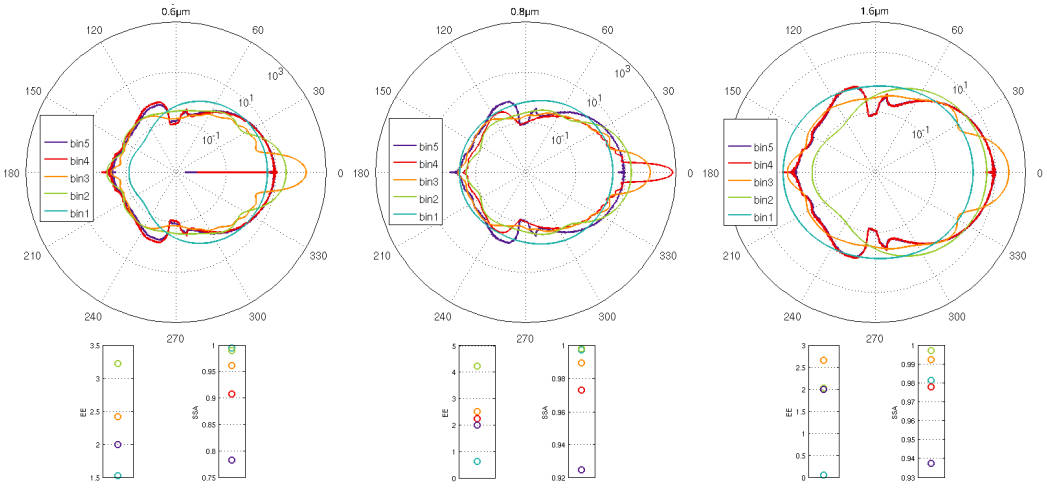

Figure 34: Scattering phase functions, single scattering albedos [SSA] and extinction efficiencies [EE] for spheroidal particles at 5 particle sizes

Figure 34 shows the scattering phase functions, single scattering albedos and extinction efficiencies for spheroidal particles for the same five size classes. According to Kandler et al. (2009) an aspect ratio of 1.6 was assumed.
To investigate the scattering properties of more realistic dust particles, irregular shaped particles were constructed. These irregular particles (example in figure 35) are randomly constructed convex polyhedrons with triangular surfaces and an aspect ratio of about 1.6.

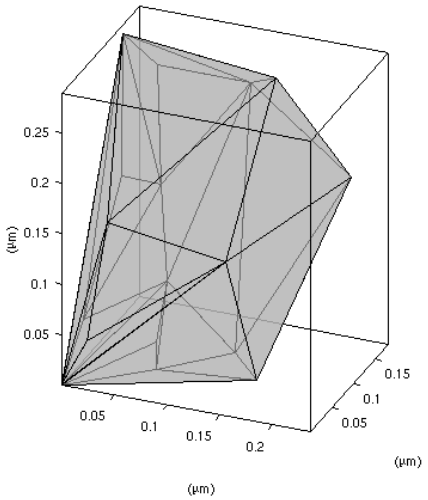

Figure 35: Example irregular particle

The ray tracing method was used to calculate the scattering properties of the irregular shaped particles that are considerably larger than the wavelength. A few hundred realizations of the random polyhedrons were considered in each size bin to calculate their scattering properties. The results are averaged for the size bins. The smaller irregular particles in the size class bin1 are to small to use the ray tracing method. For those particles the scattering properties were taken as identical to those from spherical ones. According to this assumption the scattering properties of irregular particles and spherical particles do not differ for small particles, thus all shape induced differences are caused by the deviations of the scattering properties of larger particles.
Figure 36 shows the scattering phase functions for irregular shaped particles for the 5 size classes. With bigger radius the peak in forward scattering direction is getting more pronounced.

To study the role of different particle shapes and their influence on the simulated radiation fields, first the differences in single scattering properties of the single particles have to be pointed out.
In this study the scattering properties for three different shapes of spherical, spheroidal and irregular shaped particles have been compared. Later the single particle properties are combined to the scattering classes (chapter 5.7) to obtain the scattering properties for a realistic Saharan dust cloud. The particle properties are obtained from the SAMUM community by measurements and simulations.
The different shaped particles were taken in the way that the amount of particles in the cloud did not change and all particles have the same mean projected area. This has the consequence that the volume of spheroidal particles is 3% smaller than that of spheres.
The following results are from calculations at a wavelength of 0.6µm. The results from the

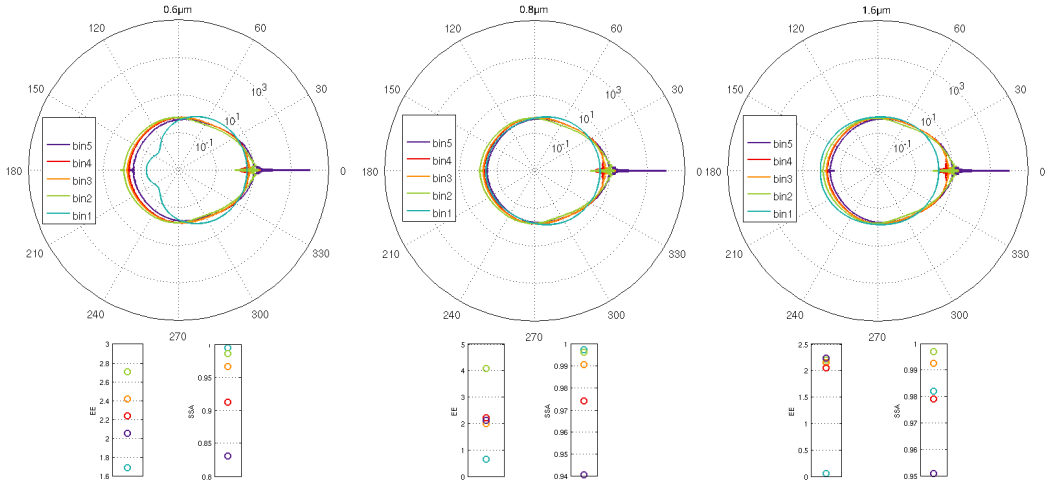

Figure 36: Scattering phase functions, single scattering albedos [SSA] and extinction efficiencies [EE] for irregular shaped particles at 5 particle sizes

calculations at the wavelengths 0.8 and 1.6µm are presented in chapter 8.
The extinction efficiency and the single scattering albedo of spherical, spheroidal and irregular shaped particles are compared in figure 37.

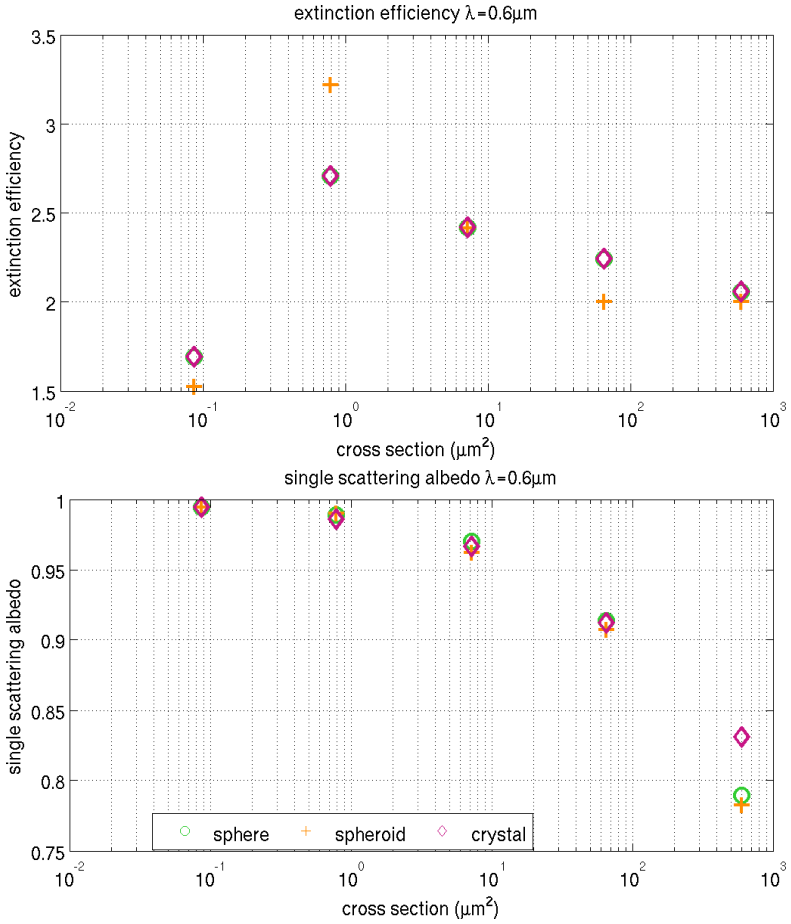

Figure 37: Extinction efficiency and single scattering albedo for spherical, spheroidal and irregular shaped particles with different cross sections

The extinction efficiency for spheres and irregular shaped particles was assumed to be the identical as noted above. The values for the extinction efficiency for spheroidal particles in figure 37 show that they are altering compared to the ones for spheres. For a scattering cross section of $0.087\mu m^2$ the value for spheroids is smaller, but for a cross section of $0.789\mu m^2$ it is the other way around. So for single particles there is no consistent tendency in the differences between spherical and spheroidal particle extinction efficiency.
For the single scattering albedo of the particles with different shapes no significant shape induced differences are found. The values of the single scattering albedo decreases for all shapes with larger particle size.
In figure 38 the scattering phase functions of the three particle shapes (spherical, spheroidal and irregular) are plotted.
Large shape-induced differences are obvious in the scattering phase functions, displayed in figure 38. For smaller particles the scattering phase functions do not differ very much from each other, but they do more with increasing particle size. The scattering phase functions

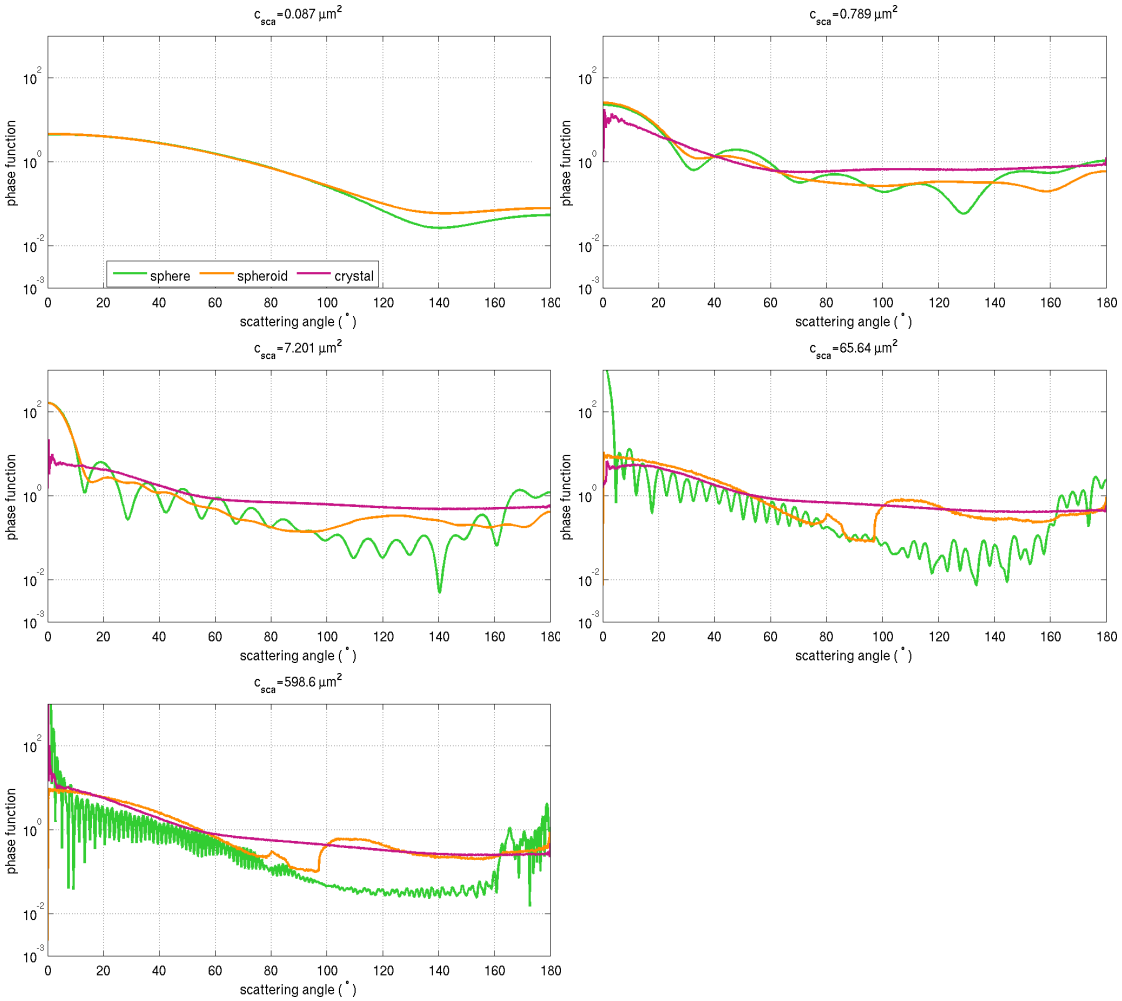

Figure 38: Single scattering phase function for spherical, spheroidal and irregular shaped particles with different cross sections

have a very special angular pattern for each particle shape. All shape-induced differences in scattering properties increase with particle size.

5.6 Comparison with laboratory measurements

Measurements of scattering properties of aerosols are presented in the Amsterdam Light Scattering Database (Volten et al. (2006)).
It contains the measured scattering matrix elements as functions of the scattering angle for aerosol particles in random orientation at 0.4416 and 0.6328 μm wavelength. It provides a variety of aerosol samples like volcanic ash from 3 different volcanoes, feldspar, red clay, quartz, loess, forestite samples, 15 phytoplankton species, two types of silt suspended in water and Saharan dust. These samples have a wide range of particle size and complex refractive index. The database is given in tabular form to be easily used for further research purpose.
For this study the database was used to compare the calculated scattering matrix elements of spheres, spheroids and irregular particles with the measured elements for Saharan dust samples.
Scattering matrices contain all polarization properties of the particles. For definition the fact is used, that the flux and polarization of the incoming light beam can be represented by a column vector $\pi\Phi = \pi\{\Phi_1, \Phi_2, \Phi_3, \Phi_4\}$, which is called a flux vector. (Hovenier (2011))
If a light beam is scattered the incoming light beam and the scattered beam are related by a 4×4 scattering matrix.

$$\Phi = \frac{\lambda^2}{4\pi^2 D^2} \begin{pmatrix} F_{11} & F_{12} & F_{13} & F_{14} \\ F_{12} & F_{22} & F_{23} & F_{24} \\ -F_{13} & -F_{23} & F_{33} & F_{34} \\ F_{14} & F_{24} & -F_{43} & F_{44} \end{pmatrix} \Phi_0 \tag{5.7}$$

Here $\pi\Phi_0$ and $\pi\Phi$ are the flux vectors of the incident and scattered light beams, λ is the wavelength and D is the distance from the particles to the detector. The scattering matrix element F_{11} is the scattering phase function, which was introduced before. The ratio $-F_{12}(\Phi)/F_{11}(\Phi)$ is the degree of linear polarisation of the scattered light. (Hovenier (2011))
The measurements were performed at a wavelength of 0.6328 μm with a particle size distribution resulting in an effective radius of 8.2μm. The real part of the refractive index has a range from 1.5 to 1.7, so for the calculations a value of 1.6 was used. The imaginary part of the refractive index goes from 10^{-2} to 10^{-5} and $5 * 10^{-3}$ was used for the calculations. (Volten et al. (2001))
The scattering matrix elements for the spherical particle are obtained by Mie Theory in the Virtual Lab (http : //vl.nz.dlr.de/VL) (Wauer et al. (2004)). The elements for spheroids and irregular particles with an aspect ration of 1.6 are calculated with the ray tracing method with programs for spheroids and irregular polyhedrons by Macke et al. (1995) and Macke and Mishchenko (1996). The irregular shaped particles are shown in figure 39. The variety of irregular shaped particles is very big, so the three irregular particles used here are treated as representative for irregular shaped polygons.

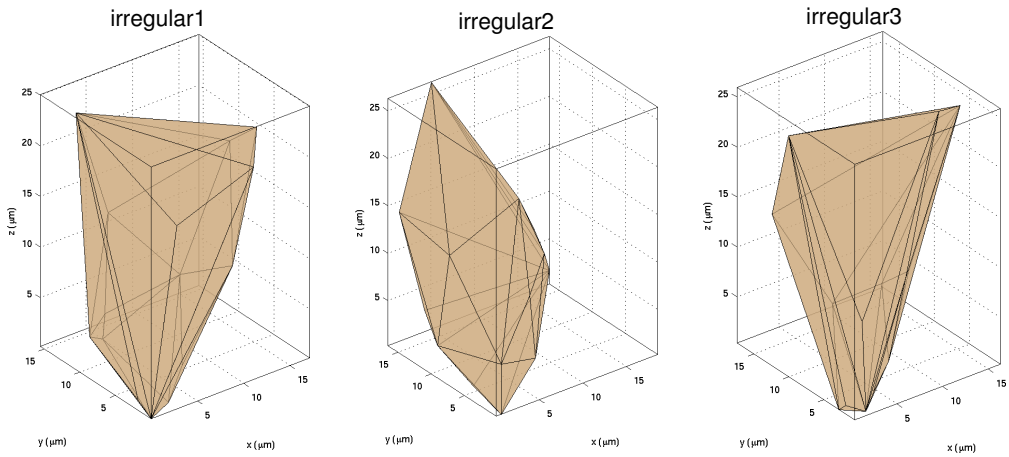

Figure 39: Representatives of irregular shaped polygons with an aspect ratio of about 1.6

In figure 40 is shown the comparison of the scattering matrix elements for spheres, spheroids, irregular shaped particles and laboratory measurements for dust particles at 0.6328 µm. It seems that the irregular shaped particles correspond a little better with the measurements than spheres or spheroids. Also additional calculations with other refractive indizes could agree better with the measurements.
To see better which of the particles fits best to the measurements of the scattering matrix elements, table 10 shows the mean deviation and the correlation coefficient of the measurements to all shape calculations. Marked in red are worst fitting cases and marked in green, the best fitting cases. The conclusion from figure 39 and the table is, that none of the scattering matrix elements calculated for different shapes fits very good to the measurements. But in most cases the irregular shaped particles fit better than spheres or spheroids.
One has to keep in mind that these measurements were performed on particles with an effective radius of 8.2µm. This rather large effective radius is caused by the origin of the dust samples. They are collected from the dust source surface. Airborne dust has a smaller effective radius which varies with the distance to the dust source region. But roughly can be said that it mainly lies in a range from 2 to 3 µm. And the larger the particles the bigger are the shape induced differences in the scattering properties.

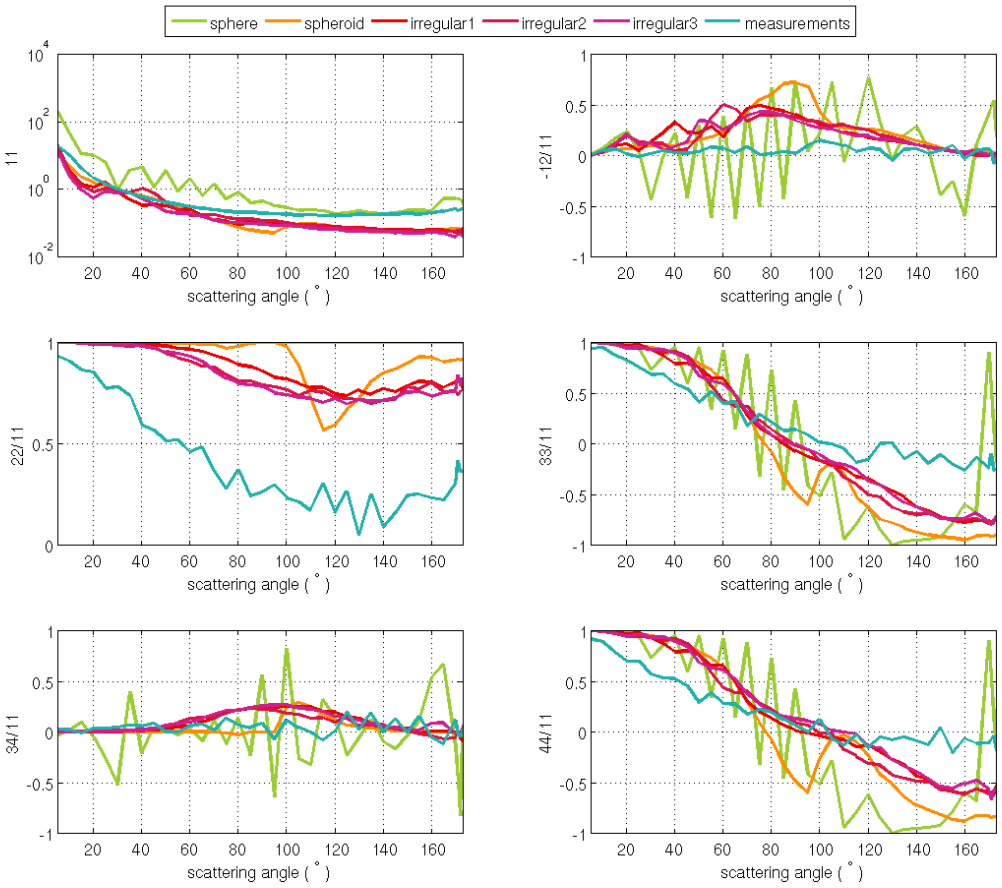

Figure 40: Comparison of the scattering matrices of laboratory measurements to simulations for different particle shapes

		sphere	spheroid	irregular1	irregular2	irregular3
F11	md	544.04	-43.783	-40.888	-28.826	-50.972
	cc	0.96172	0.99393	0.9644	0.94002	0.94815
-F12/F11	md	126.76	425.63	346.67	352.94	318.71
	cc	0.14644	0.25488	0.26541	0.33631	0.28285
F22/F11	md	145.33	124.53	113.45	104.91	104.4
	cc	NaN	0.54775	0.86234	0.91556	0.92815
F33/F11	md	-75.849	-147.17	-85.515	-94.658	-80.217
	cc	0.74352	0.95377	0.96645	0.96313	0.96341
F34/F11	md	-151.14	-14.719	111.77	83.601	151.22
	cc	0.041801	-0.017412	0.097263	0.19639	0.01429
F44/F11	md	-73.664	-107.03	-29.246	-37.19	-10.619
	cc	0.75428	0.9017	0.92597	0.92939	0.91817

Table 10: Mean deviation (md) and correlation coefficient (cc) of the calculated scattering matrix elements of different particles compared to the measured scattering matrix elements

5.7 Scattering classes for different shaped particles

Since the modelled domain from the COSMO-MUSCAT for the clouds from the year 2008 consists of 182×229 horizontal boxes and 40 vertical layers, there are over 1.5 million dust cloud boxes. To perform the 3D Monte Carlo radiation transport calculations, for each box the scattering properties (extinction efficiency, single scattering albedo) including the scattering phase functions with an adequate scattering angle resolution are required.
Handling these amount of data and importing it for the 3D Monte Carlo calculations needs a lot of computing time and memory. To solve this problem the size and shape dependent scattering properties have been discretized into 14 classes.
20 LM-MUSCAT-DES dust clouds from the modelled period 2006 and 2008 were used for the scattering classes:

- 2006: 19.05. 12:00, 20.05. 12:00
- 2008: 19.01. 10:00-15:00, 25.01. 10:00-15:00, 28.01. 10:00-15:00 (hourly)

Each cloud box has a different particle size distribution with 5 size classes with following radii:

	radius range	effective radius
bin1	$0.100-0.288\mu m$	$0.166\mu m$
bin2	$0.288-0.871\mu m$	$0.501\mu m$
bin3	$0.871-2.630\mu m$	$1.514\mu m$
bin4	$2.630-7.943\mu m$	$4.571\mu m$
bin5	$7.943-23.988\mu m$	$13.804\mu m$

Table 11: sizeclasses

So one has to find significant properties in the size distribution which mainly influence the scattering properties. First the boxes were grouped into 5 classes depending in which of the 5 size classes the largest number of particles is located. In table 12 these parting is shown.

bin1	bin2	bin3	bin4	bin5
91.92	3.47	2.76	1.81	0.03

Table 12: parts of boxes in %

Table 12 shows that the amount of dust cloud boxes which have their highest amount of particles in bin1 is over 90% of the boxes. Thus in over 90% of the boxes the amount of small particles from the size class bin1 with an effective radius of $0.166\mu m$ is bigger than that of the size classes with larger particles. These 90% of the boxes were split up into 10 additional subclasses.
The ratio between small and large particles is an appropriate measure for the scattering properties of one grid box with a given discrete size distribution. But the biggest particles are the size class bin5 and here often the amount of particles is not enough to get a good

indicator, so the next smaller size class bin4 was used for the ratio. And with a closer look at the ratio between the third roots of the size bins, there the correlation between scattering properties and the ratio r is even higher.

$$r = \frac{\text{number of particles in bin4}^{\frac{1}{3}}}{\text{number of particles in bin1}^{\frac{1}{3}}}$$

The ratio r is between 0 and 1, so the additional 10 classes result by parting the ratio between 0-0.1, 0.1-0.2, 0.2-0.3,...,0.9-1.
Finally there are 14 scattering classes for the dust cloud boxes. The proportions of the cloud boxes of the 20 LM-MUSCAT-DES clouds are categorized into the 14 scattering classes as shown in table 13.

Biggest particle amount in size	Ratio between big and small particles	Occurrence of scattering class in dust cloud boxes	Composition of the scattering classes in %					effective radius (μm)	Name
			bin 1 0.166 μm	bin 2 0.501 μm	bin 3 1.514 μm	bin 4 4.571 μm	bin 5 13.804 μm		
bin 1	0.0-0.1	in %14.31	61.82	36.10	2.03	0.05	0.00	2.098	1.1
	0.1-0.2	67.38	60.85	36.53	2.47	0.14	0.00	2.866	1.2
	0.2-0.3	6.97	56.92	37.02	5.24	0.81	0.01	5.887	1.3
	0.3-0.4	1.89	52.38	35.03	10.43	2.13	0.03	6.416	1.4
	0.4-0.5	0.99	45.22	33.11	17.64	3.97	0.07	6.936	1.5
	0.5-0.6	0.51	37.32	31.18	25.4	5.96	0.11	7.065	1.6
	0.6-0.7	0.05	32.62	29.22	30.48	7.50	0.18	7.657	1.7
	0.7-0.8	0.00	46.94	19.41	13.51	19.24	0.90	9.633	1.8
	0.8-0.9	0.00	44.99	20.46	6.53	26.74	1.28	9.744	1.9
	0.9-1.0	0.00	39.43	11.48	12.98	34.63	1.48	9.469	1.10
bin 2		3.47	34.77	56.39	7.68	1.14	0.01	5.353	2
bin 3		2.74	14.98	21.25	53.49	10.10	0.18	6.895	3
bin 4		1.81	0.00	0.00	0.00	99.59	0.40	5.475	4
bin 5		0.03	0.00	0.00	0.00	0.00	100.00	13.804	5

Table 13: Development and composition of the 14 scattering classes as described in chapter 5.7. Bin1 to bin5 are 5 size classes with corresponding effective radius.

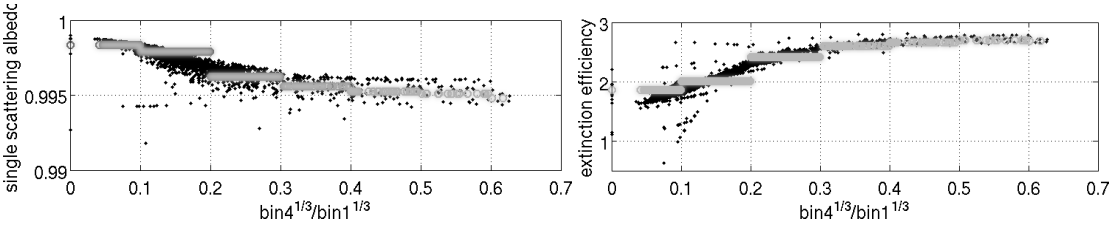

Figure 41: Extinction efficiency and single scattering albedo at 1.6μm calculated exact for each cloud box with Mie theory (black dots) and the discretized values in grey circles.

For the 14 classes the averaged optical properties of the classified boxes were taken. This provides a useful discretization and makes the great amount of data manageable and comparable.
Figure 41 shows the discretized extinction efficiency and single scattering albedo for spherical particles. The values with black dots are calculated with Mie Theory for all dust cloud boxes and the grey circles show the chosen average values for the corresponding classes. The discretization is assumed to sufficiently represent the micro-physical and thus optical variability in the 3D radiative transfer calculations.

Scattering properties for different shapes The scattering properties calculated by different methods for spherical, spheroidal and irregular shaped particles at certain effective radii are now combined to obtain the scattering properties of the scattering classes. The calculations in this paragraph are exemplary shown for a wavelength of 0.6μm. For the results of other wavelengths (0.8 and 1,6μm) see the appendix in chapter 8.

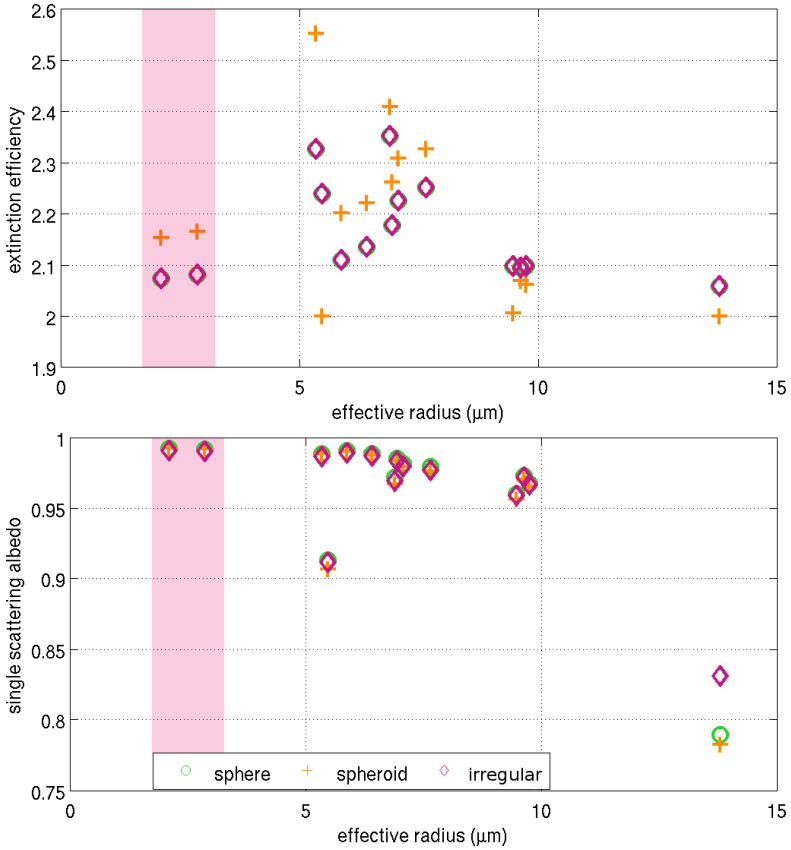

Figure 42: Extinction efficiency and single scattering albedo for spherical, spheroidal and irregular shaped particle scattering classes with different effective radii

In figure 42 the single scattering albedo and the extinction efficiency for the scattering class averages are displayed. To each scattering class corresponds a certain effective radius, which is on the x axis. Over 80% of the dust cloud boxes are in the pink shaded region, most boxes are in the two classes with small effective radius.

The extinction efficiency for spheroid particles is about 0.1 higher than the value for spheres and irregular particles. This results in higher optical thickness for clouds with projected area equivalent spheroidal particles. The extinction efficiencies of irregular particles do not differ from the ones for spherical particles because of the approximation that they are equal.
The imaginary part of the refractive index is very low in the considered wavelength range. At 0.6μm the dust particles have an refractive index of $1.574 + i0.0011$. That's why the absorption is low and the scattering albedo is very high. Thus there are only small differences in the single scattering albedo for the three particle shapes. The values for spheroids and irregular particles differ by less than 1% from the single scattering albedo of spheres. In the study by Otto et al. (2009) which deals with radiative transfer calculations for dust clouds consisting of spherical and spheroidal dust particles it is also shown, that at a wavelength of 0.6μm the differences between spheroids and spheres are small.
The single scattering albedo is about 0.5% lower for spheroids than for spheres, but the values reported by Otto et al. (2009) are smaller in general. This may mainly be caused by different input data for particle size distributions and refractive index due to measured data at different time and location.
The work of Yang et al. (2007) also shows that the single scattering albedo from spheres and spheroids show only small differences, with slightly smaller values for spheroids.
There are other studies on the topic of particle shape like Kalashnikova and Sokolik (2004) dealing with mixtures of different shapes based on electron microscopy data. They show, that for different shapes the differences with respect to spherical particle vary even in sign and increase with particle radius.
Fu et al. (2009) obtain the result that the single scattering albedo of spherical and spheroidal particles differ by less than 1%. In Kalashnikova and Sokolik (2002) the scattering properties of mixtures of sharply edged, smooth shapes and spheres are compared. They found larger single scattering albedo for mixtures with more sharp-edged particles.

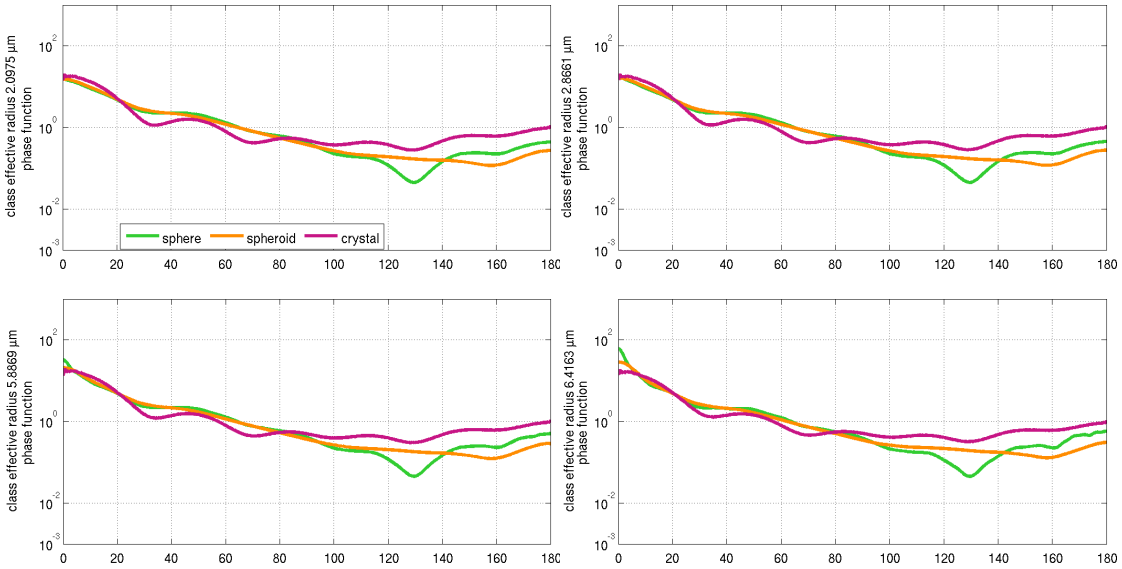

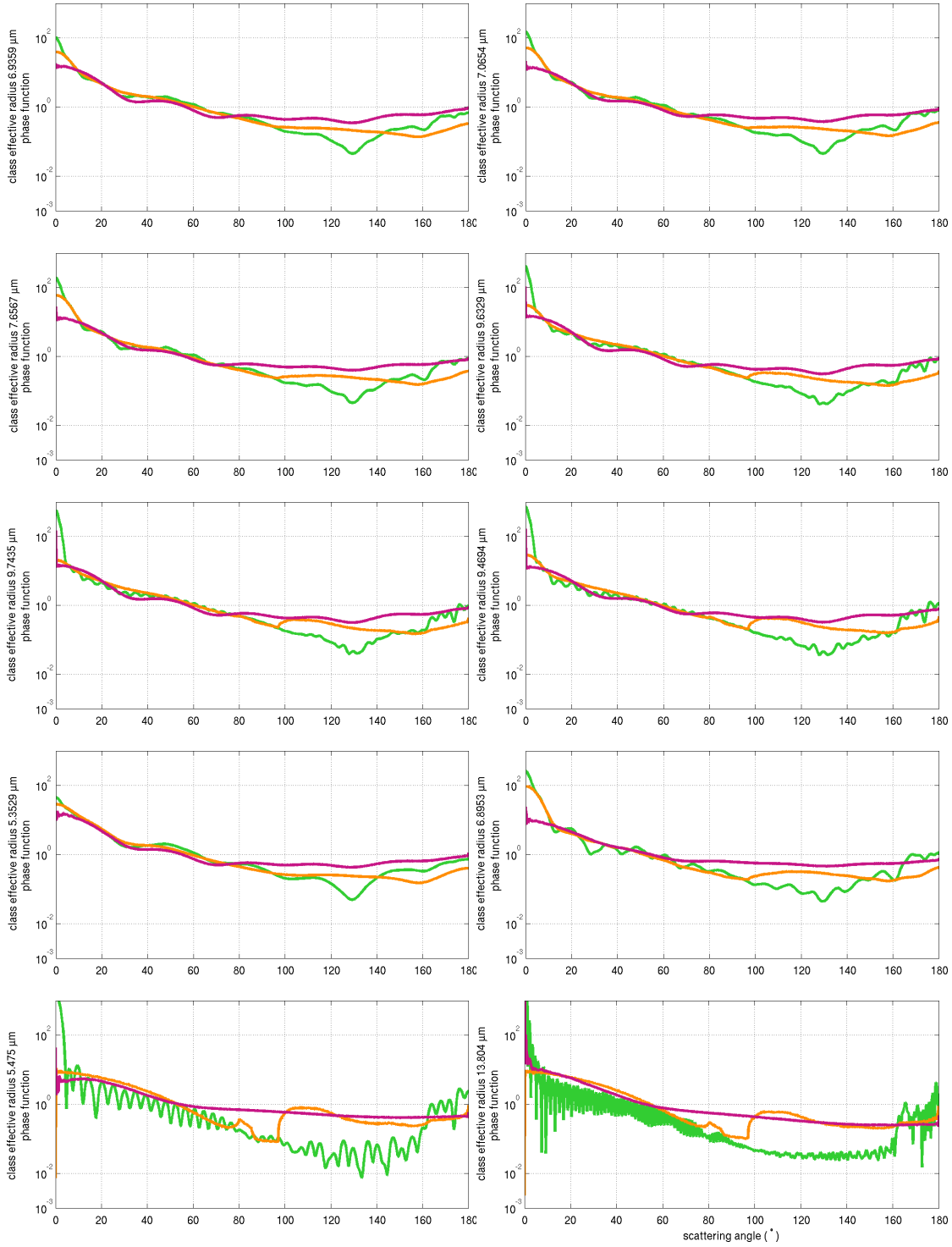

Table 15: Single scattering phase function for spherical, spheroidal and irregular shaped particle scattering classes with different effective radii

The scattering phase functions plotted in table 15 are calculated at 0.6μm wavelength. For other wavelengths look at the appendix in chapter 8. The shape induced differences in the phase functions are more pronounced than in the other scattering properties. The two upper diagrams with an effective radius of 2.0975 and 2.8661μm cover over 80% of the dust cloud boxes. Most obvious is the different shape of the phase function of spheres compared to the ones for spheroids and irregular particles, especially in the region of a scattering angle from 100 to 160° with a maximum in a smaller region at about 130°. In Yang et al. (2007) these differences can also be found although they are less pronounced. In the next paragraph is investigated how the already treated scattering properties of different shaped particles proceed to the radiative properties of a realistic Saharan dust cloud.

6 Radiative properties of dust clouds

This chapter is focused on the radiative fields produced by dust clouds.
The modelled fields from MC-UniK are compared to the measured fields from the MSG satellite. Although the comparison is difficult due to the uncertainties in the modelled dust spatial distribution and in the scattering properties, in some cases good agreement could be found.
Also the pattern of the modelled irradiance from the COSMO-MUSCAT model and the modelled radiance field from MC-UniK were opposed. Here good agreement could be found because the basics, the dust particle size distributions, are exactly the same.

6.1 MC-UniK vs. MSG measurements

The output of the COSMO-MUSCAT model from 31 January 2008 13:00 UTC was used to perform radiative transfer calculations. From the modelled particle size distribution the optical properties of the dust cloud boxes were calculated for three different particle shapes. The Monte Carlo model MC-UniK (Macke et al. (1999))was used to calculate normalized radiances for the COSMO-MUSCAT dust cloud. The normalized radiances are multiplied with the narrow band solar constant for each channel of SEVIRI (Clerbaux (2006)). The results are compared with the measurements of the MSG satellite.

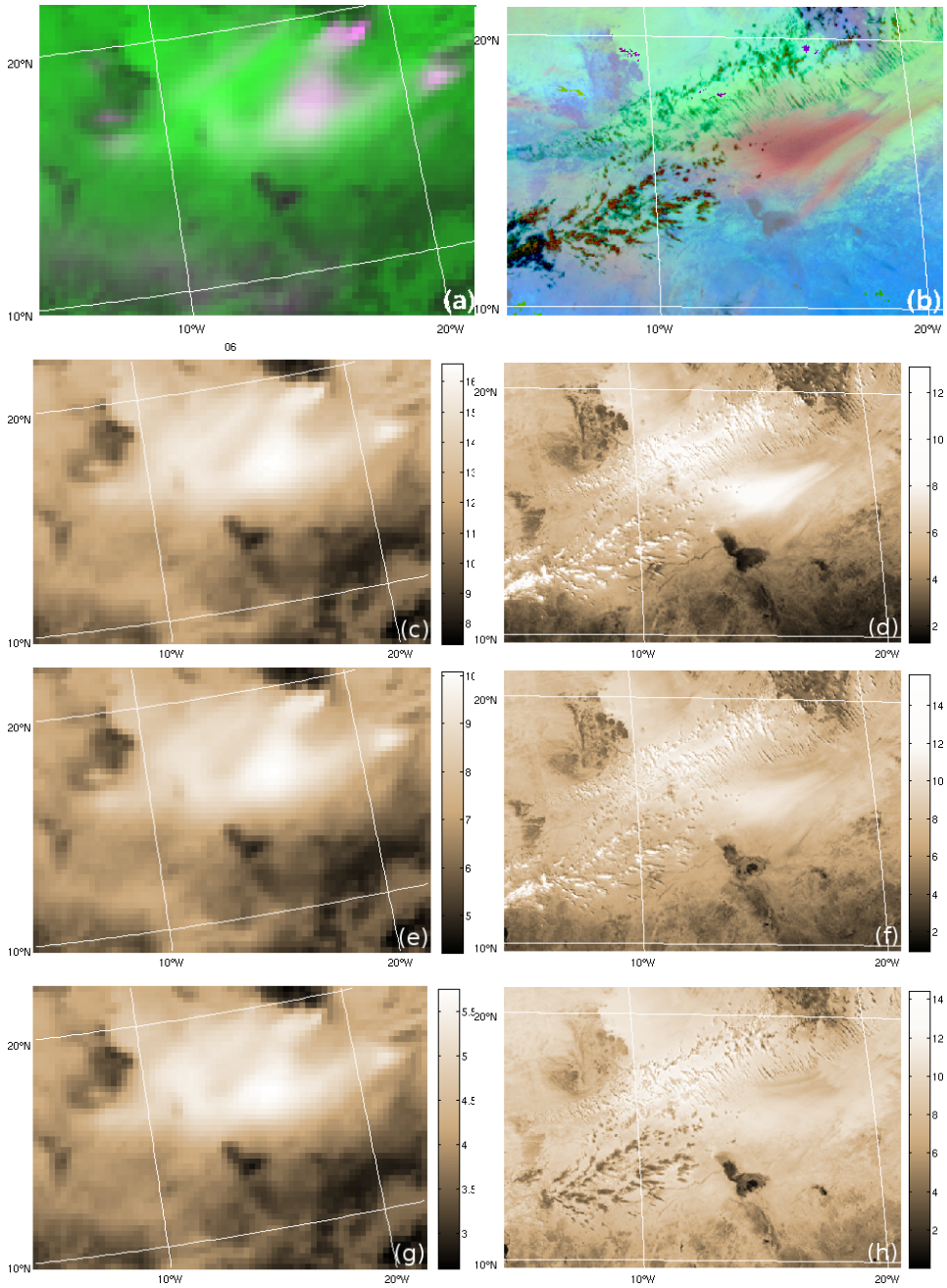

Figure 43: The Monte Carlo simulated part of the dust Cloud from 31 January 2008 13:00 UTC. (a) MUSCAT cloud (b) IR Index from the MSG satellite (c) MC-UniK simulated normalized radiance for spherical particles at 0.6 µm ((e): 0.8 µm, (g): 1.6 µm) (d) measured radiance from MSG around the 0.6 µm channel (f): 0.8 µm (h): 1.6 µm) in $W/m^2/sr$ colorbar is a little shifted because of the highly reflecting water clouds which not occur in the model.

Figure 43 shows the comparison. (a) presents the modelled COSMO-MUSCAT cloud, while (b) shows the IR-Index of MSG for the same scene. The IR-Index indicates the dust in pink to red colours.
The radiances from MC-UniK for a cloud with spherical particles and the measured radiance from the satellite (channel 1 of the SEVIRI instrument) at the wavelength of 0.6 μm are illustrated in (c) and (d). (e) and (f) show the same for a wavelength of 0.8 μm and (g) and (h) for 1.6 μm. The modelled and measured radiance patterns agree quite well at a wavelength of 0.6 μm, and at 0.8 μm also the pattern of the dust cloud can be recognized. At a wavelength of 1.6 μm the dust cloud can be clearly seen in the modelled radiance field, but in the satellite measurement it is not visible. And the absolute values in all wavelengths differ very much.
If we look at the modelling results for spheroidal and irregular particle shapes presented in figure 44, for spheroidal particles in the left column the results fit even worse in all cases except at 1.6 μm. The right column shows the radiances for irregular shaped particles and the radiance at 0.8 μm seems to fit quiet good to the measured dust pattern.

Summarizing the results, at 0.6 μm wavelength the modelled cloud with spherical particles fit best to the satellite observations, although the absolute values are significant higher. At a wavelength of 0.8μm the radiance field of the dust cloud with spherical particles fits good with the pattern and also the absolute values show good agreement. The modelled radiance for a cloud consisting of irregular particles also fits good to the measurements. The radiance field for the dust cloud with spheroidal particles do not agree with the measurements at 0.6 μm and 0.8 μm. But if we look at the satellite measurements at 1.6 μm it seems that here the spheroidal particles fit better than spherical or irregular shaped particles in the radiance pattern. But all show lower values in general. Although the dust cloud is slightly shifted, satellite measurements and model results show a similar pattern at a wavelength of 0.6 μm and 0.8 μm. But the absolute values differ in most cases. The assumption of spherical particles seems to fit best to the satellite measurements.
It is difficult to quantify the similarities because the radiances are modelled at a fixed wavelength of 0.6 μm whereas the radiances from satellite are measured at weighted wavelength around the channels centre wavelength (channel 1: 0.6 μm, channel 2: 0.8 μm, channel 3: 1.6 μm). The weighting could cause big differences especially in the absolute values of the modelled radiance. Also the presence of water clouds in the measured field causes deviations, because in the modelled field there are no water clouds considered.
Another big uncertainty are the particle scattering properties. Even small deviations in for example the single scattering albedo of the particles can cause big differences in the resulting radiance, especially in region with high optical thickness. Another very big problem is the uncertainty of COSMO-MUSCAT. By comparing the modelled dust cloud to the IR images based on MSG satellite measurements, the spatial and temporal resolution of the clouds often are not in agreement. And one has also to rely on the modelled vertical cloud distribution, which also might not match to reality in certain cases.
With the big uncertainties in the modelled dust cloud, it is hard to say if the modelled optical thickness fits to the reality. A detailed description of the validation of the COSMO-MUSCAT

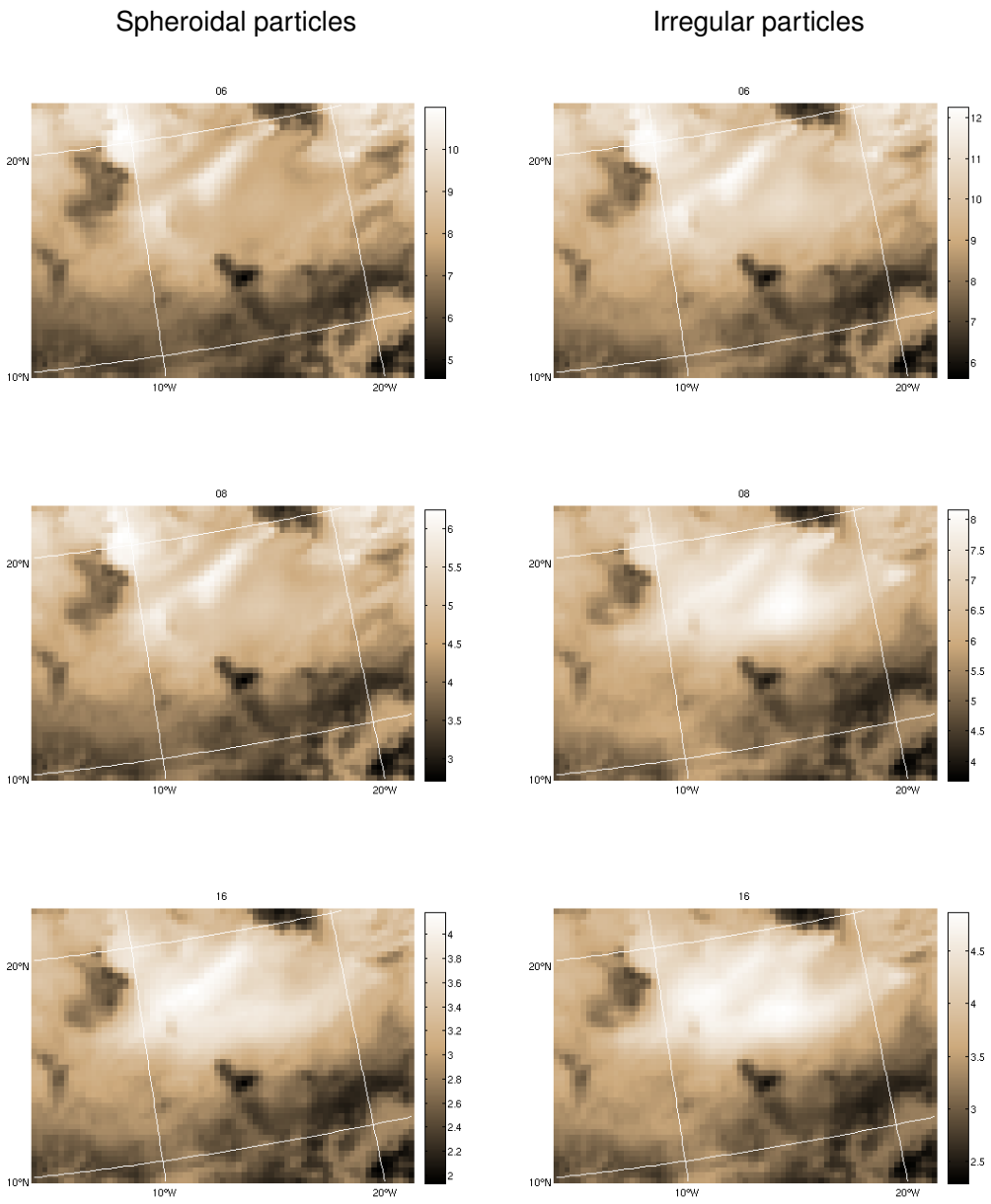

Figure 44: The Monte Carlo simulated part of the dust Cloud from 31 January 2008 13:00 UTC. MC-UniK simulated radiance for spheroidal (left column) and irregular shaped (right column) particles at 0.6μm (first row), 0.8μm (second row) and 1.6μm (third row)

model can be found in Heinold et al. (2011b).
There is concluded, that the dust transport patterns especially on 31 January 2008 is reproduced well by the model, but in some areas the optical thickness could be over- or underesti-

mated depending on not fully captured meteorological conditions in some local regions. But if the modelled optical thickness of a dust clouds differ much from the real optical thickness, of course the modelled radiative fields have big deviations from the satellite measurements. As the dust cloud from 31 January 2008 is the dust cloud which is reproduced best by the model and even the big amount of dust downwind the Bodélé Depression is represented well, this day was chosen for the radiative transfer calculations in this study.

6.2 Radiative transfer calculations of COSMO-MUSCAT and MC-UniK

The COSMO-MUSCAT model can also perform radiative transfer calculations. How the radiative transfer is realized in the model is briefly described in chapter 2 and shown in detail in Heinold et al. (2011a).
In figure 45 on the left picture is shown the field of reflected irradiance calculated by COSMO-MUSCAT. Because in the COSMO-MUSCAT radiative transfer calculations water clouds are accounted for, which do not occur in the Monte Carlo radiative transfer calculations the radiative fields look very different for both models. With the help of cloud cover data from COSMO-MUSCAT, the pixels with water clouds have been excluded. The pixels are whitened as shown in the right picture from figure 45.
The corresponding results of the Monte Carlo radiative transfer simulations the dust cloud consisting of spheroidal (left picture), spheroidal (middle picture) and irregular shaped (right picture) particles are presented in the row below. The correlation coefficients are 0.9531 for the cloud with spherical particles, 0.9069 for the cloud with spheroidal particles and 0.9310 for the cloud with irregular shaped particles. As the radiative transfer calculations in COSMO-MUSCAT are realized with the assumption of spherical particles the results look like they were expected.

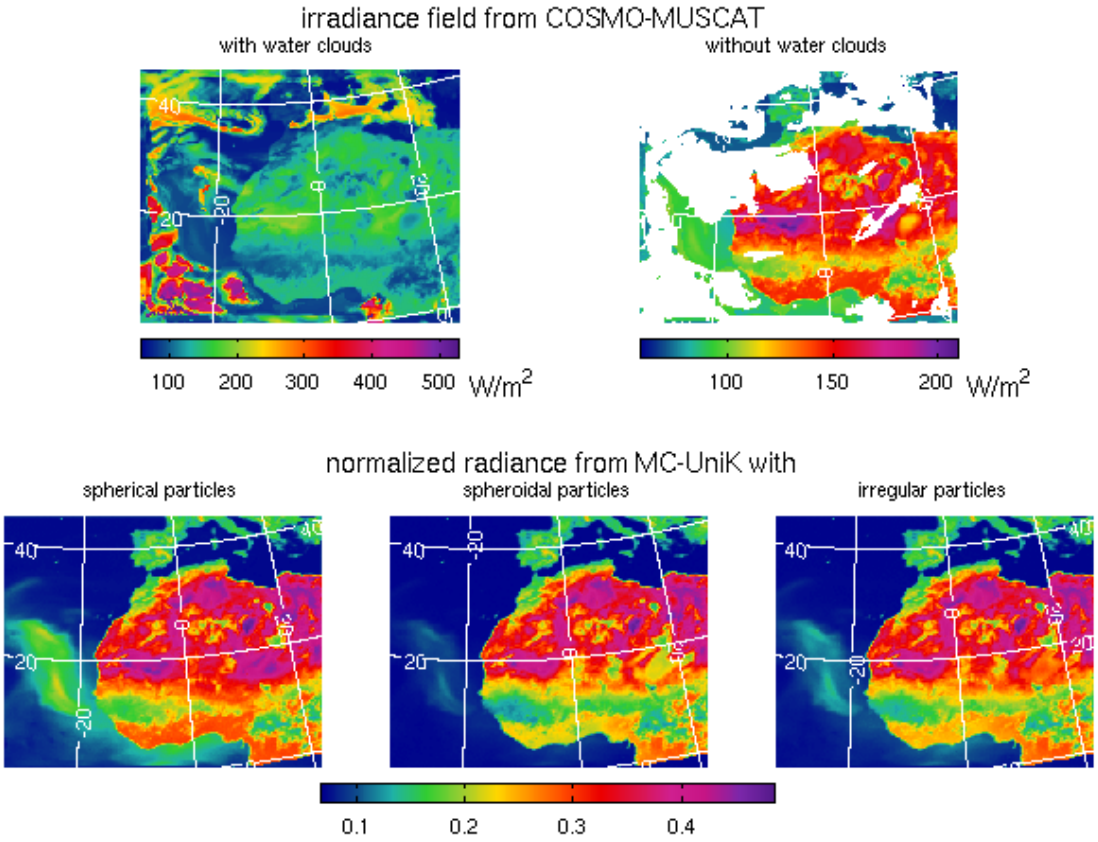

Figure 45: First row: Irradiance field as calculated from the COSMO-MUSCAT on the left side with cloud pixels and on the right side with cloud pixels excluded.
Second row: MC-UniK normalized radiances at a wavelength of 0.6μm for the dust cloud consisting of spheroidal (left picture), spheroidal (middle picture) and irregular shaped (right picture) particles.

6.3 Horizontal photon transport

Large scale and high resolution three-dimensional radiative transfer simulations are very expensive in computing time. A commonly used approximation for the 3D radiative transfer is the so-called Independent Pixel Approximation (IPA), where the results of 1D radiative transfer calculations are added column by column to approximate the domain averaged radiative fluxes or radiances. The only differences in 3D and IPA is the negligence of horizontal photon transport in the IPA. In this study full 3D and IPA calculations for a 3D dust cloud with a sun zenith angle of 33° at 31 January 2008 13:00 UTC have been performed.
The model domain shown in figure 46 has a width of about 1800 km. In order to resolve 3D effects, the grid box size was refined from 26 km for the COSMO-MUSCAT cloud to 6 km for the Monte Carlo calculations.
In figure 46 the simulated reflectivity field at the cloud for 1D and 3D calculations is presented. The first row shows the optical thickness of the cloud at 0.6 μm and the gradients of the optical thickness. The Sun direction is indicated by the yellow arrow on the right side of the domain.
The fields of the first column in figure 46 are calculated with only vertical photon transport (IPA-1D) and in the second column with additional horizontal photon transport (3D). The domain averaged values of the fields of normalized reflected radiance, absorption, transmission and reflection do not show significant differences between the 3D and IPA-1D calculations.
In the third row the differences from 3D-1D in % are plotted. Depending on the cloud structure local deviations are clearly visible. In the case of 3D the edges of the radiative fields in the dust cloud are smoothed out due to the horizontal photon transport.
Where the gradients in optical thickness of the dust cloud are largest, the 3D effect is most pronounced. In some areas the normalized radiance for the 3D scenario differ over $\pm$20% from the fields for the 1D scenario.
In the absorption field we get differences up to +80% and –40%, but as the values for the absorption are very small in general the percentage difference might not be a good indicator in that case.
In the field of reflection the horizontal photon transport causes deviations from IPA from+30% to –20% and it is clearly linked to the gradients in optical thickness. The transmission with horizontal photon transport differs $\pm$15% from the IPA approximation.
The aspect of 1D and 3D photon transport in radiative transfer simulations for water clouds in the atmosphere is discussed in e.g. Benner and Evans (2001). Their results fit well to ours for dust clouds. Davis et al. (1997) have also shown the smoothing effect of horizontal photon transport in cloudy atmosphere. Di Giuseppe and Tompkins (2003) show that the effect of horizontal photon transport is negligible for the mean quantities of reflection, transmission and absorption, but for high variability in water cloud structure the effect increases. Also the dependence on the sun zenith angle is considered. The comparison for I3RC with 3D and 1D Monte Carlo models shows that the 3D effect is larger for lower sun zenith angle. For the step cloud with high gradient in optical thickness, the 3D effect is most pronounced (Cahalan et al. (2005)).
In case of a realistic inhomogeneous cloud it could not be seen exactly how far the hori-

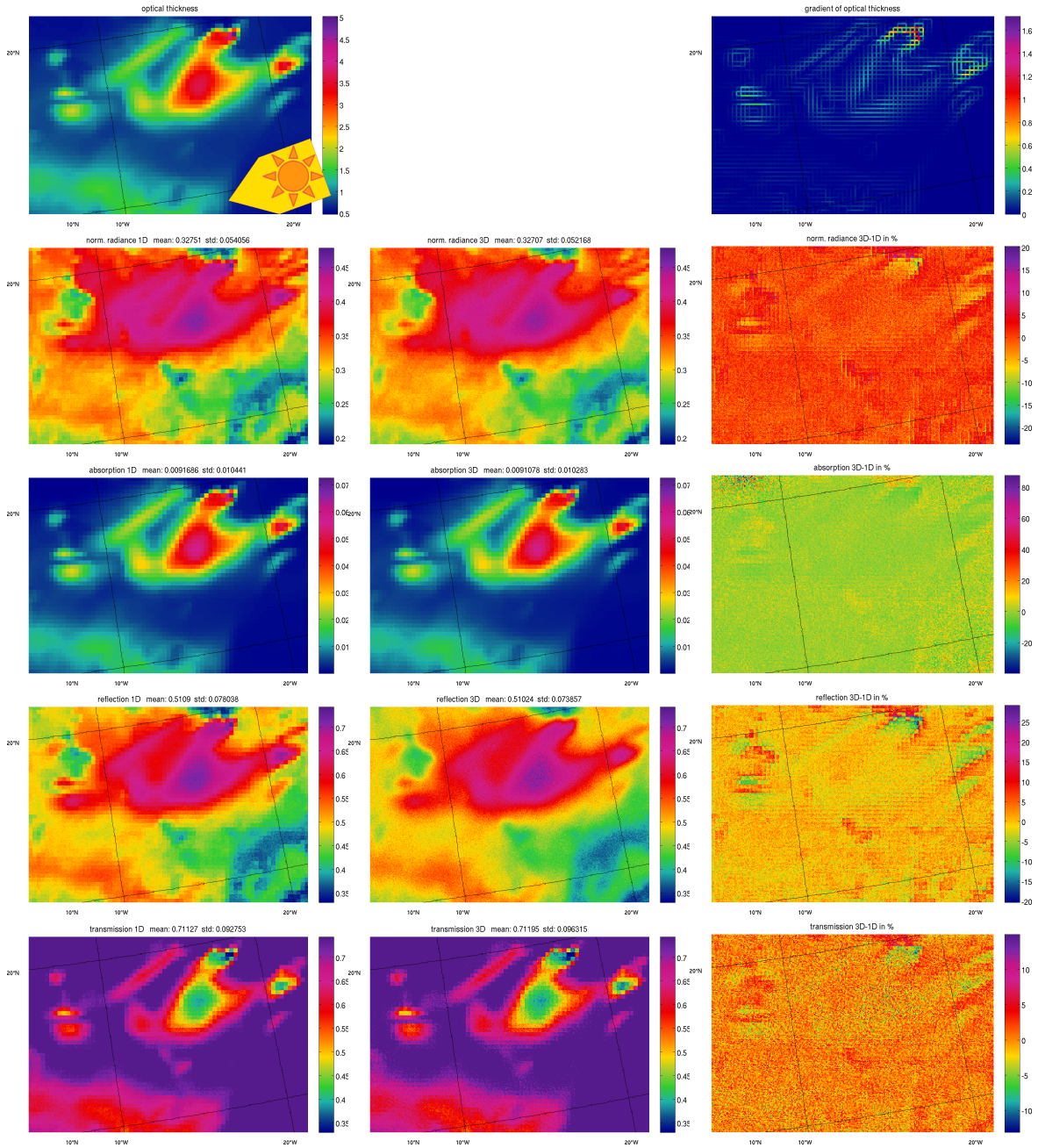

Figure 46: Overview of the MC-UniK calculations for the dust cloud from 31 January 2008: Optical thickness, normalized radiance field and fields of absorption, reflection and transmission at 33° sun zenith angle for 1D and 3D radiative transfer calculations with a resolution of 6 km.

zontal photon transport affects the radiative fields. Thus it is hard to say if it is important or negligible in certain cases. To get a better impression of how the 3D effect is influenced by cloud structure, optical thickness and sun zenith angle specific calculations with an idealized cloud structure have been performed. The results are presented in figures 47 and 48.

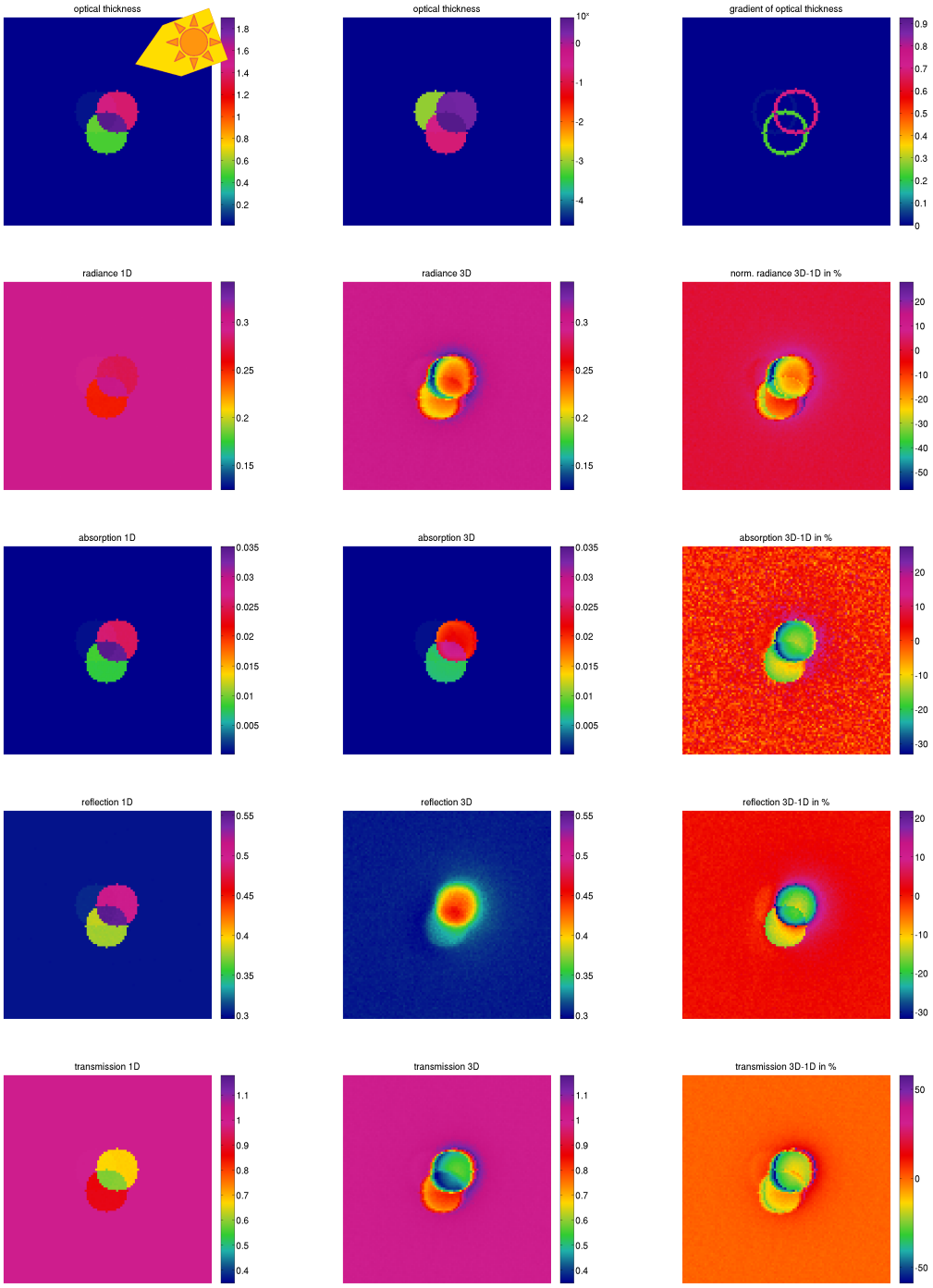

Figure 47: Results of MC-UniK calculations: Optical thickness, normalized radiance field and fields of absorption, reflection and transmission at 70° sun zenith angle for 1D and 3D radiative transfer calculations for a constructed test cloud with a resolution of 1 km.

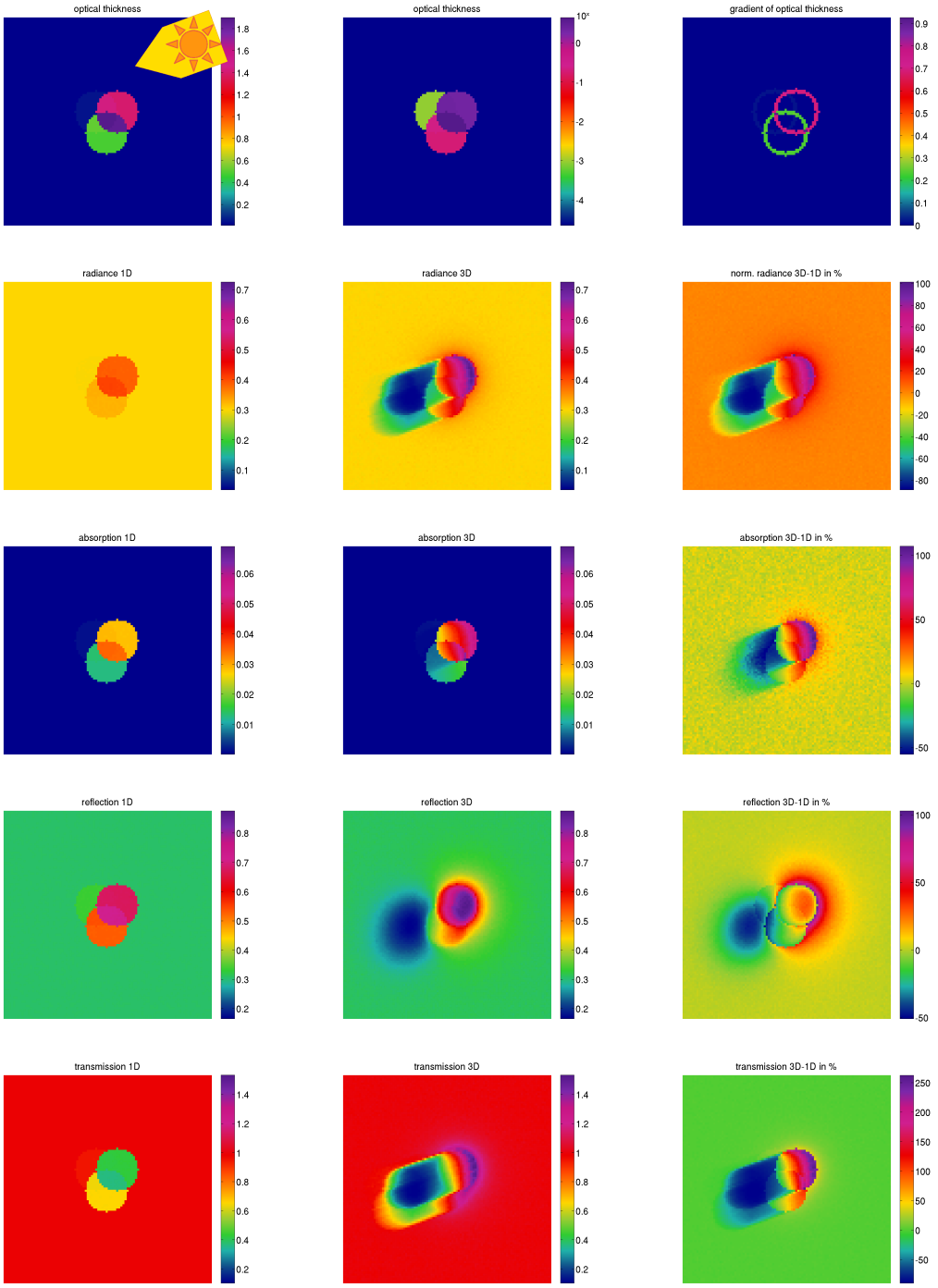

Figure 48: Results of MC-UniK calculations: Optical thickness, normalized radiance field and fields of absorption, reflection and transmission at 20° sun zenith angle for 1D and 3D radiative transfer calculations for a constructed test cloud with a resolution of 1 km.

Calculations with MC-UniK have been performed with a cloud consisting of three overlapping circles with different optical thicknesses. The resolution is 1 km per pixel. The columns of the cloud are homogeneous and they don't have a vertical varying structure, the particle size distribution is the one of the scattering class 1-2 (see chapter 5.7), which is suitable for over 60% of the dust cloud boxes of a realistic cloud.
In the first row of the figures 47 and 48 the optical thickness of the cloud is displayed in normal and in logarithmic scale. The sun direction is indicated with the yellow arrow. The third picture of the first row shows the gradient in optical thickness. Even with a sun zenith angle of 70° degree which is relatively large, the 3D effect can be seen in a region of about 5 km from the gradients in optical thickness. Deviations from the 1D calculations can be seen clearly in all radiative fields and the values differ locally by $\pm$50%. If we look at the MC-UniK calculation results for a sun zenith angle of 20° the deviations are even more obvious. About 25 km of the modelled area radiative fields away from the gradients in optical thickness are affected by horizontal photon transport. Of course in realistic dust clouds the cloud structure is more inhomogeneous and with that the affected region is influenced by different sides from different structures. But with the wide range that the 3D effect has with low sun position especially in cases with focus on local investigation one should keep in mind, that the horizontal photon transport might not be negligible.

6.4 Radiative transfer calculations for particles with different shapes

In this paragraph the topic of the deviations in radiation fields caused by different shapes is investigated. The modelled cloud from COSMO-MUSCAT from 31. January 2008 at 13:00 UTC was used to perform the Monte Carlo radiative transfer simulations with MC-UniK.
For the calculations a sun zenith angle of 33° and a satellite viewing zenith angle of 10° were assumed.
The methods of calculating the scattering properties of different shaped particles are presented in chapter 5. These were used as input for the 3D radiative transfer simulations with the model MC-UniK. Because the geometric optics method does not allow to calculate the extinction efficiency of irregular shaped particles, it was assumed that the values are identical to the ones for projected area equivalent spheres. This assumption reduces the differences in the radiative fields of irregular shaped particles compared to that of spheres. Thus, all shape induced differences in the radiation fields result from the differences in single scattering albedo and scattering phase function.
The radiative fields calculated by MC-UniK are presented in figure 49. Because of the limited calculation resources, the calculations are not performed on the whole model area, but on a dust hot spot, an area which covers the Bodélé depression. Nearly in the middle of the pictures Lake Chad can be seen.
The first row shows the optical thickness of the dust cloud consisting of spherical, spheroidal and irregular shaped particles, but no significant shape-induced differences can be seen. The same is true for the absorption, reflection and transmission field.
Most obvious are the shape induced differences in the normalized radiance (second row). The pixel with high optical thickness show big differences in the radiance field especially in regions with high optical thickness.

The domain averaged deviations from the reference cloud with spherical particles are shown in figure 50. Large differences occur in the absorption field. For spheroids the averaged absorption field is about 3.6% higher and for irregular shaped particles it is 17.1% higher than the absorption field of spherical particles. However the absolute values are very small, so that percentage differences might not be the best indicator for shape-induced absorption differences.
The averages of fields of reflection and transmission differ by less than 1% for irregular particles and spheroids from spheres. In Yang et al. (2007) is shown that the reflectance of a dust cloud with spheroidal particles is much higher than the reflectance of a cloud consisting of spherical particles, which under the chosen conditions (aspect ratio, refractive index) of this study could not be verified.
For the averaged field of normalized radiance we find lower values for spheroids and irregular particles. The normalized radiance of the dust cloud consisting of spheroids is about 20.3% lower than that with spherical dust particles. In the case of the irregular shaped particle the averaged field is 13.7% lower.
In Fu et al. (2009) differences of less than 5% at a wavelength of 0.55μm have been found for their dust cloud reflectivity calculations. Here also the differences in the extinction efficiencies and single scattering albedo for spherical and spheroidal particles are less than

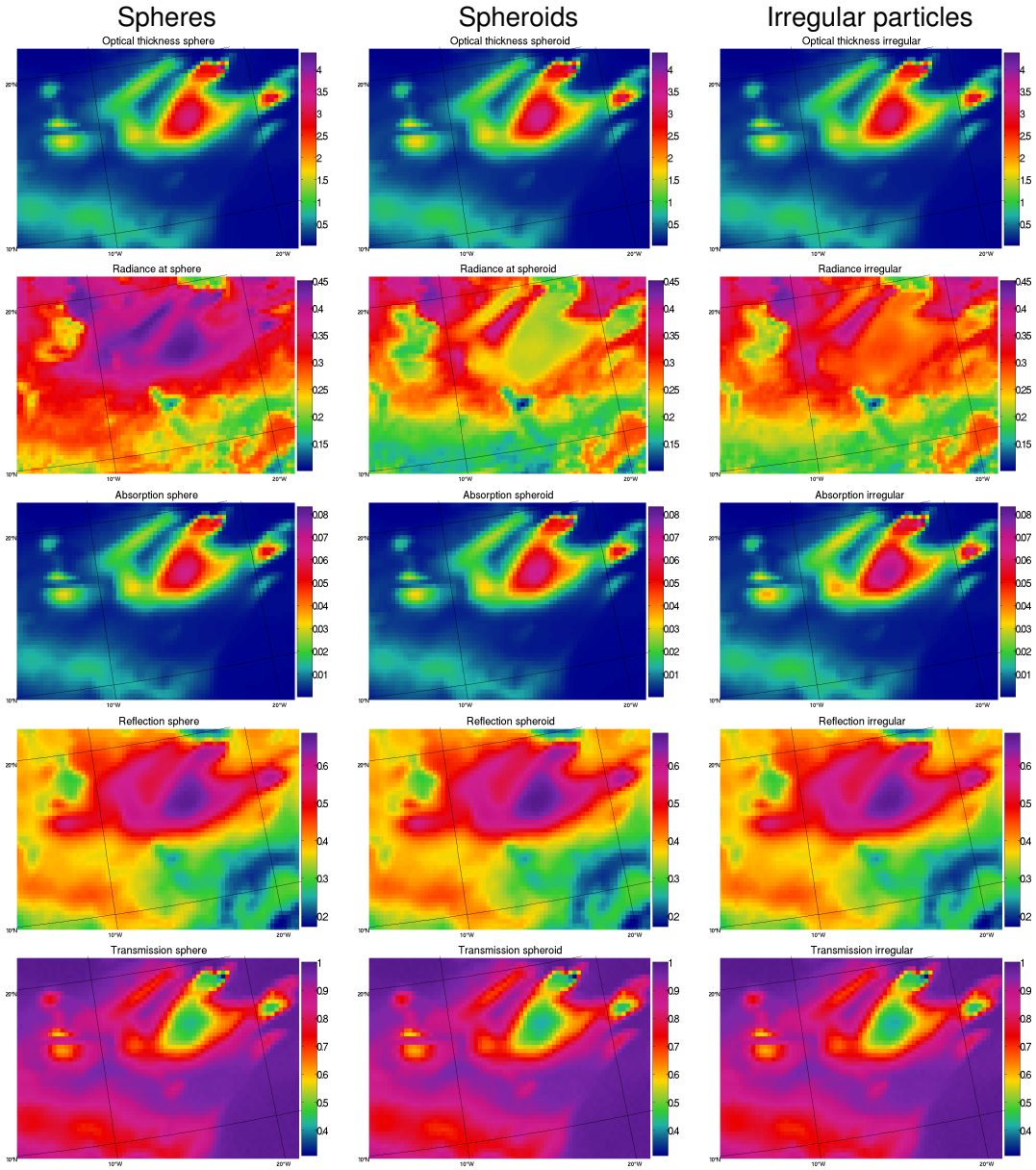

Figure 49: Radiative fields calculated with MC-UniK at 0.6μm for three different shapes (spheres, spheroidal and irregular particles)

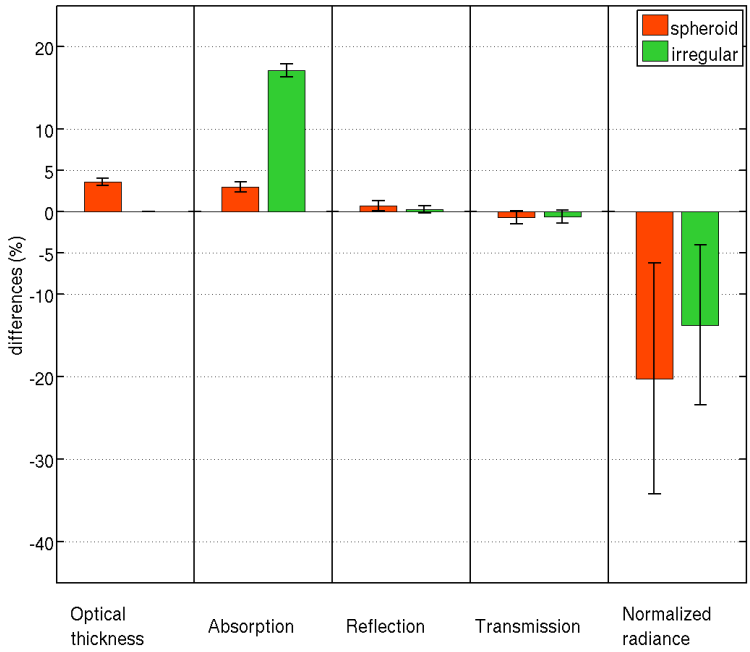

Figure 50: Differences of normalized radiance from sphere to spheroid and sphere to irregular particle for the radiative fields

1%.
The very high difference found in this study seem unexpected and hard to explain.

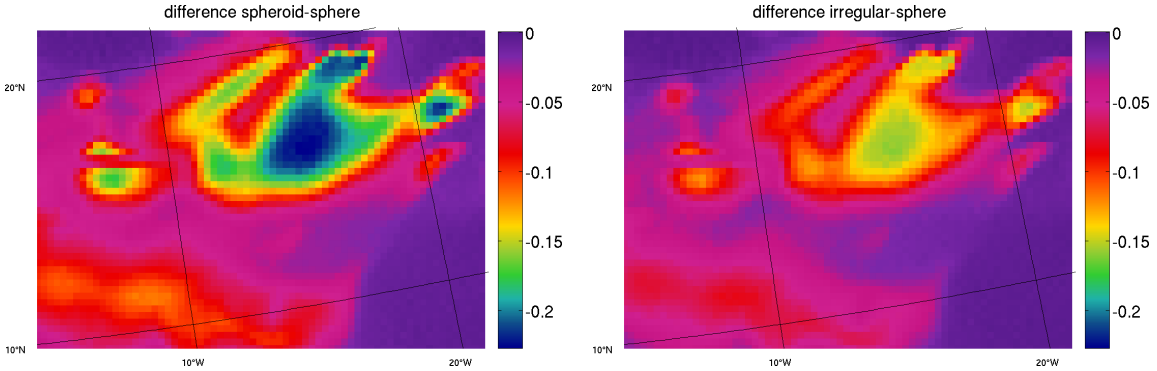

Figure 51: Differences of normalized radiance from sphere to spheroid (left side) and sphere to irregular particle (right side)

If we look at the local distribution of the differences of the radiation fields shown in figure 51, it is even more obvious that the differences are highest in pixels with high optical thickness. Here the deviation of the normalized radiance fields from the field of spherical particles to the field of spheroidal particles on the left side and the differences in percent of the field with spherical particles to the field of spheres is plotted. In the thicker parts of the dust cloud the radiance is over 20% lower in a cloud with spheroidal particle than in the cloud with spherical particles. For irregular shaped particles the radiance is up to 13% lower.

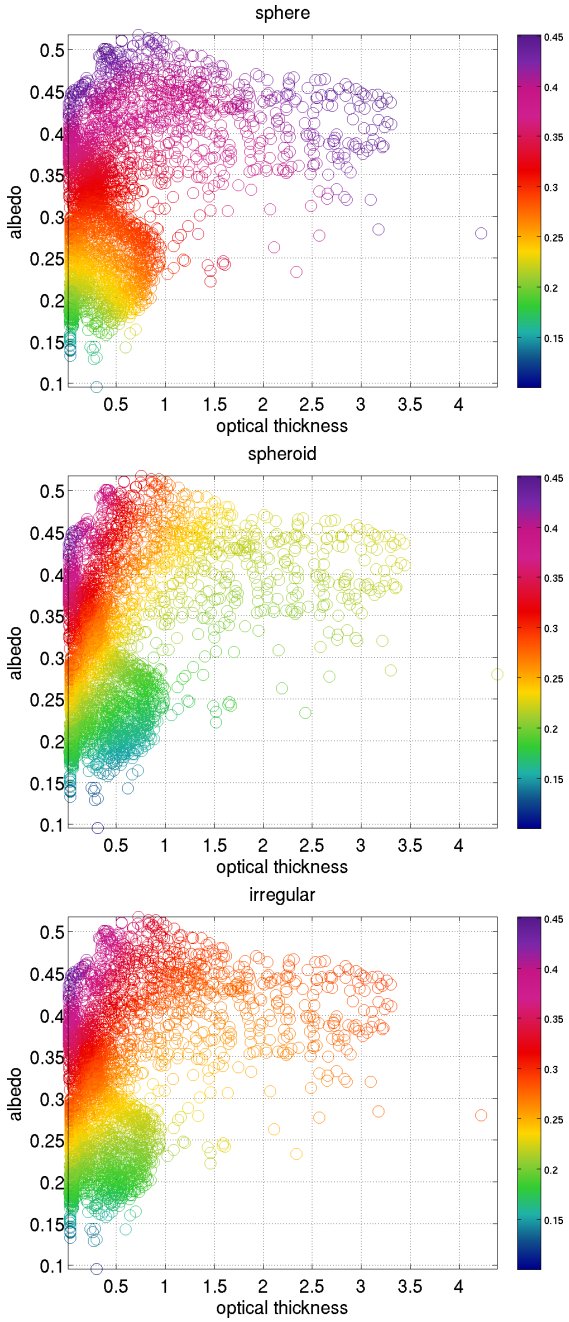

Figure 52: Normalized radiance dependent on the optical thickness and the surface albedo of a cloud with spherical (left), spheroidal (middle) and irregular shaped particles

Figure 52 shows the normalized radiance in colour of a cloud with spherical (top), spheroidal (middle) and irregular shaped (bottom) particles dependent on the optical thickness on the x axis and on the surface albedo on the y axis. What particularly catches the eye is that with

higher optical thickness the radiance is not steadily increasing.
One reason for that is, that the majority of the cloud pixels with high optical thicknesses has a relatively high surface albedo below, leading to a reduced surface reflection at larger dust optical thickness. This is explained in more detail in chapter 4.2 This results in high optical thickness and also more big particles exactly over surfaces with large albedo values. The particle size plays an important role in the differences of the radiative fields. The deviations in optical particle properties are increasing with particle size, thus one would expect bigger differences in the simulated radiative field where larger particles are involved.

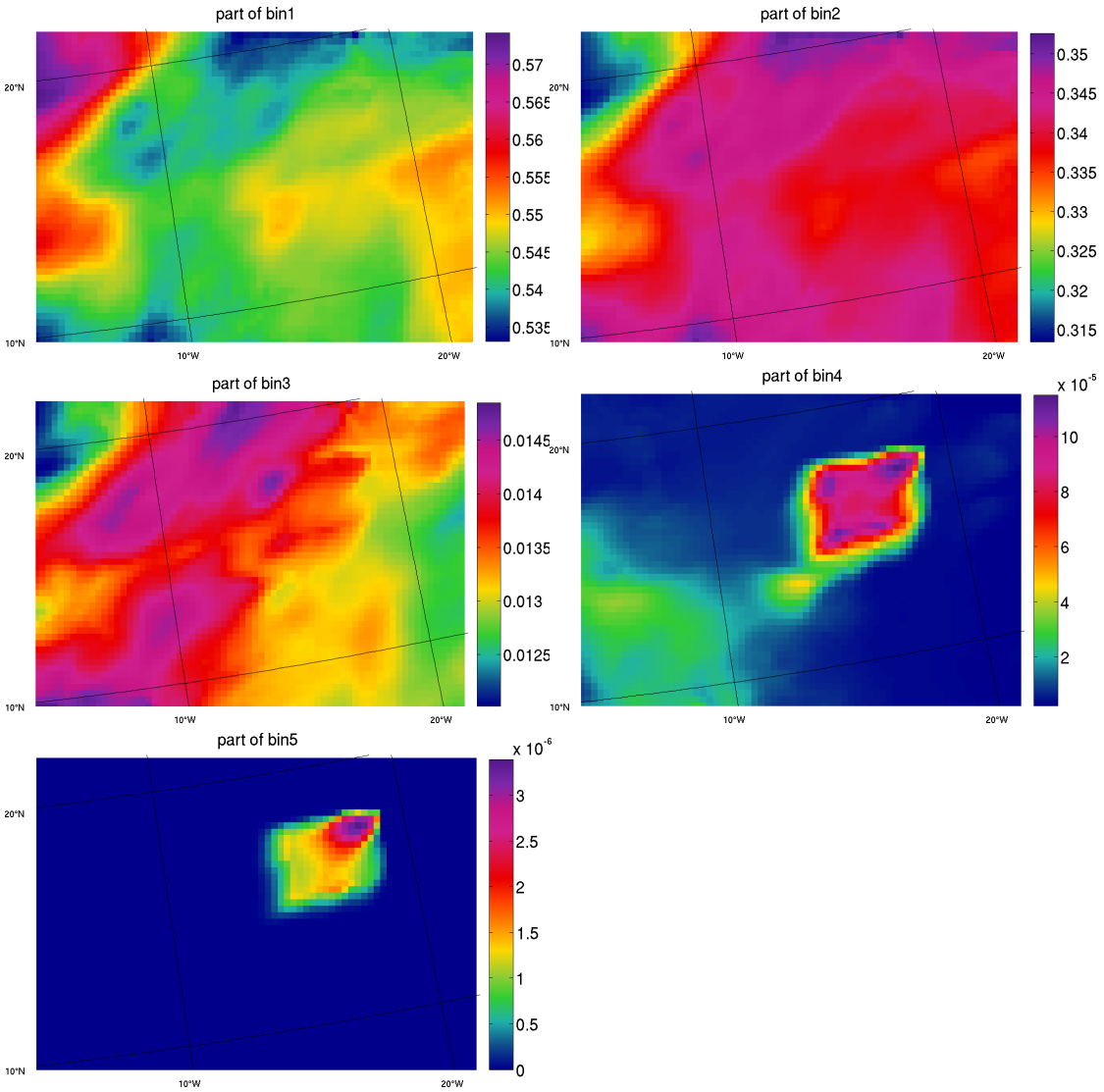

Figure 53: Local distribution of the proportion of the 5 size classes of the dust cloud particles. bin1: 0.166 µm, bin2: 0.501 µm, bin3: 1.514 µm, bin4: 4.571 µm, bin5: 13.804 µm particle radius

In figure 53 the vertical averaged distribution of the 5 particle size classes are plotted. The pictures indicate that the hot spot of large particles (bin4 with 4.571 μm and bin5 with 13.804 μm particle radius) is in the regions with the higest optical thickness close to the dust source.
From the comparison of the scattering properties of single particles of different shapes in 5.5 we have seen, that the differences of optical properties of dust particles increase with particle radius. The bigger portion of large particles may cause the big differences in the normalized radiance in regions with high optical thickness. The connection between vertical averaged effective radius of the dust cloud pixel and the optical thickness of that pixel is shown in figure 54

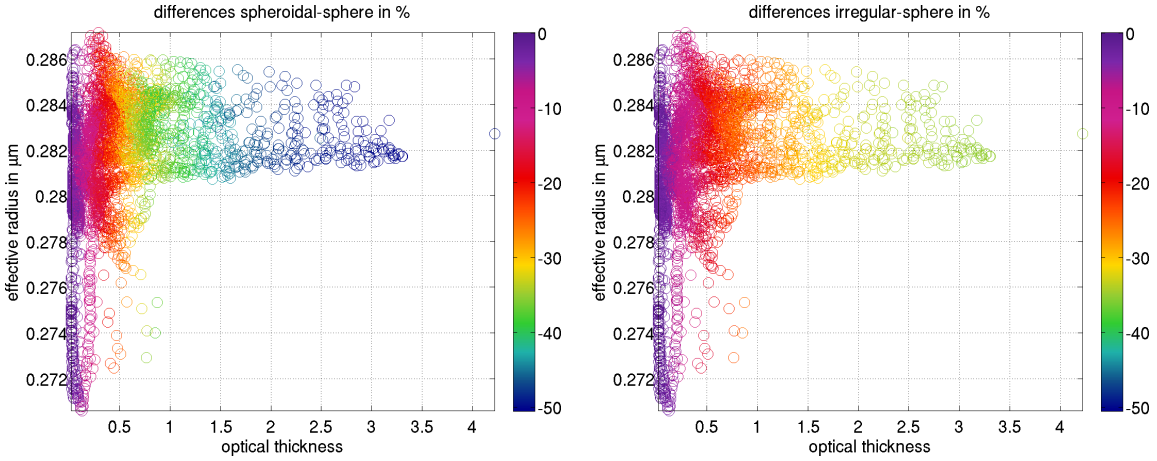

Figure 54: Differences of normalized radiance of a cloud consisting of spheroidal (left) and irregular shaped particles (right) to a cloud consisting of spherical particles

Nearly all pixels with high optical thickness $\tau > 1$ also have high effective radii $r_{eff} > 2.8$ μm. The pictures illustrate, that the biggest deviations of normalized radiance fields of clouds with spherical particles compared to spheroidal or irregular shaped particles are located in the pixels with high optical thickness and high effective radii. Especially for spheroidal particles this effect is most pronounced.
The combination of a very big amount of large particles results in big shape induced differences in radiative fields.
Also the vertical dust distribution could give a hint on cloud structure of the pixels where the biggest differences are located. Figure 55 shows the vertical resolved composition of the cloud pixels. On the x axis the percentages of the 5 size bins are given. The colours indicate the averages of pixels with high (violet) and low (green) differences in the normalized radiance exemplary between the cloud consisting of spherical and spheroidal particles.
In the cases with highest shape induced differences especially in the first meters above the surface, the proportion of large particles from the size classes bin3 (1.514 μm), bin4 (4.571 μm) and bin5 (13.804 μm) is the biggest.

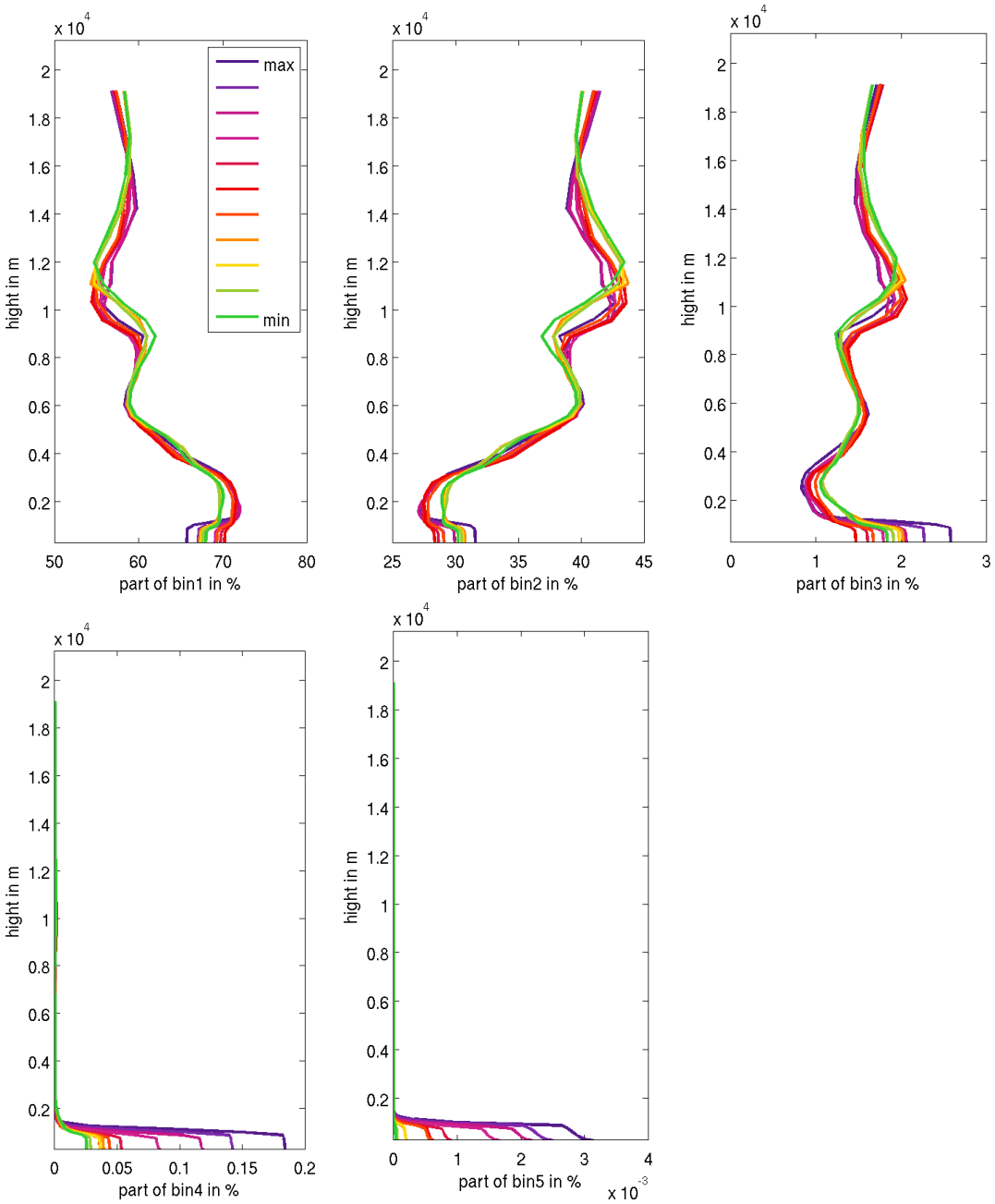

Figure 55: Vertical distribution of the portion of the 5 size classes of the dust particles. The colours are a measure for the differences of the simulated radiance from green for small differences to violet for high differences.

In the cases of the cloud from 31. January 2008 at 13:00 UTC we have a combination of high optical thickness above high surface albedo and a bigger proportion of larger particles

especially above the surface in this cloud pixels. To see, how the radiative transport calculations result in other conditions than in this very special case, one should have a look at other modelled dust clouds from COSMO-MUSCAT. But here the problem is, that in all realistic modelled clouds we have nearly the same conditions. The dust sources have a higher surface albedo and next to the dust sources we get high optical thickness and the proportion of larger particles is bigger.
To understand better how the conditions influence the radiative transfer calculations test clouds were built. Because the particle size seem to be an important factor to explain the big differences in radiative fields of dust clouds of different shaped particles, the test clouds consist of only one particle size. As we have 5 particle sizes (bin1: 0.166 μm, bin2: 0.501 μm, bin3: 1.514 μm, bin4: 4.571 μm and bin5: 13.804 μm), we get 5 clouds with substantial different micro-physical properties. The test clouds are vertical homogeneous. Within the test cloud the optical thickness is varying between 0 and 3. The underlying surface albedo has a range from 0.1 to 0.6, which covers all values occurring in the Sahara.
The test clouds have pixels with combinations of the values with different optical thicknesses and different surface albedos. And as the different particles sizes are treated separately the results can be linked to particle size, optical thickness and surface albedo.

Figure 56 displays the normalized radiance fields for the test clouds. The columns are sorted by the particle shape, spherical, spheroidal and irregular shaped particles and the rows show the different particle size bins from bin1 to bin5. The figures for the other radiative fields (absorption, reflection and transmission) are displayed in the appendix in chapter 8 in figures 60 to 62. In the regions with high optical thickness the normalized radiance is decreasing. The absorption is increasing with optical thickness, the transmission is decreasing. These effects are most pronounced for large particles. The reflection is lower in case of high optical thickness and large particles.
In figure 56 in the last row the normalized radiance with logarithmic scale for large particles of bin5 with an effective radius of 13.804μm for spherical, spheroidal and irregular shaped particles is displayed. There the shape induced differences are most obvious. With higher optical thickness the radiance is decreasing. This is more pronounced for irregular shaped particles than for spheres, but for spheroidal particles this effect is much stronger. As the effect is stronger for high optical thickness and large particles this is a good explanation for the large shape induced differences we get for the real COSMO-MUSCAT cloud from the 31. January 2008 at 13:00 UTC.

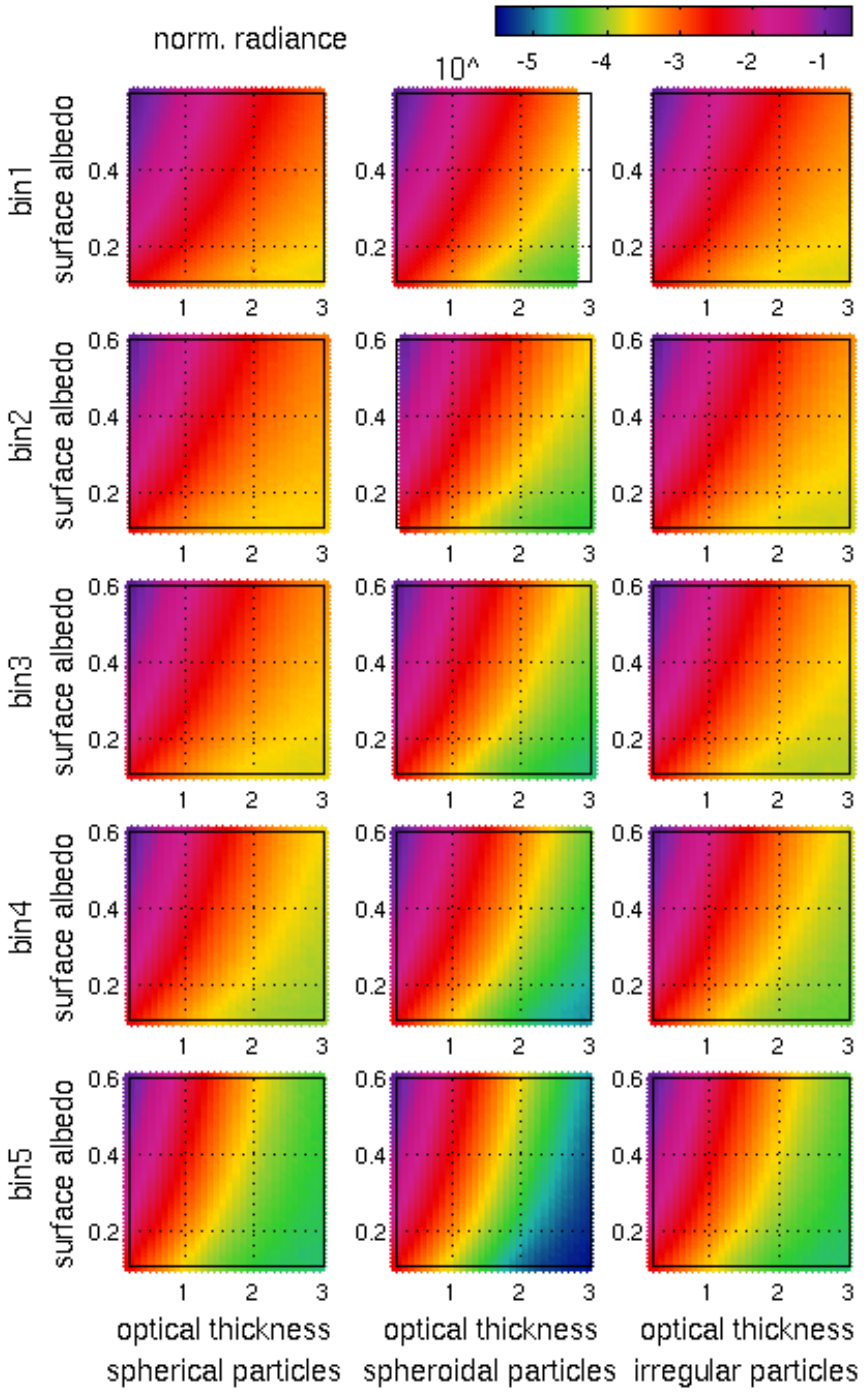

Figure 56: normalized radiance of the test cloud consisting of spherical, spheroidal and irregular shaped particles depending on the surface albedo and optical thickness, sorted by particle size.

7 Outlook

The Monte Carlo Model MC-UniK has offered the opportunity to simulate the radiative transfer in highly inhomogeneous realistic shaped dust clouds. Although it needed a lot of computing time, it was possible to simulate radiative felds in different szenarios.
In this work was shown that the assumption of special shapes of dust particles in radiative transfer calculations causes big deviations in the resulting radiative fields. It could not be worked out which of the tested shapes (spheres, spheroids and irregular particles) is the best approach. The problem is to compare modelled radiative fields with measurements, because of different resolutions of the spacial distribution and in the wavelength. With the model MC-UniK used in this study it is only possible to model the radiative transfer at one certain wavelength, but the satellite measurements from the MSG satellite are made at a band around the center wavelength. Thus it was not possible to compare the absolute values, only patterns of radiance could be recognized. The computational effort would have been to high to model the radiative transfer on more than the chosen wavelengths. But that is an interesting posibility to improve the results of this study in future.
A lot of asumptions had to be made to perform the radiative transfer calculations. As they are made even for the input data the errors are forwarded and perhaps increased to the end results. So a lot of work has to be done with sensitivity studies to get to know to which assumtions and deviations the results are sensible.
In this thesis could be shown, that the usage of different shapes, which only rudimental could represent the big variety of natural dust shapes, result in significant different radiative fields. But it also is possible, that a lot of the other assumptions can influence the radiative fields. The refractive index should be a focus of sensitivity studies as well. Even small changes can cause big deviations in the absorption properties of one particle. Also the size dependency of th refractive index should be one focus. In this thesis was assumed that it is the same for all particle sizes.
The particle size is also a big point in radiative transfer simulations and the influence of changes in the size distribution is not very clear. But one can say that the larger the particles are, the more important are even small changes in the optical properties.
The importance of the correct surface albedo should not be underestimated. In chapter 4.2, esspecially in figure 27 is shown that the modelled radiance is increasing with the underlying surface albedo. This is even more important on thin dust clouds.
Another important topic is the horizontal photon transport. It is often neglected in common radiative transfer models due to computation time. But the 3D effect can lead to big deviations in the radiative fields. The deviations are increasing with lower sun position and with high gradients in the optical thickness of the dust cloud. In the mean of the radiative fields the 3D effect has no signifocant influence, but local effects can cause differences in the fields of more than 80% in ideally shaped test clouds. It should be investigated with several realistic shaped clouds and different sun positions how much the results differ in reality and how big the affected area around the cloud optical thickness gradients is.
Further the moving dust cloud is changing its composition with time. There the size distribution is affected. But also other aerosols can mix with the dust and change the optical

properties of the dust cloud. This effect also was neglected in this study and should be investigated in the future.

8 Appendix

MSG IR Index vs. modelled cloud from COSMO-MUSCAT at different timepoints (yyyymmddtttt)

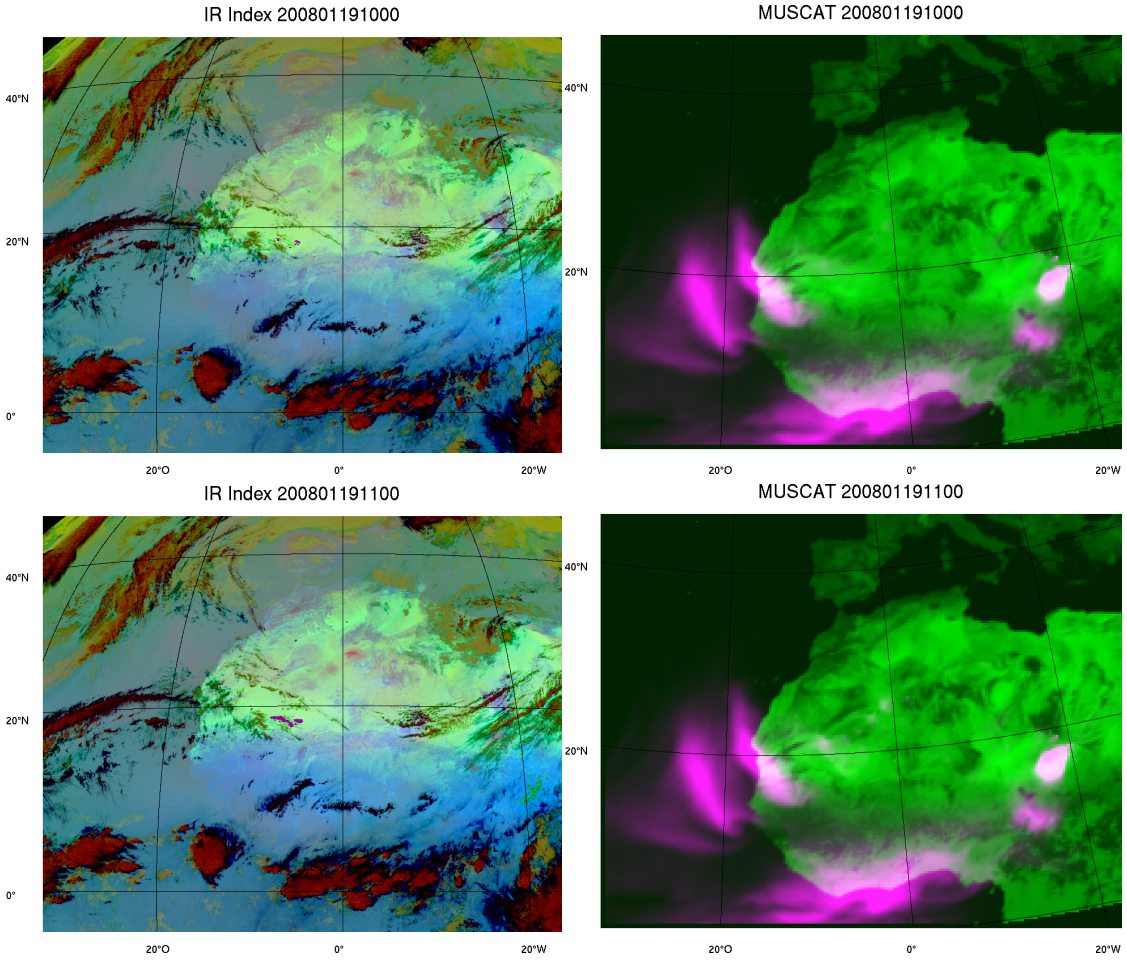

IR Index 200801191200

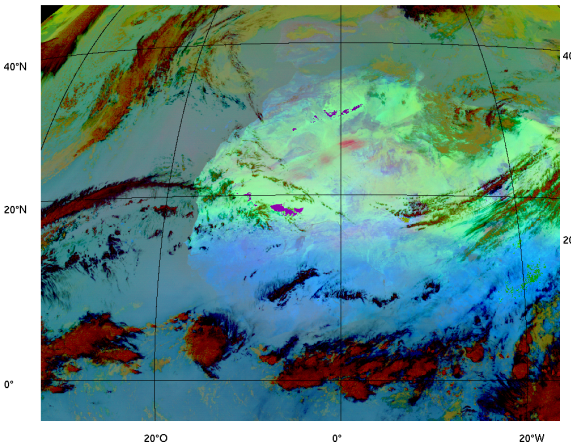

MUSCAT 200801191200

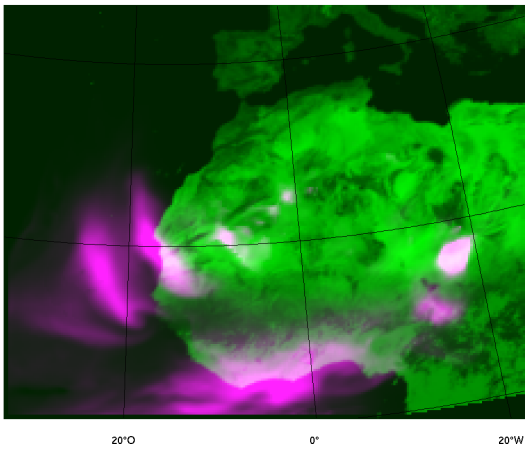

IR Index 200801191300

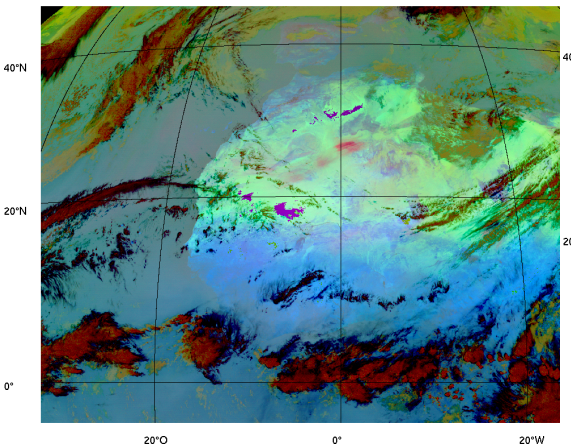

MUSCAT 200801191300

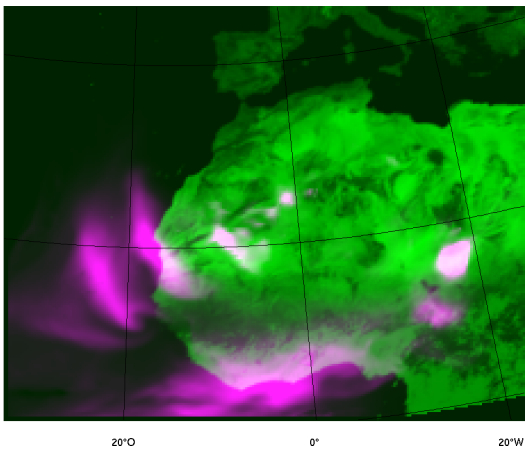

IR Index 200801191400

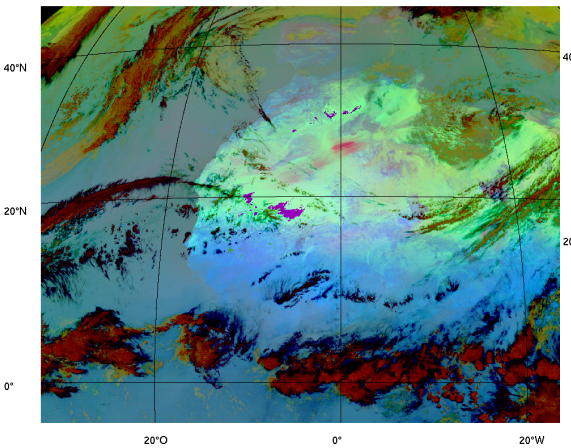

MUSCAT 200801191400

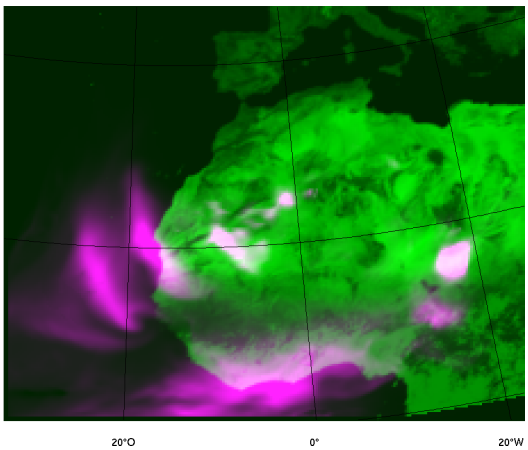

IR Index 200801191500

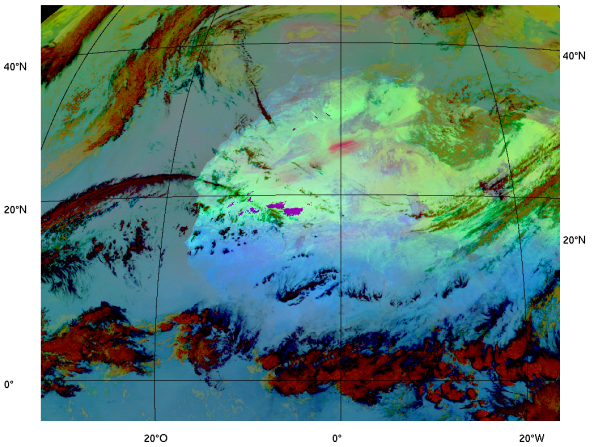

MUSCAT 200801191500

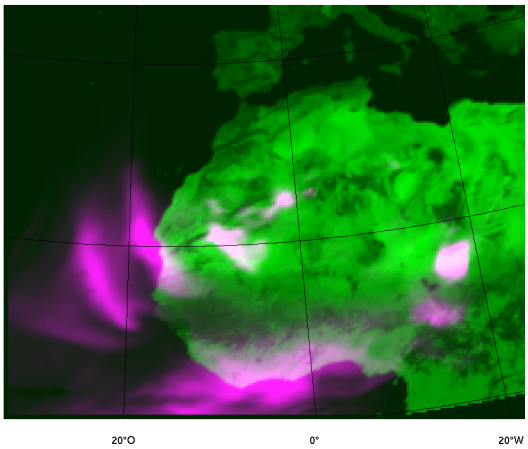

IR Index 200801250100

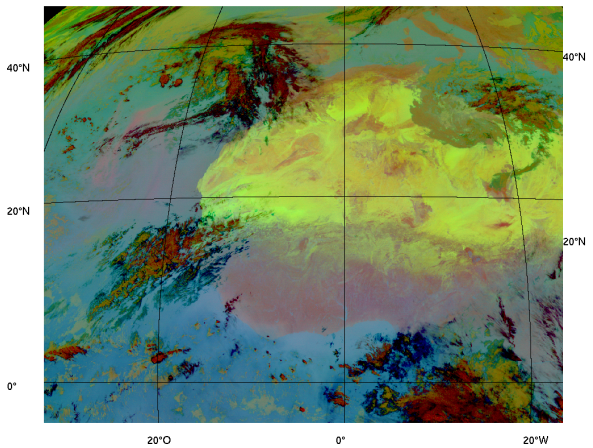

MUSCAT 200801250100

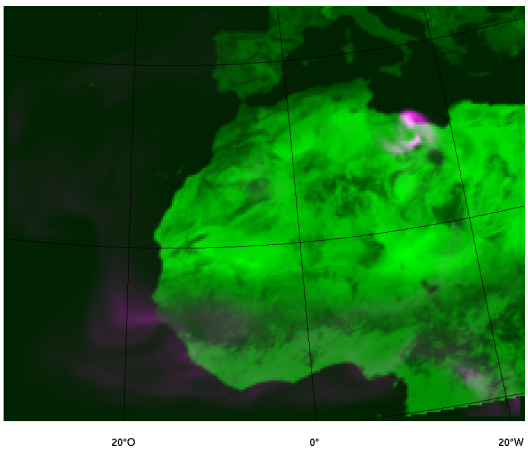

IR Index 200801250200

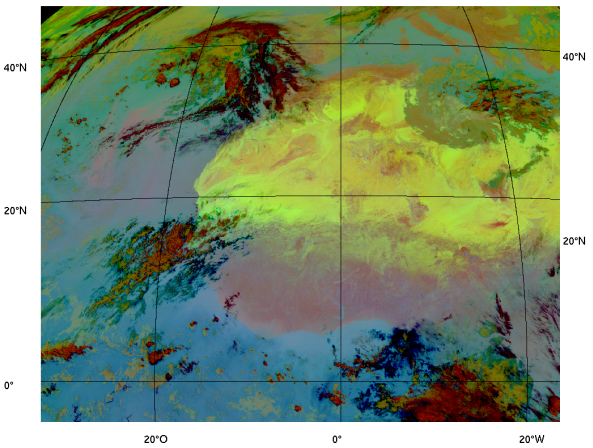

MUSCAT 200801250200

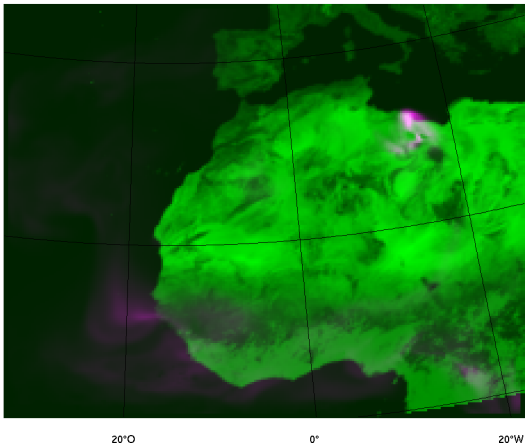

IR Index 200801250300

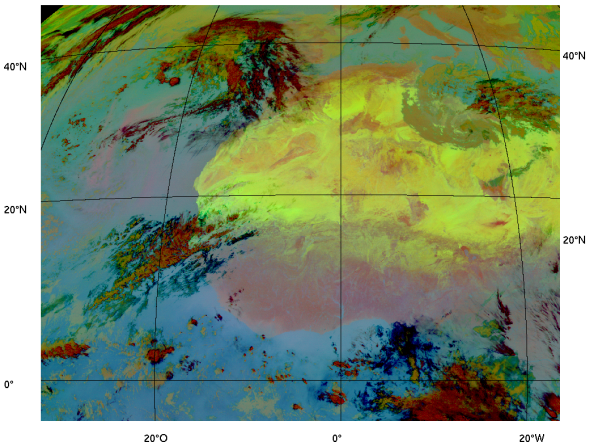

MUSCAT 200801250300

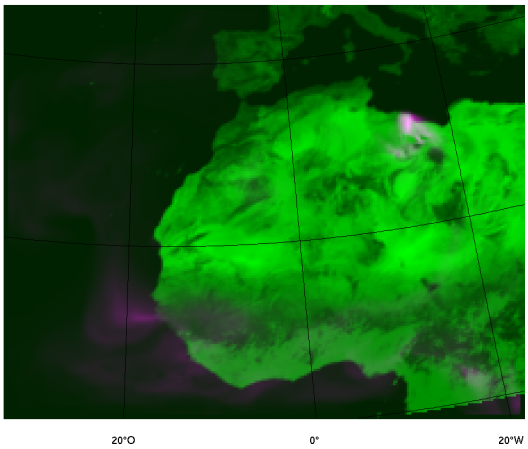

IR Index 200801250400

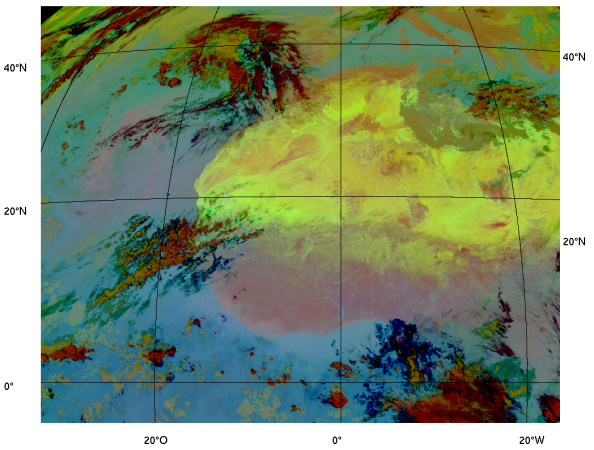

MUSCAT 200801250400

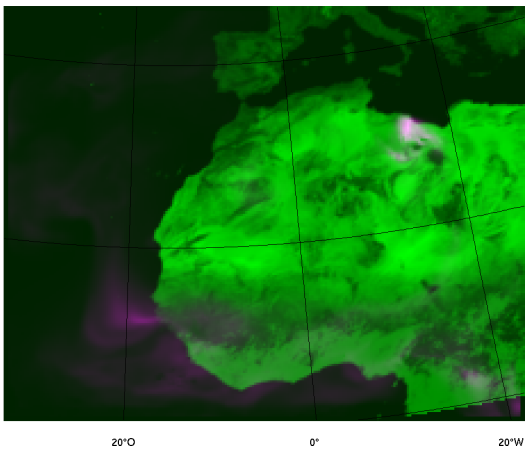

IR Index 200801250500

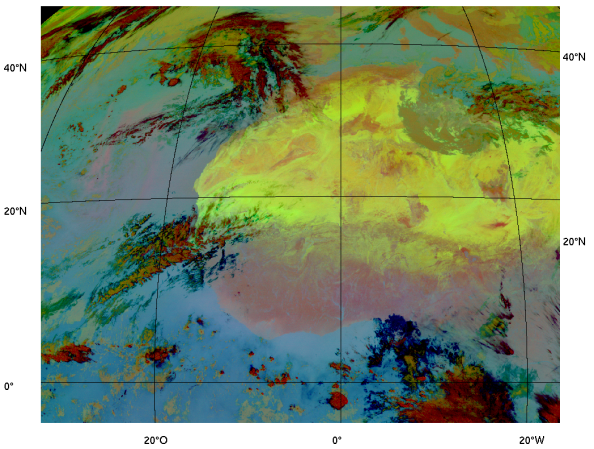

MUSCAT 200801250500

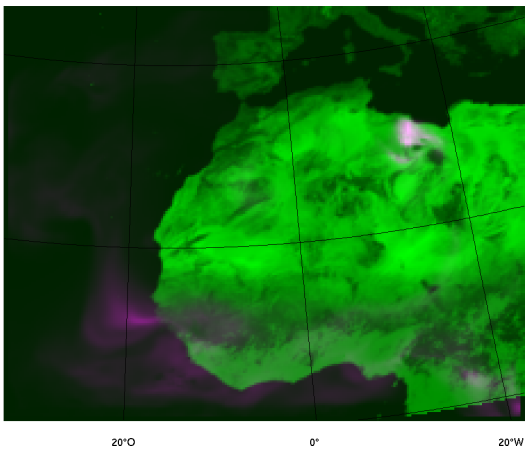

IR Index 200801250600

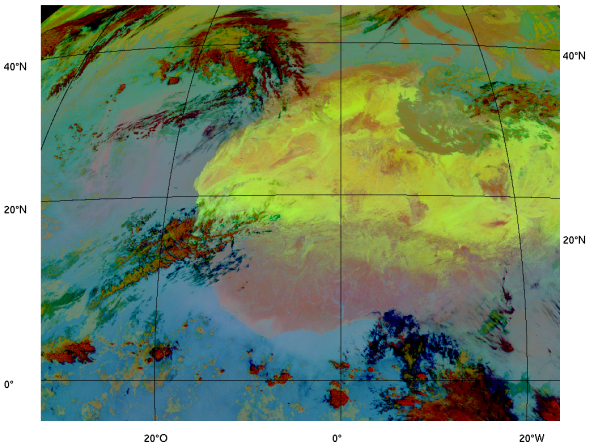

MUSCAT 200801250600

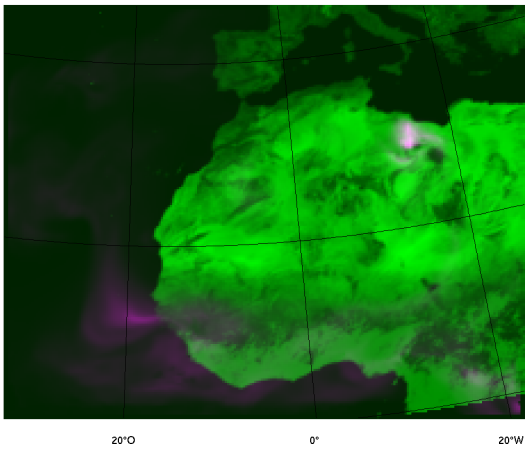

IR Index 200801250700

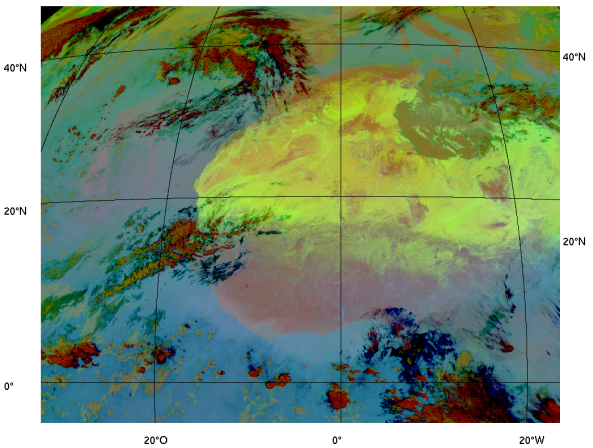

MUSCAT 200801250700

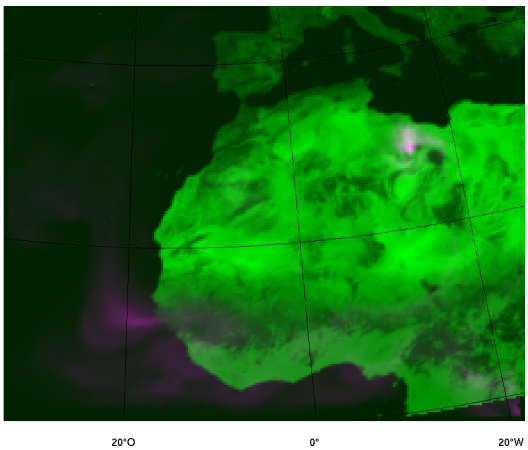

IR Index 200801250800

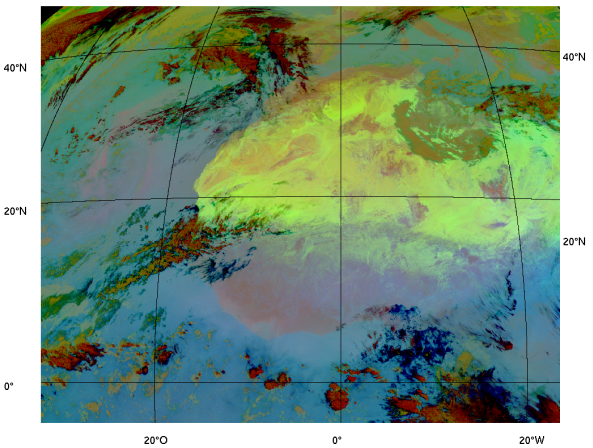

MUSCAT 200801250800

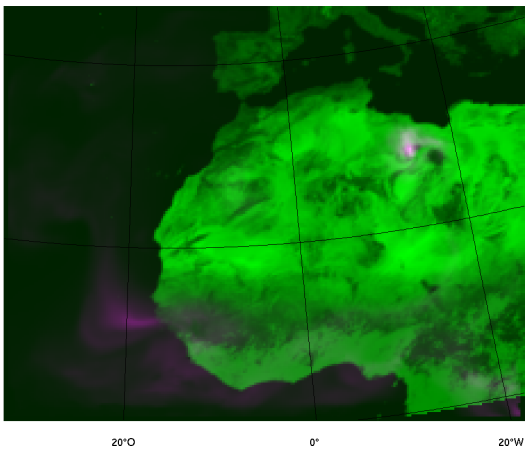

IR Index 200801250900

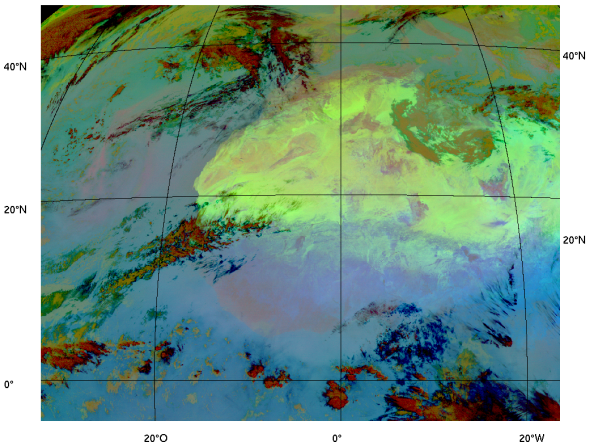

MUSCAT 200801250900

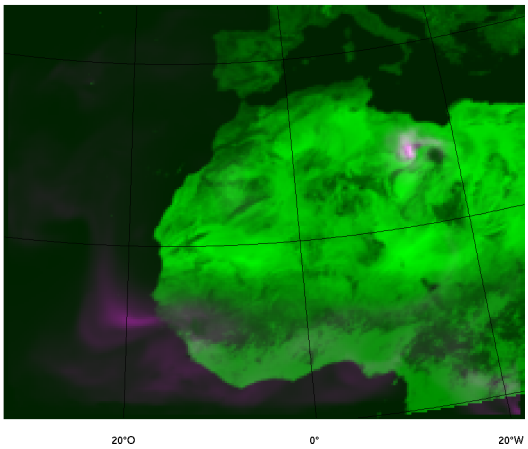

IR Index 200801251000

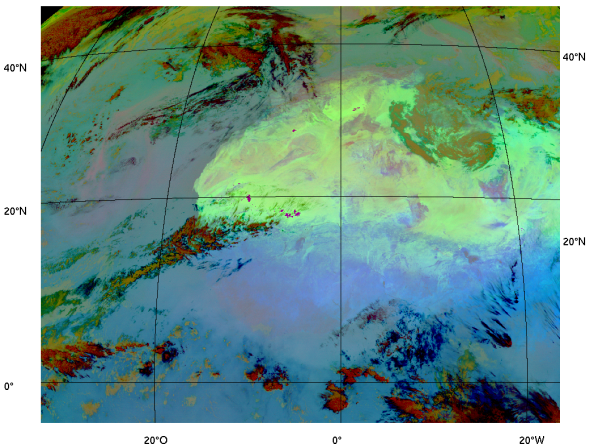

MUSCAT 200801251000

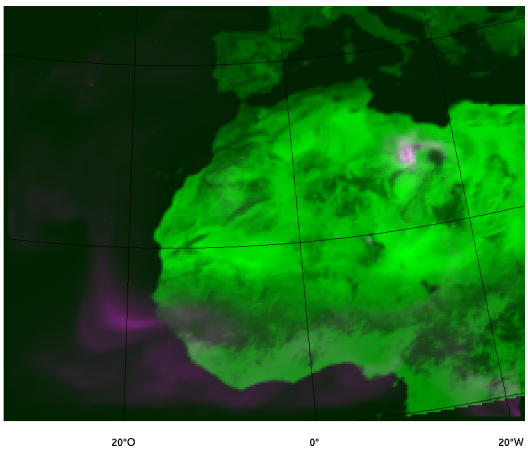

IR Index 200801251100

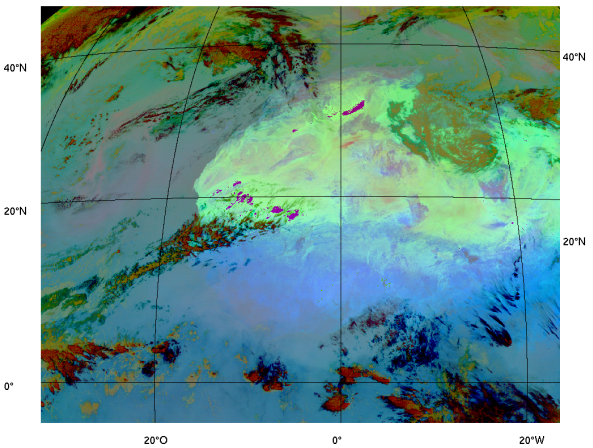

MUSCAT 200801251100

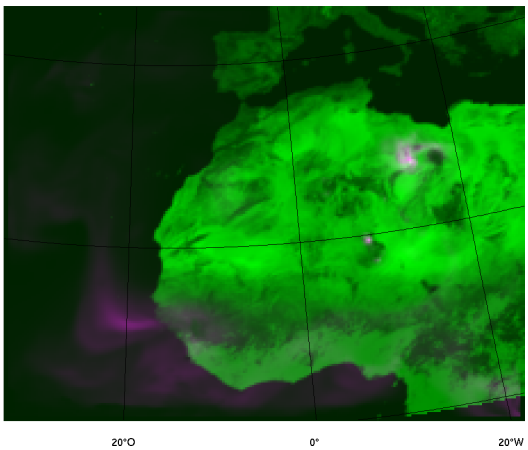

IR Index 200801251200

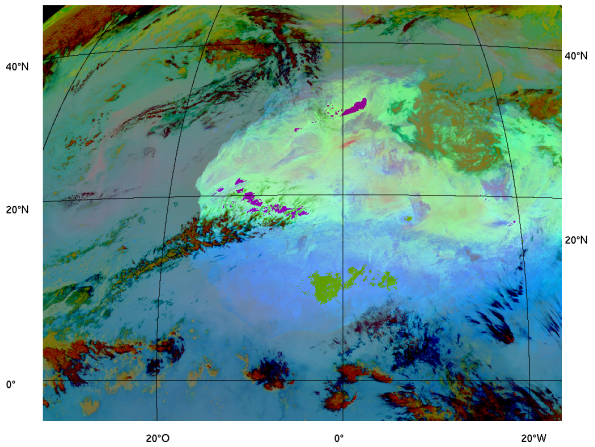

MUSCAT 200801251200

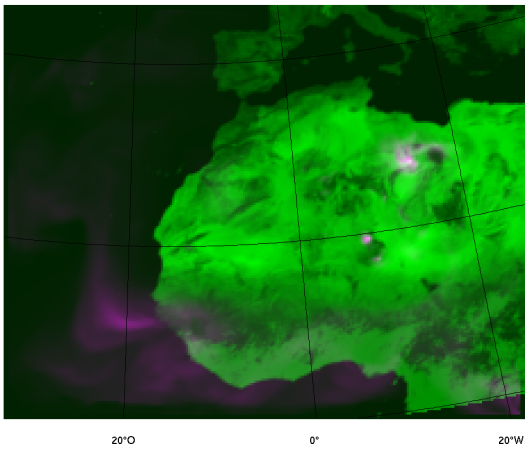

IR Index 200801251300

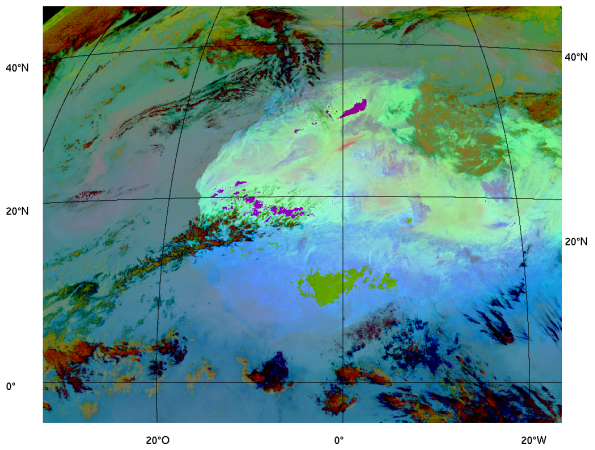

MUSCAT 200801251300

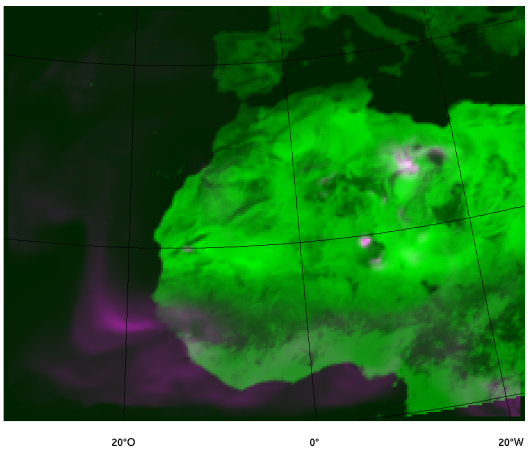

IR Index 200801251400

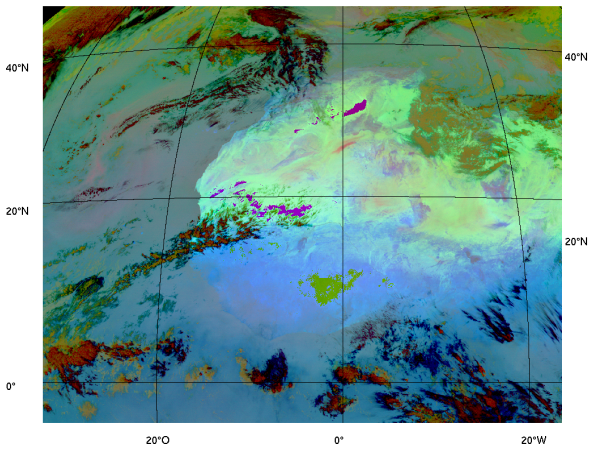

MUSCAT 200801251400

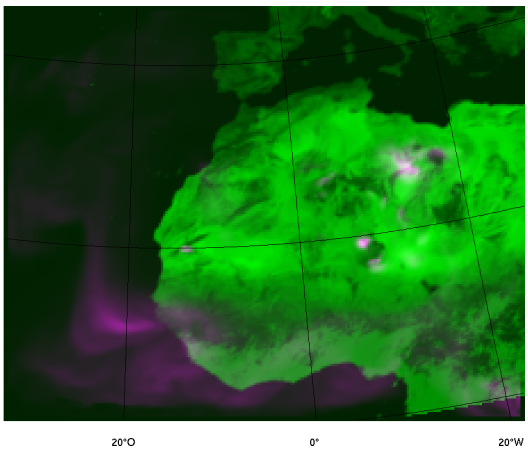

IR Index 200801251500

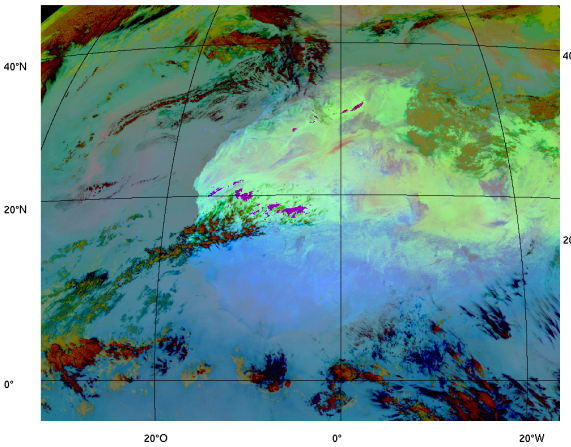

MUSCAT 200801251500

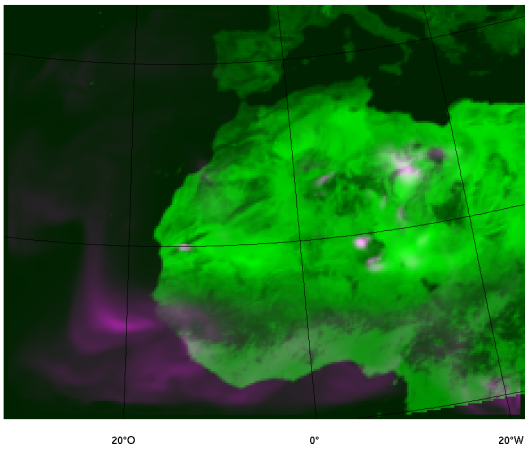

IR Index 200801251600

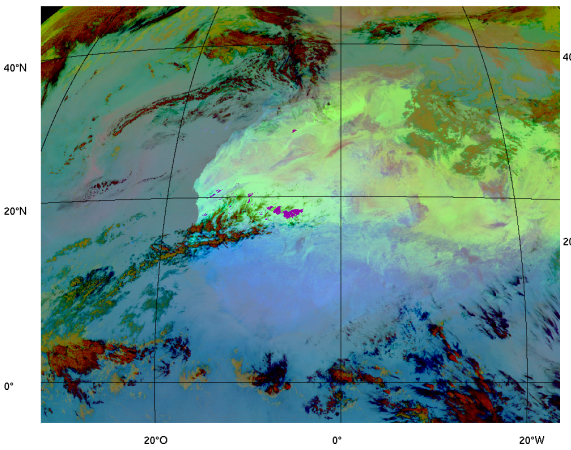

MUSCAT 200801251600

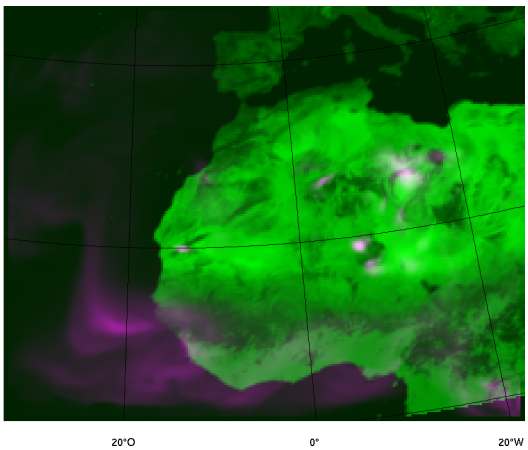

IR Index 200801251700

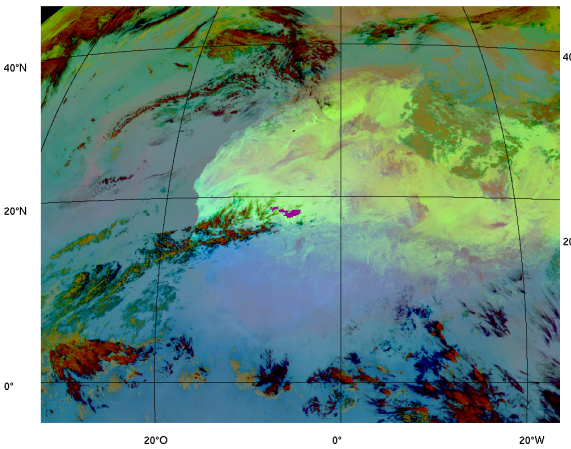

MUSCAT 200801251700

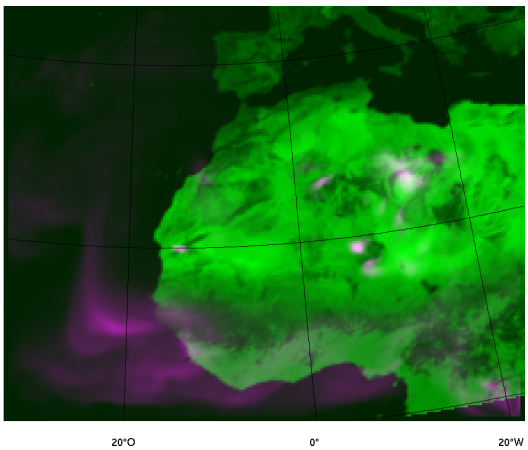

IR Index 200801251800

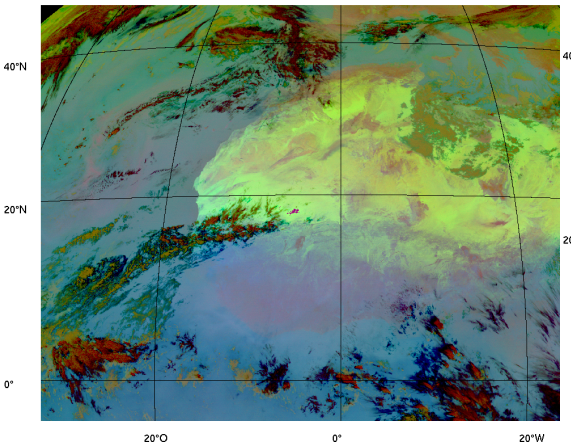

MUSCAT 200801251800

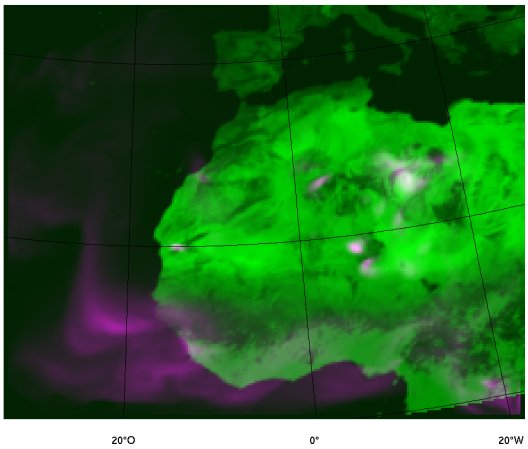

IR Index 200801251900

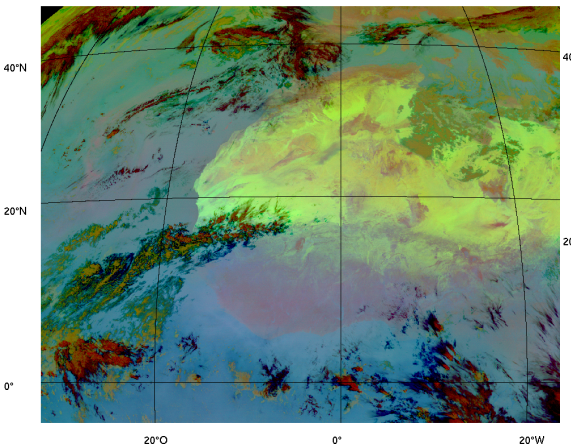

MUSCAT 200801251900

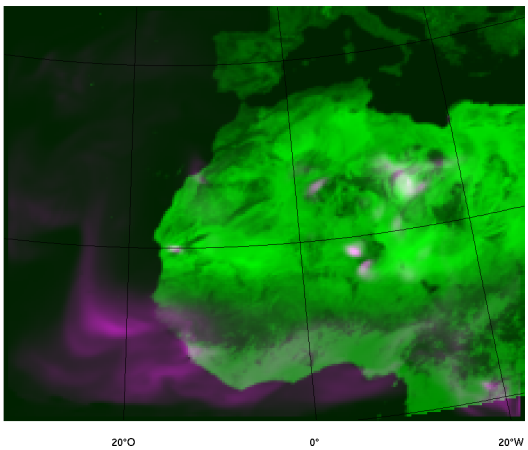

IR Index 200801252000

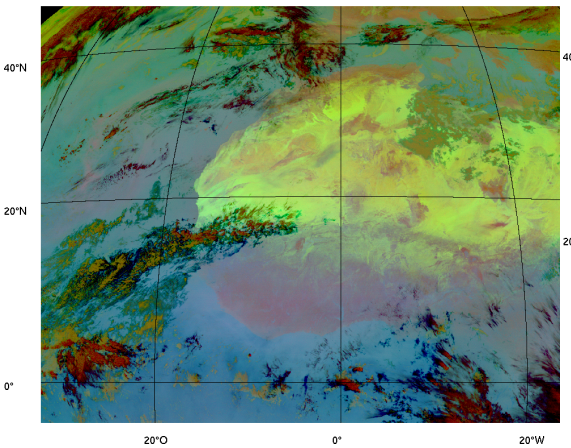

MUSCAT 200801252000

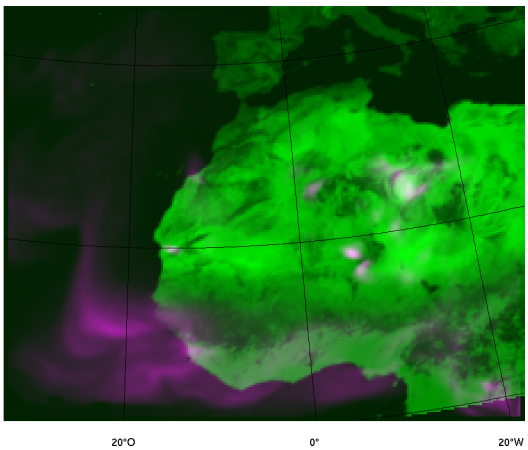

IR Index 200801252100

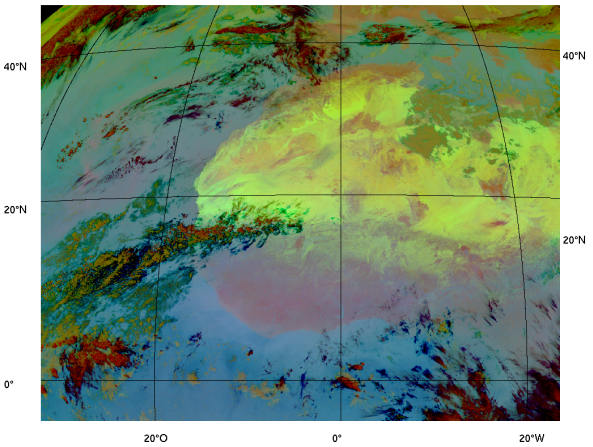

MUSCAT 200801252100

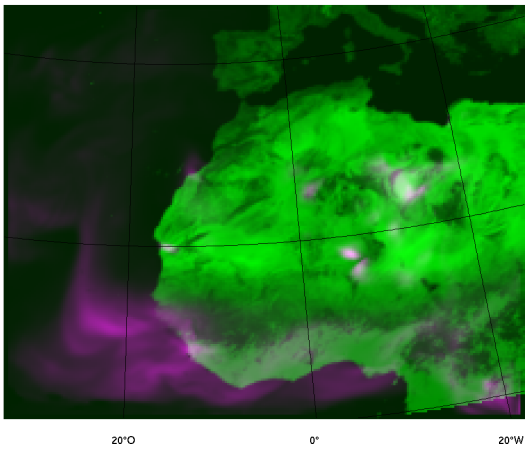

IR Index 200801252200

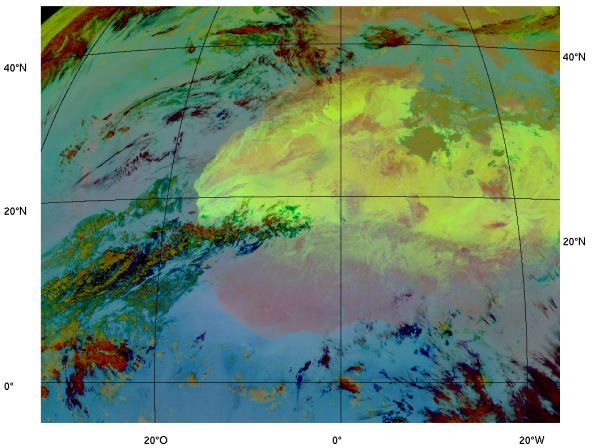

MUSCAT 200801252200

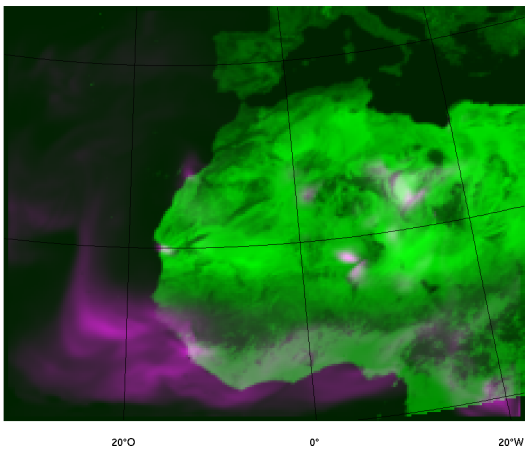

IR Index 200801252300

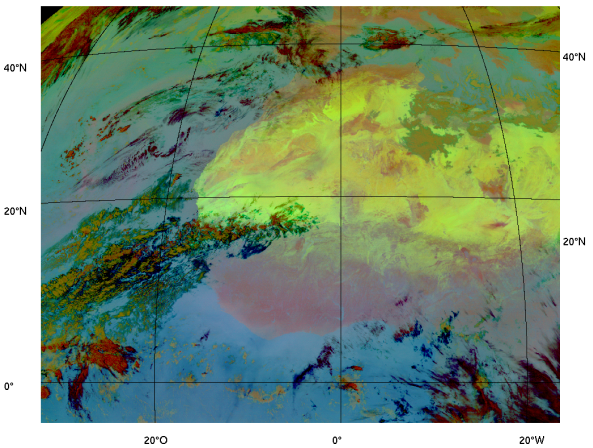

MUSCAT 200801252300

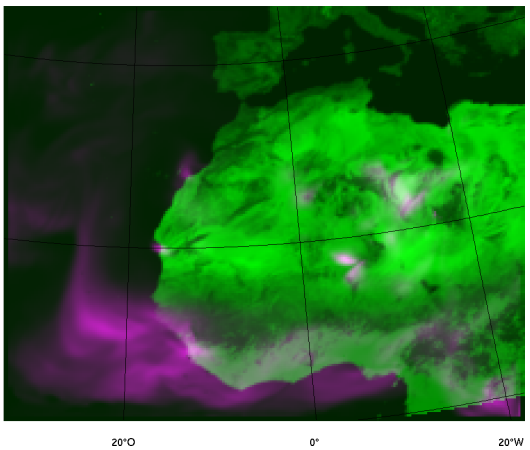

IR Index 200801310100

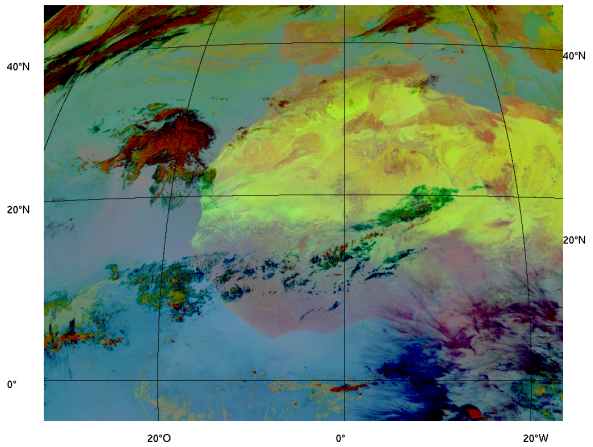

MUSCAT 200801310100

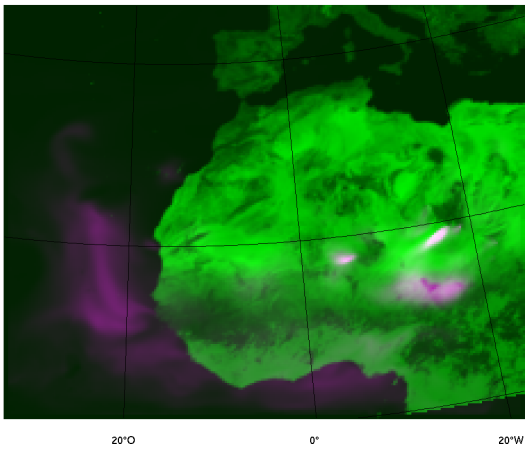

IR Index 200801310200

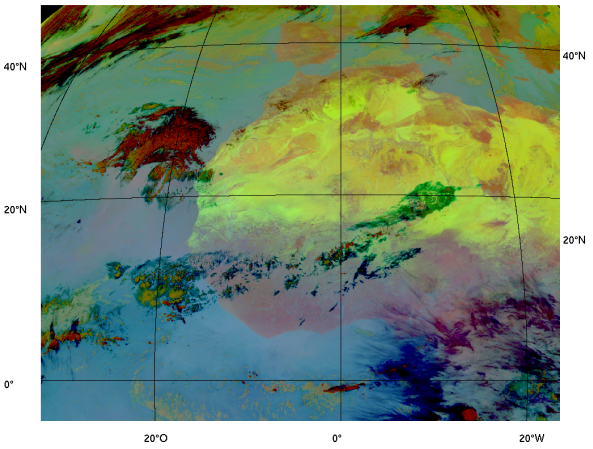

MUSCAT 200801310200

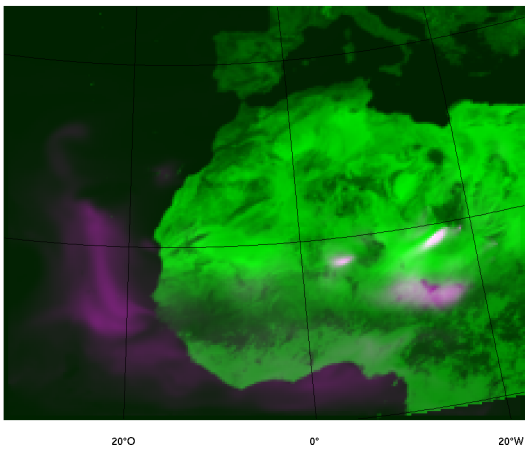

IR Index 200801310300

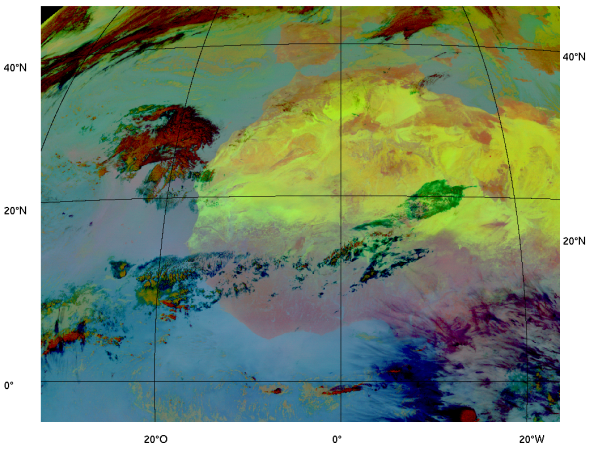

MUSCAT 200801310300

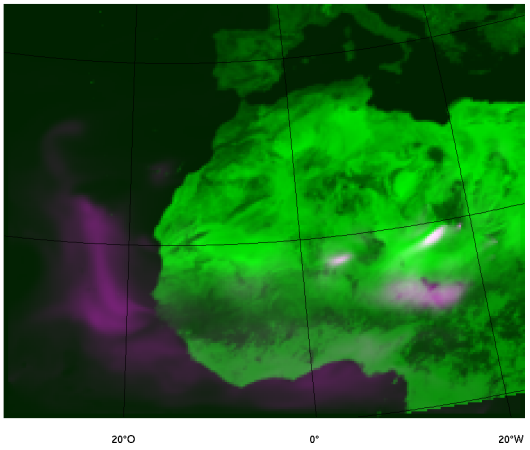

IR Index 200801310400

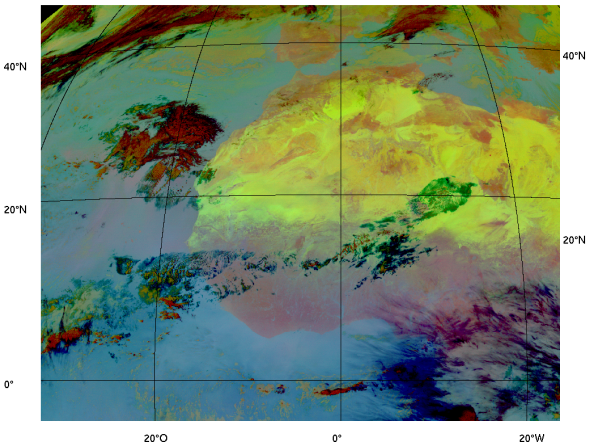

MUSCAT 200801310400

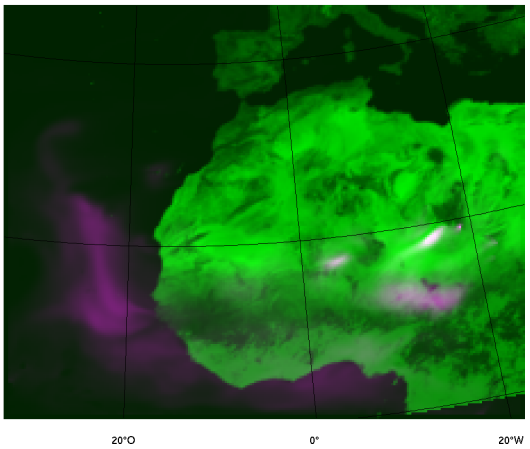

IR Index 200801310500

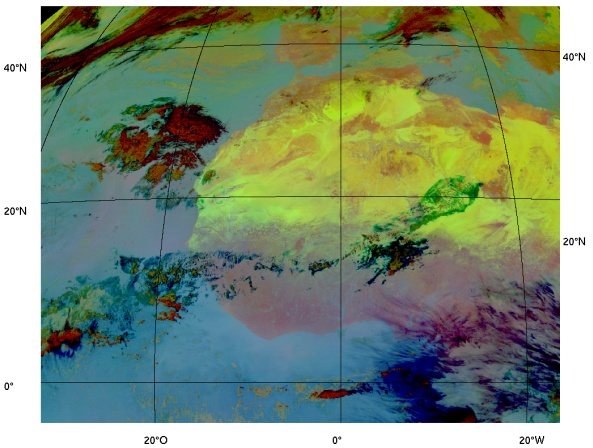

MUSCAT 200801310500

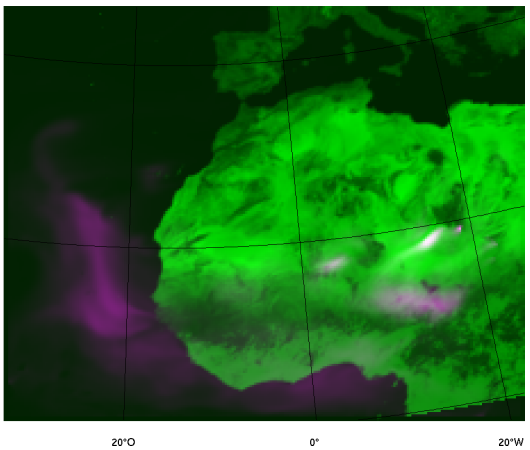

IR Index 200801310600

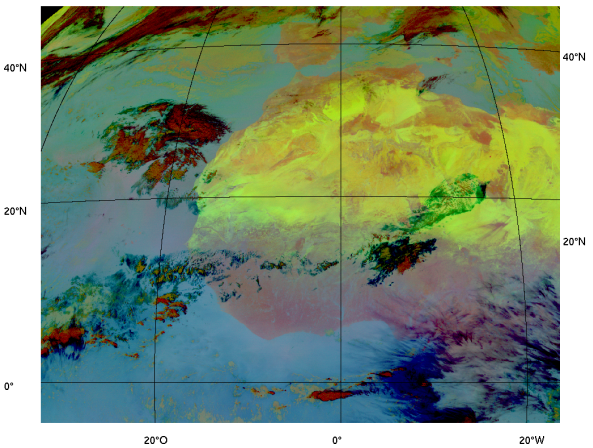

MUSCAT 200801310600

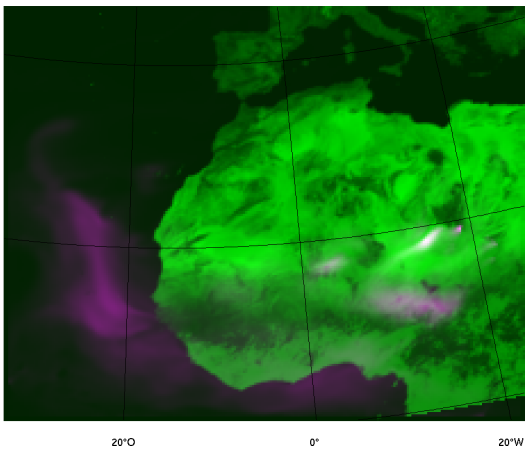

IR Index 200801310700

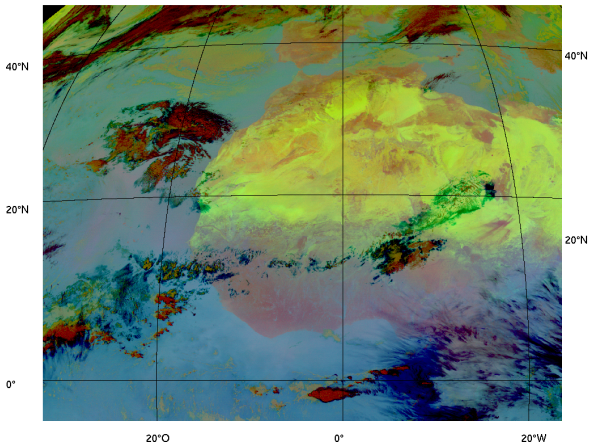

MUSCAT 200801310700

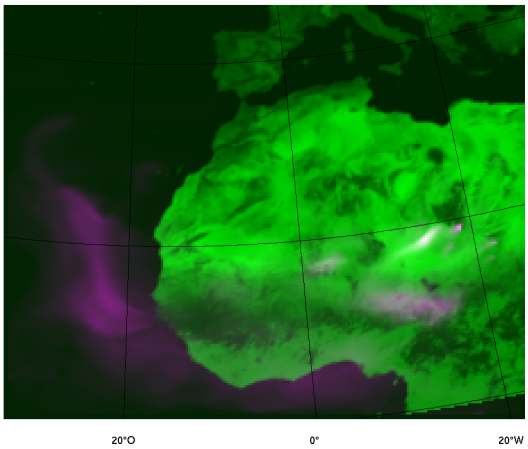

IR Index 200801310800

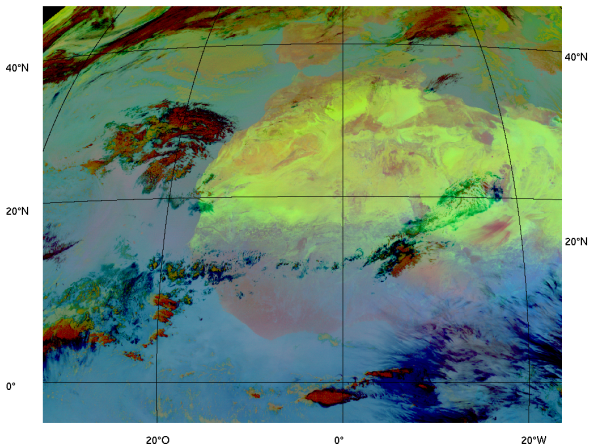

MUSCAT 200801310800

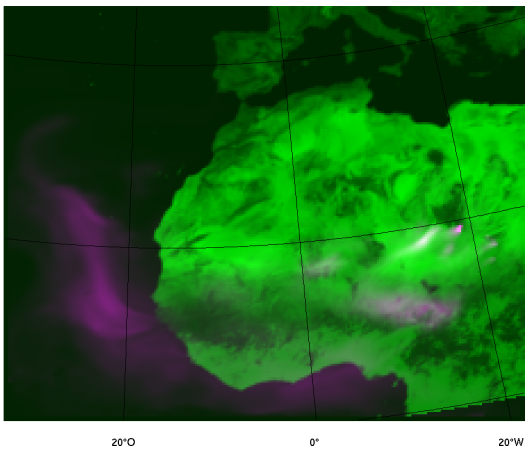

IR Index 200801310900

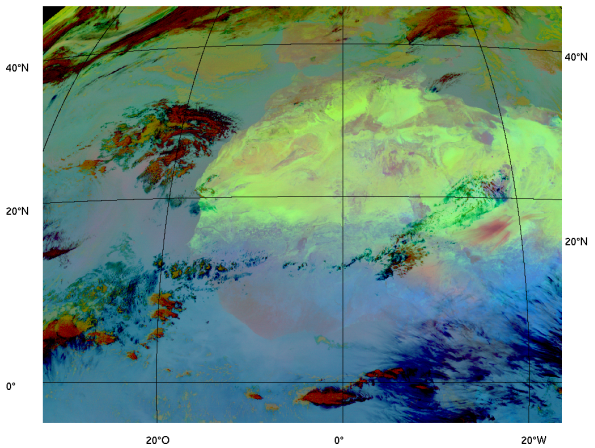

MUSCAT 200801310900

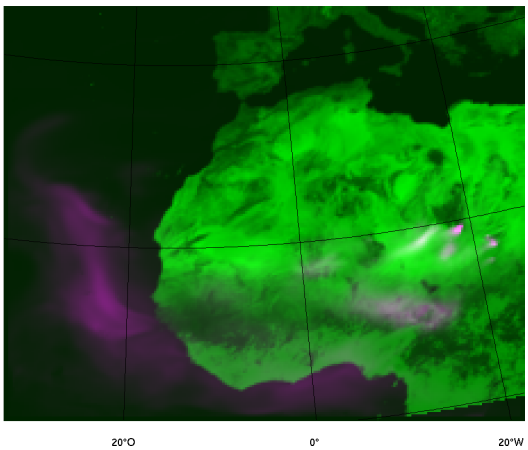

IR Index 200801311000

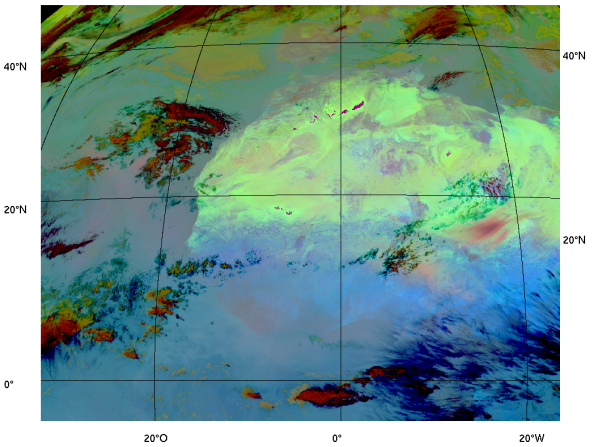

MUSCAT 200801311000

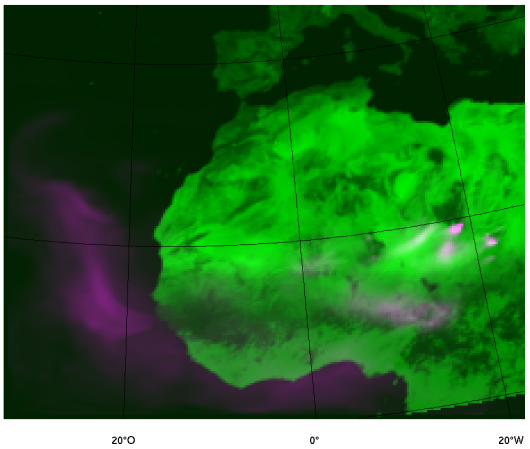

IR Index 200801311100

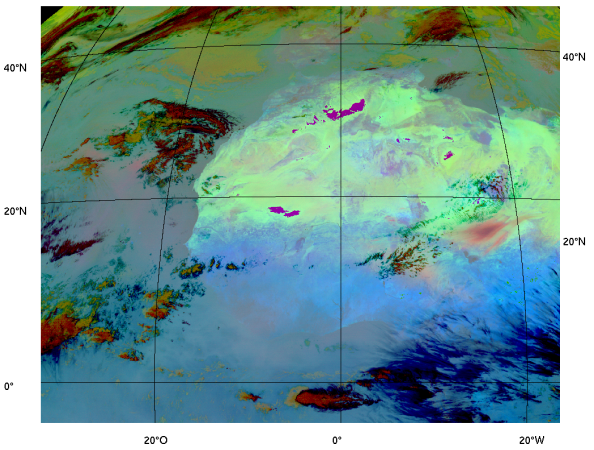

MUSCAT 200801311100

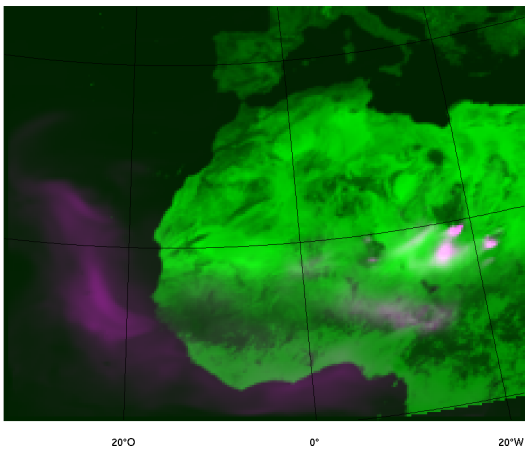

IR Index 200801311200

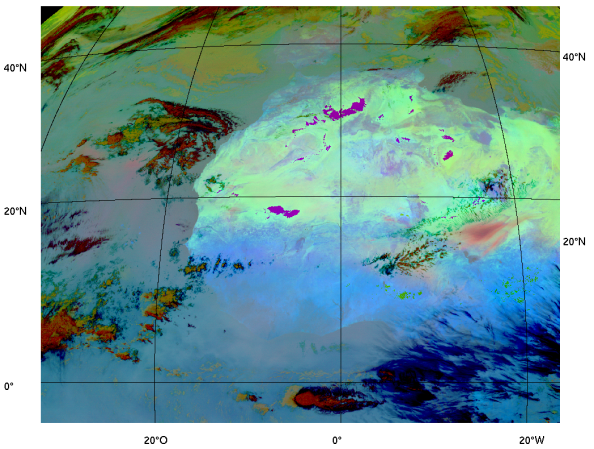

MUSCAT 200801311200

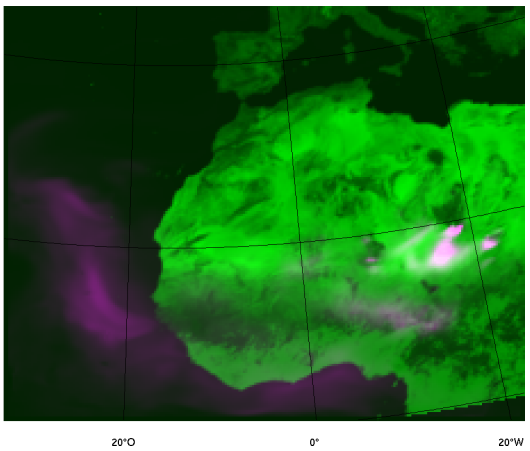

IR Index 200801311300

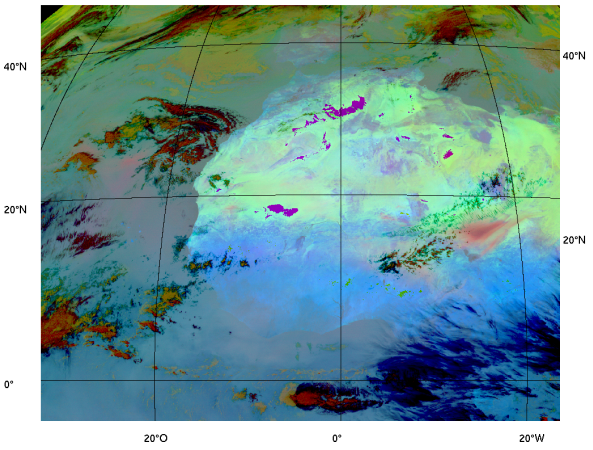

MUSCAT 200801311300

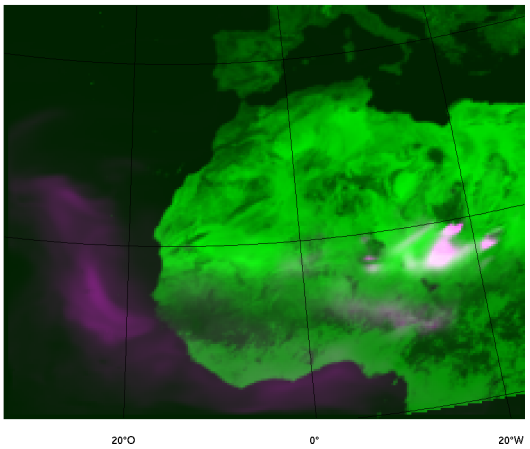

IR Index 200801311400

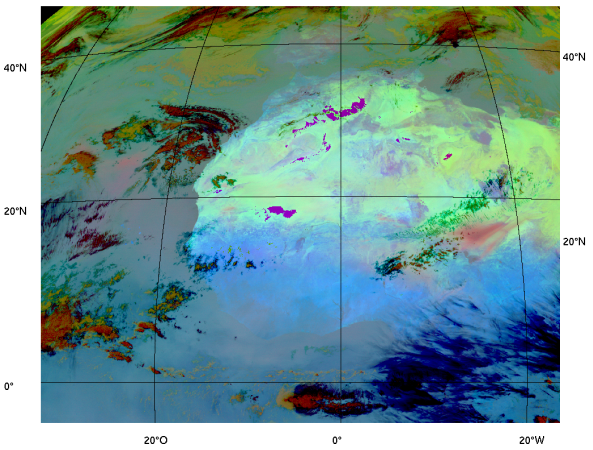

MUSCAT 200801311400

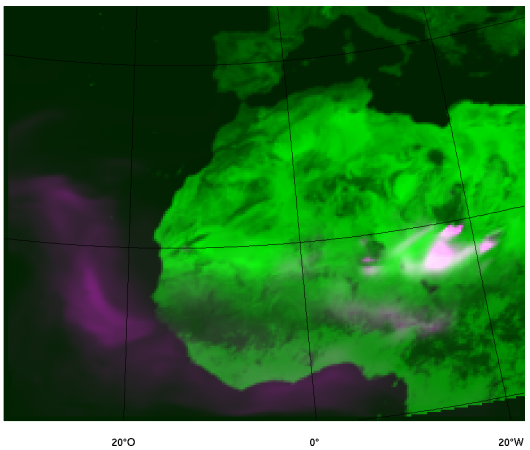

IR Index 200801311500

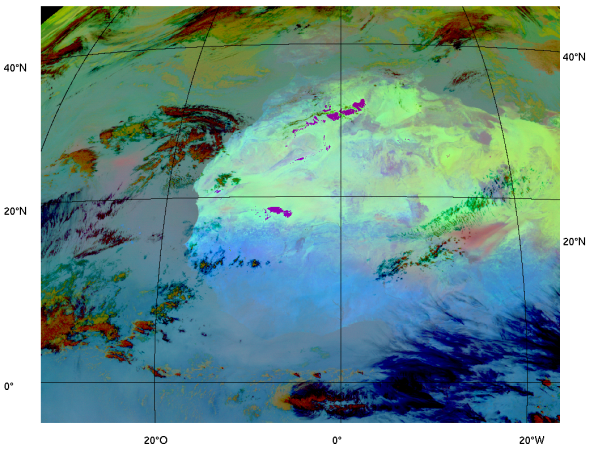

MUSCAT 200801311500

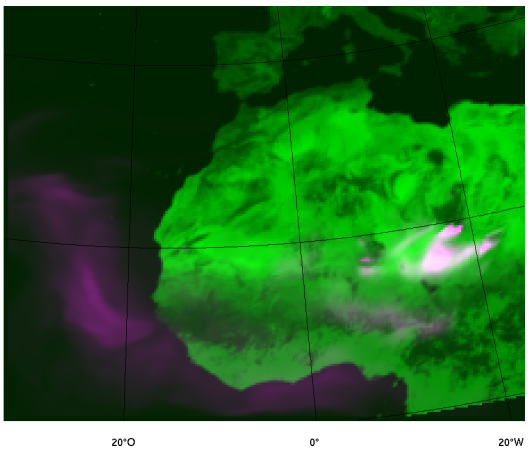

IR Index 200801311600

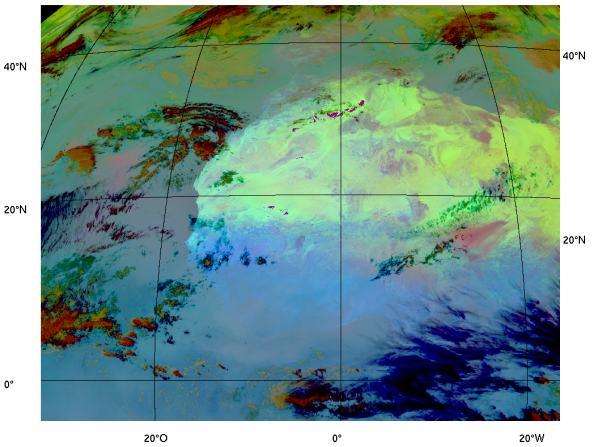

MUSCAT 200801311600

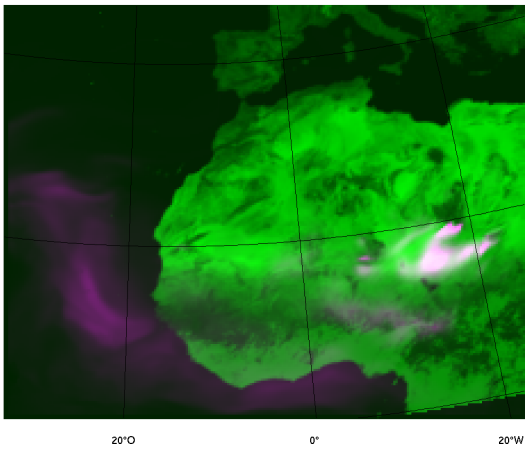

IR Index 200801311700

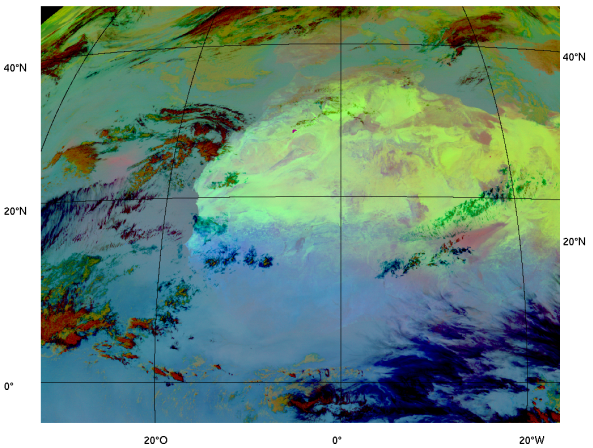

MUSCAT 200801311700

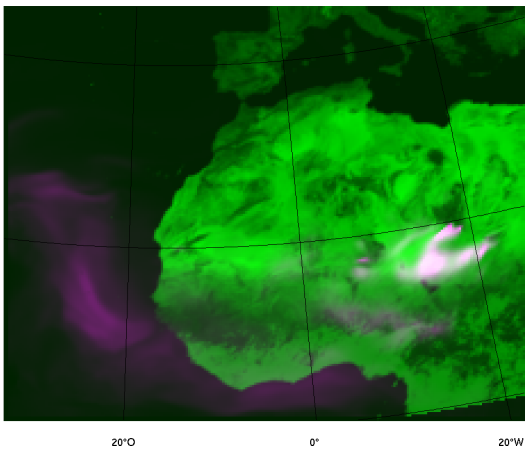

IR Index 200801311800

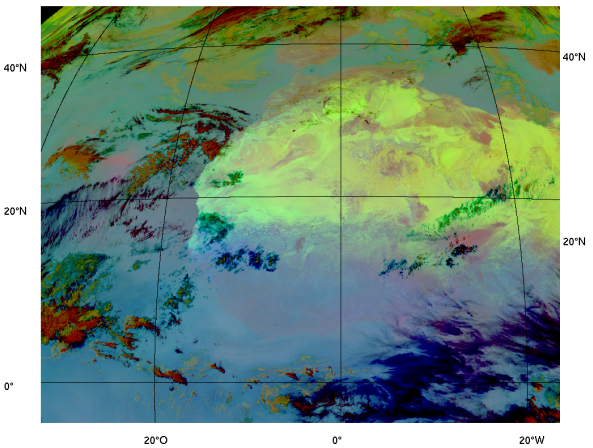

MUSCAT 200801311800

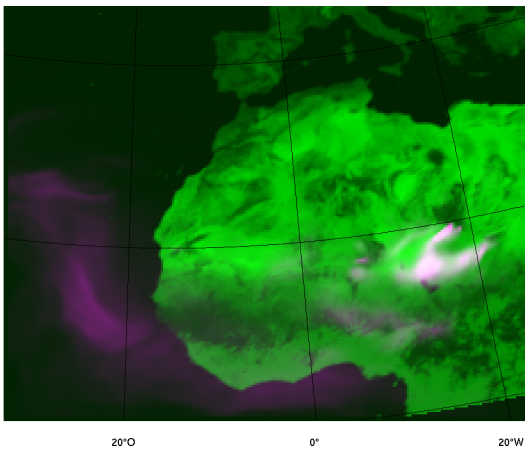

IR Index 200801311900

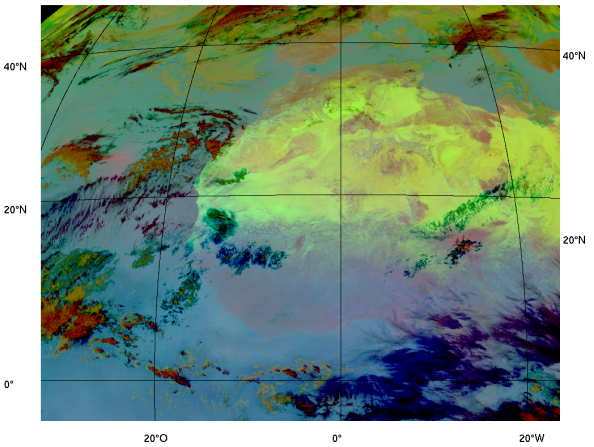

MUSCAT 200801311900

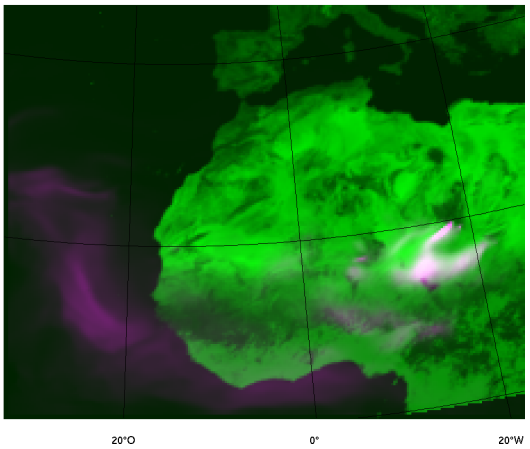

IR Index 200801312000

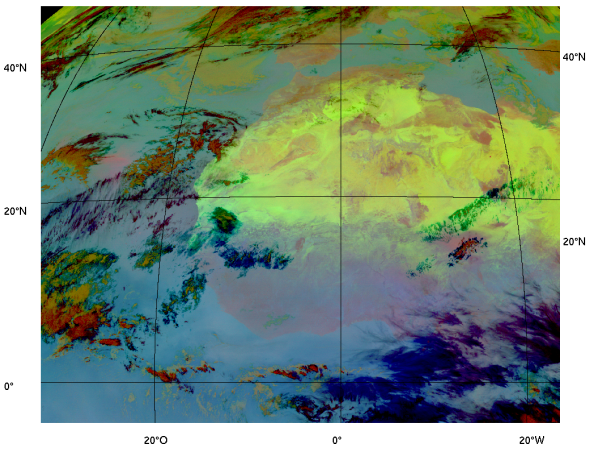

MUSCAT 200801312000

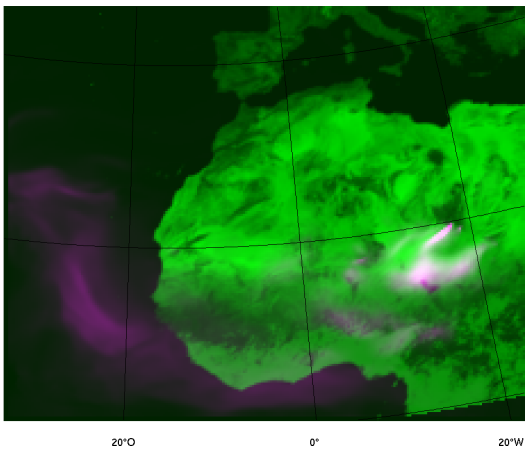

IR Index 200801312100

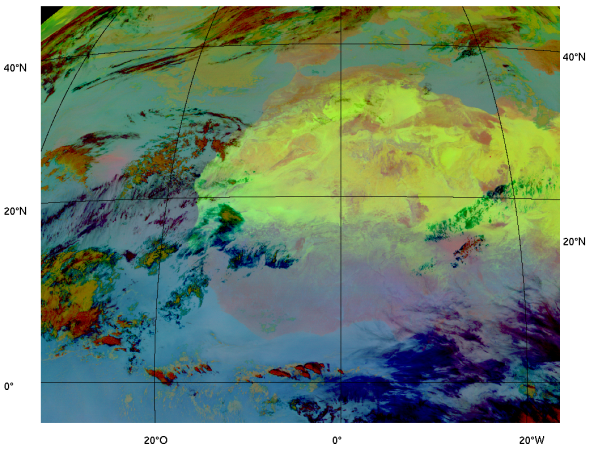

MUSCAT 200801312100

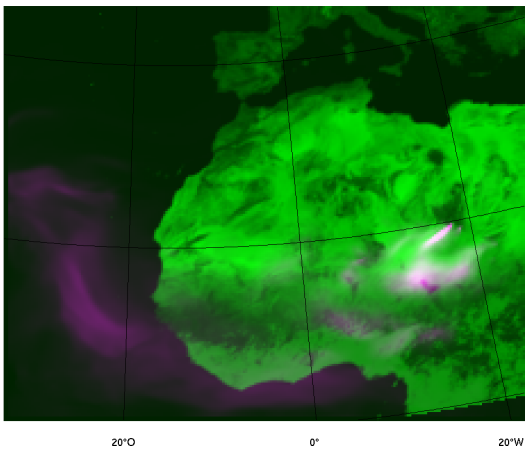

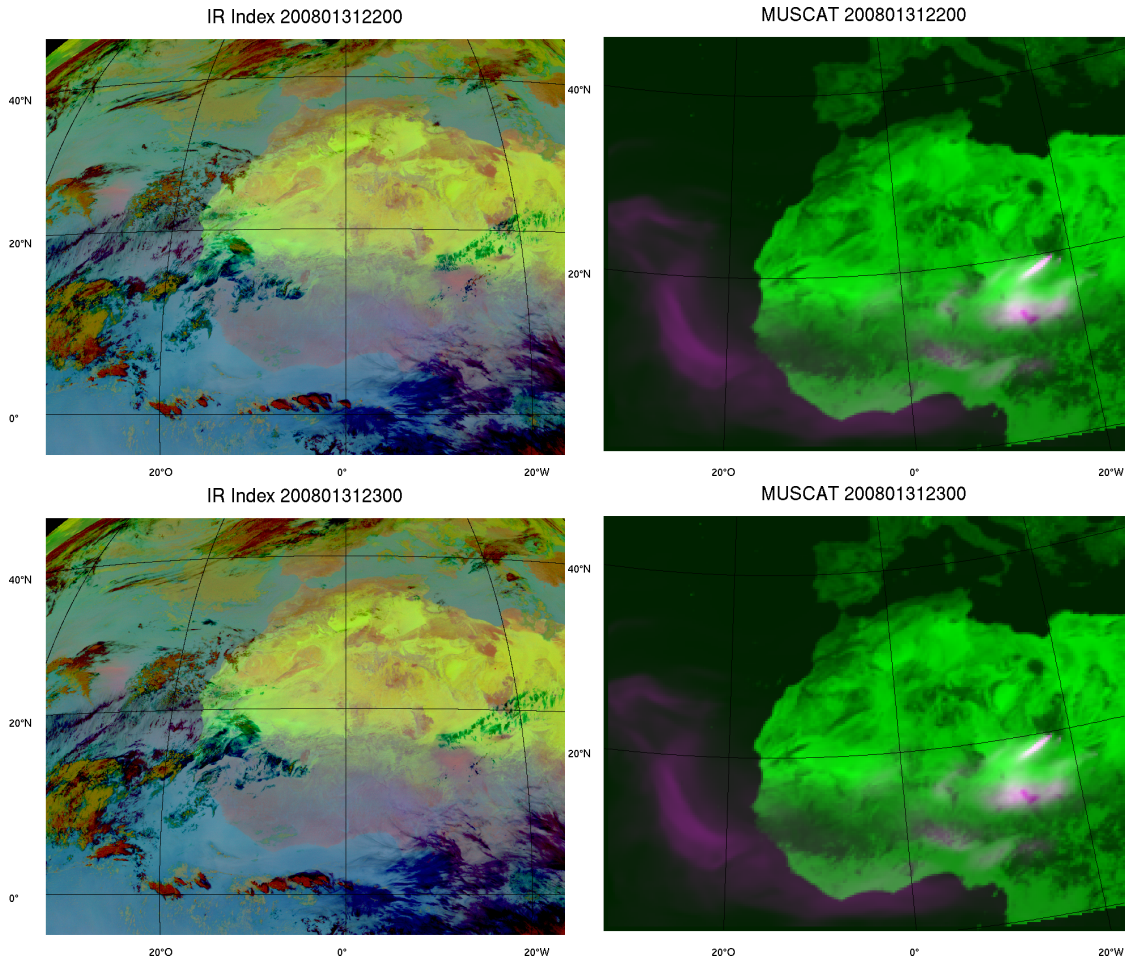

Table 27: Comparison of three different dust scenes: on the left the IR dust index and on the right the modelled dust cloud by MUSCAT. The dust is colored pink and the surface albedo of the moel domain is shaded in green.

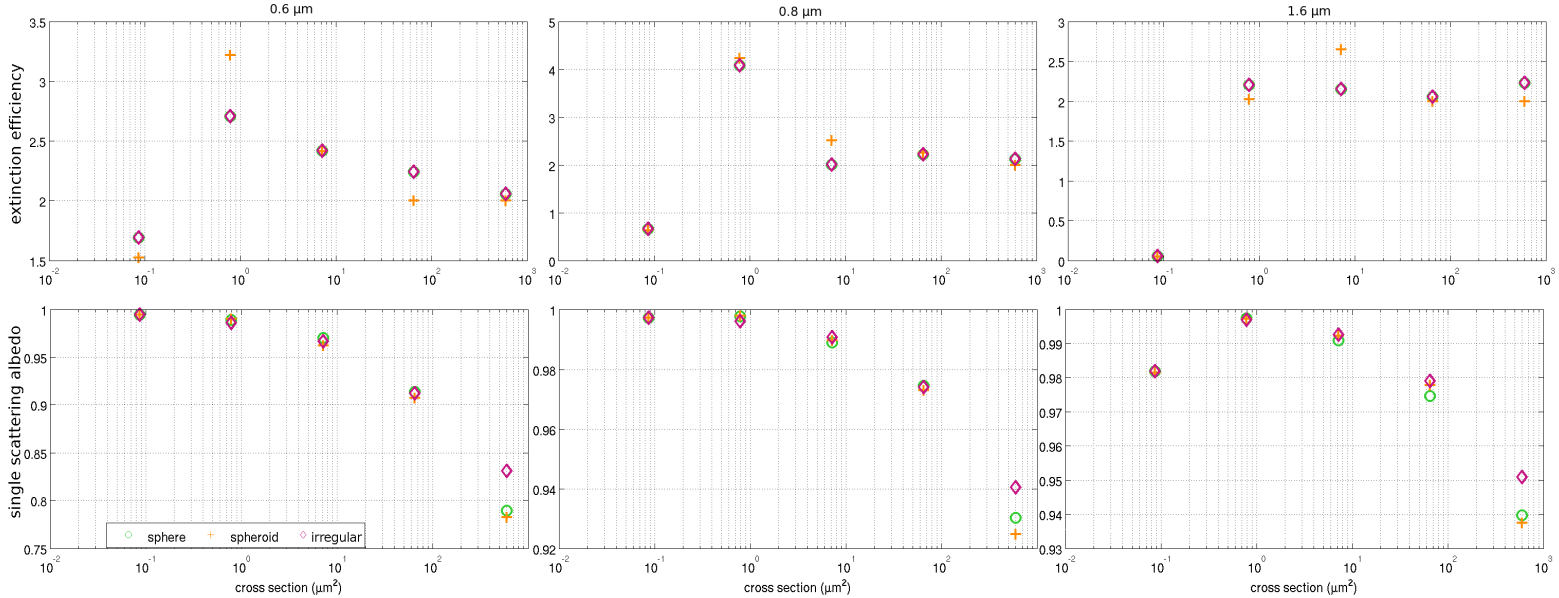

Figure 57: Extinction efficiency and single scattering albedo for three different particle shapes at three wavelengths

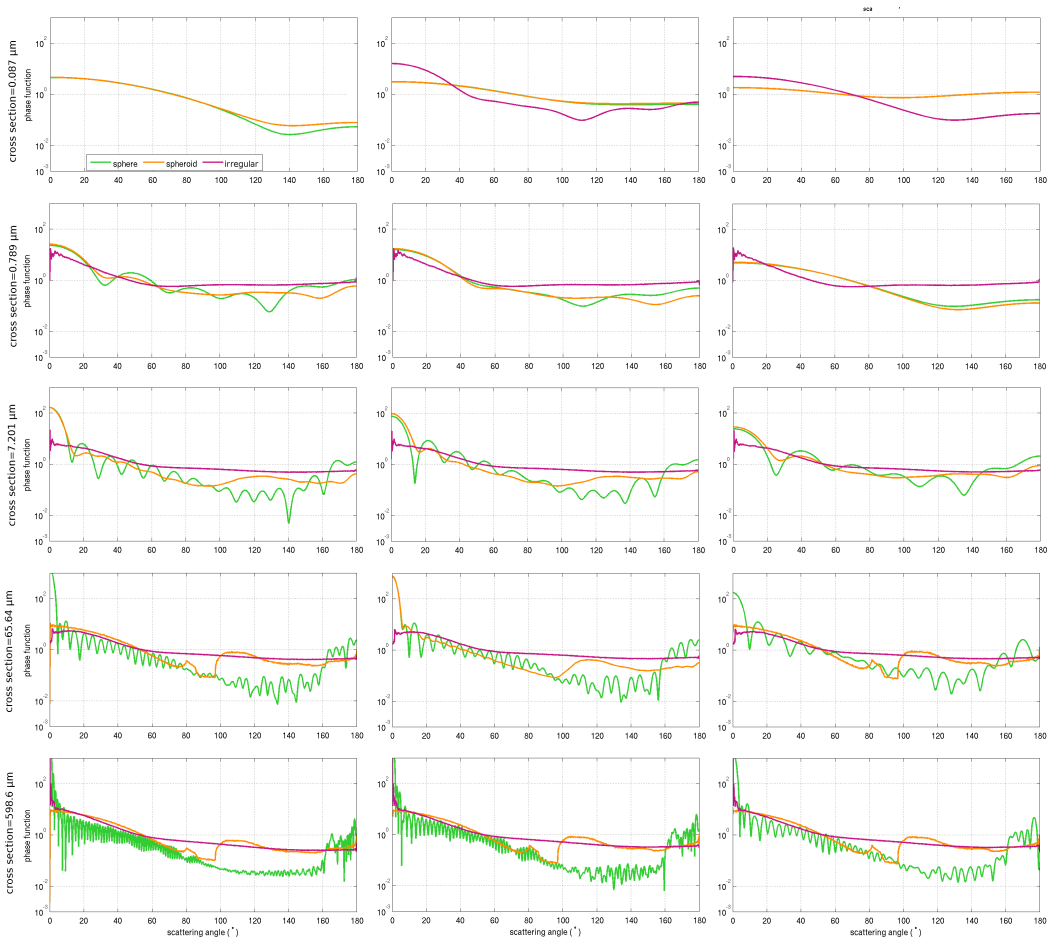

Figure 58: Scattering phase functions for 5 different sizes (scattering cross sectionssc_{sca}) at three wavelengths

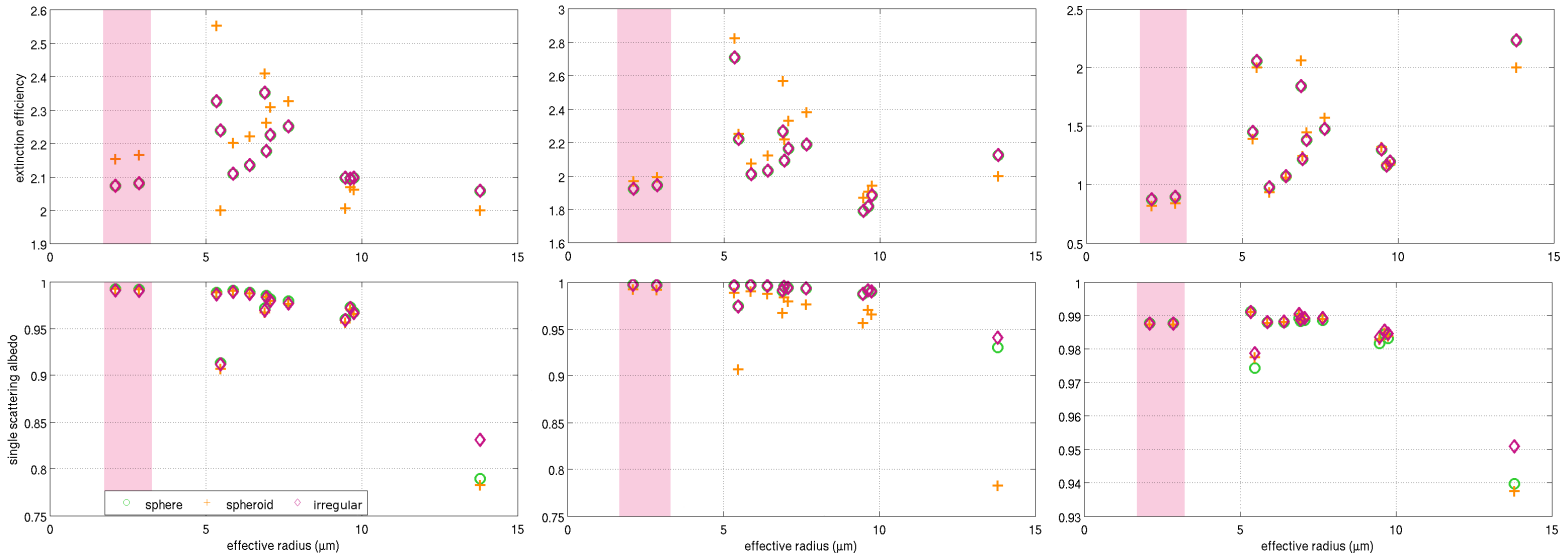

Figure 59: Extinction efficiency and single scattering albedo of 14 different scattering classes depending on their effective radius for three wavelengths

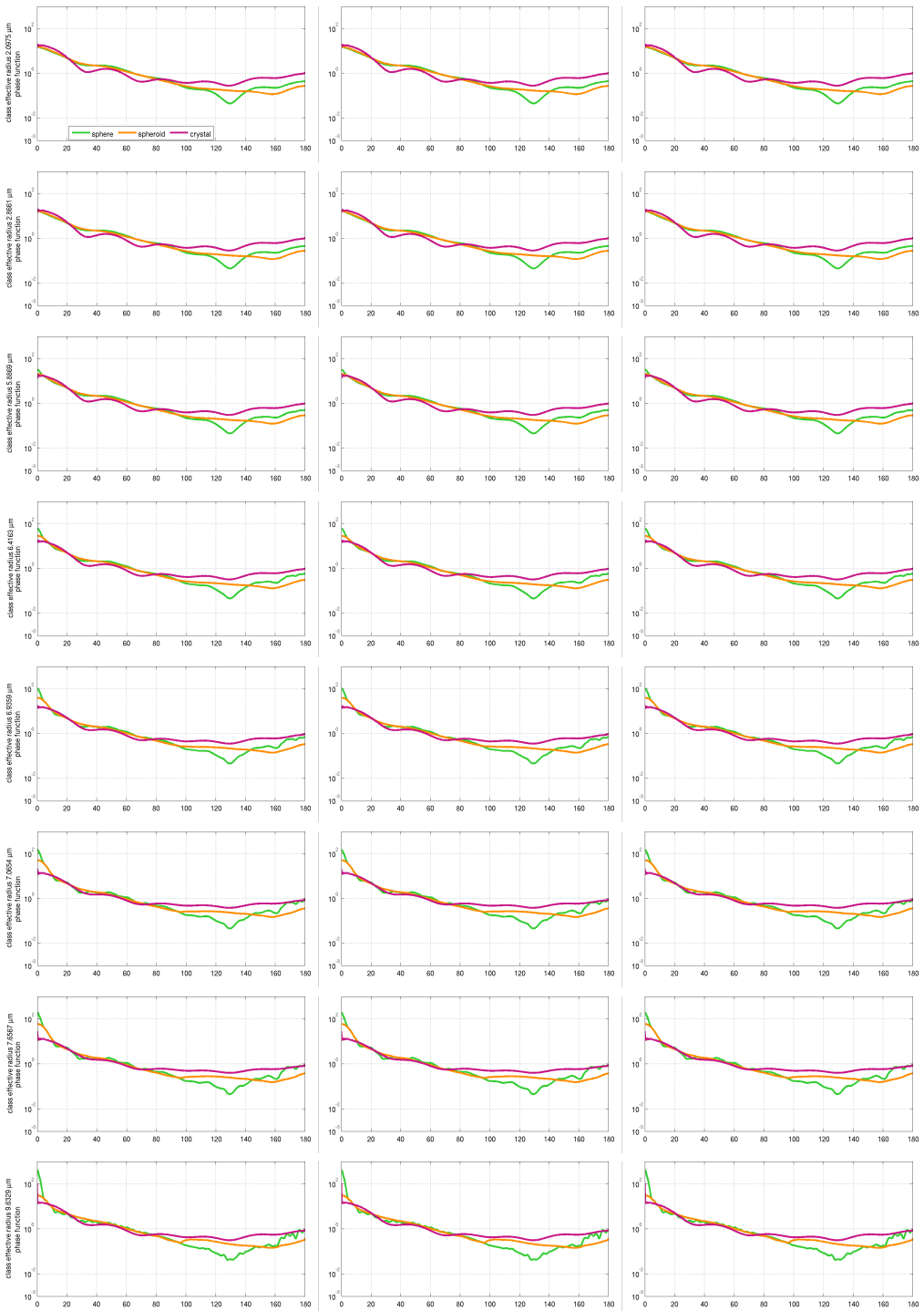
class effective radius 2.0975 µm
class effective radius 2.6681 µm
class effective radius 3.3889 µm
class effective radius 4.4163 µm
class effective radius 6.9359 µm
class effective radius 7.9054 µm
class effective radius 7.8567 µm
class effective radius 9.8329 µm
phase function
sphere
spheroid
crystal

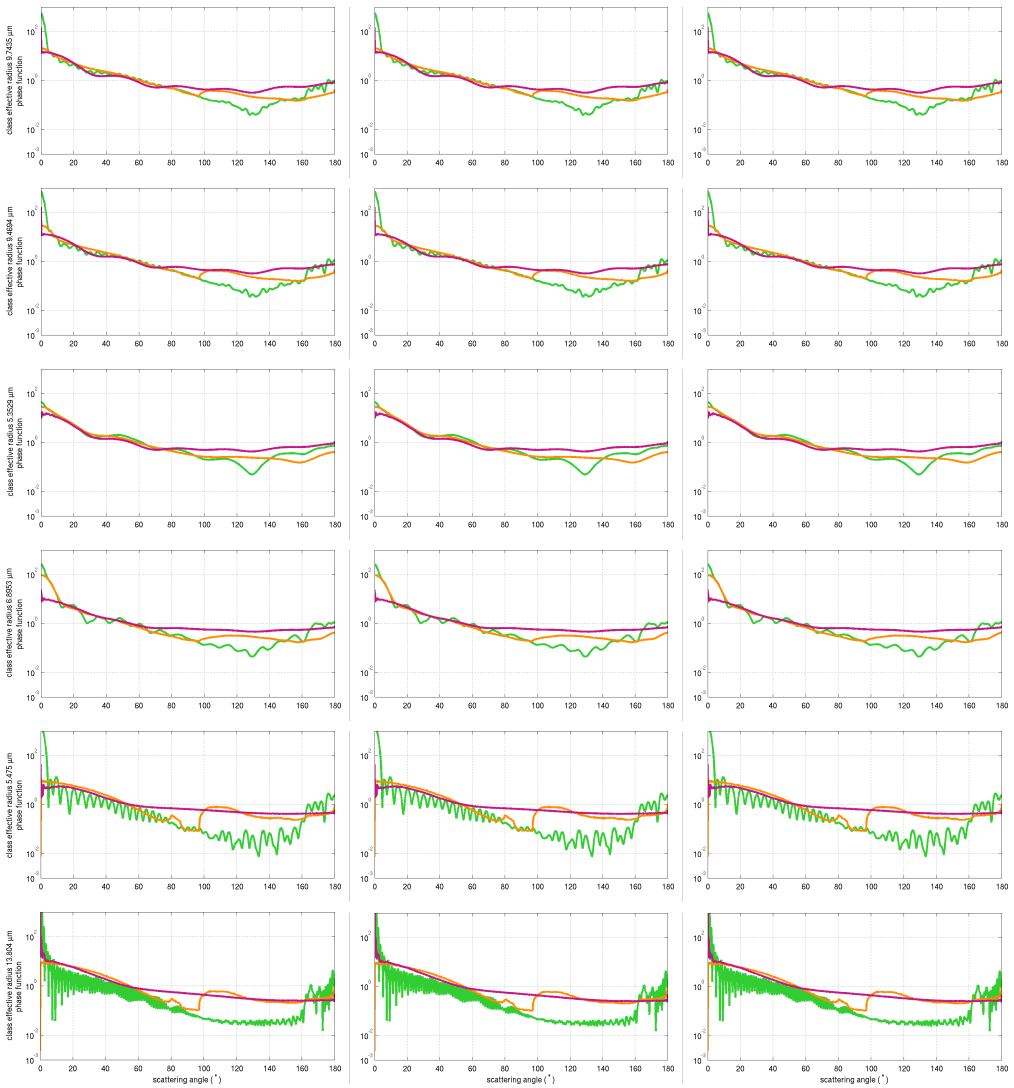

Table 28: Scattering phase functions for 14 scattering classes for three different shapes and three wavelengths

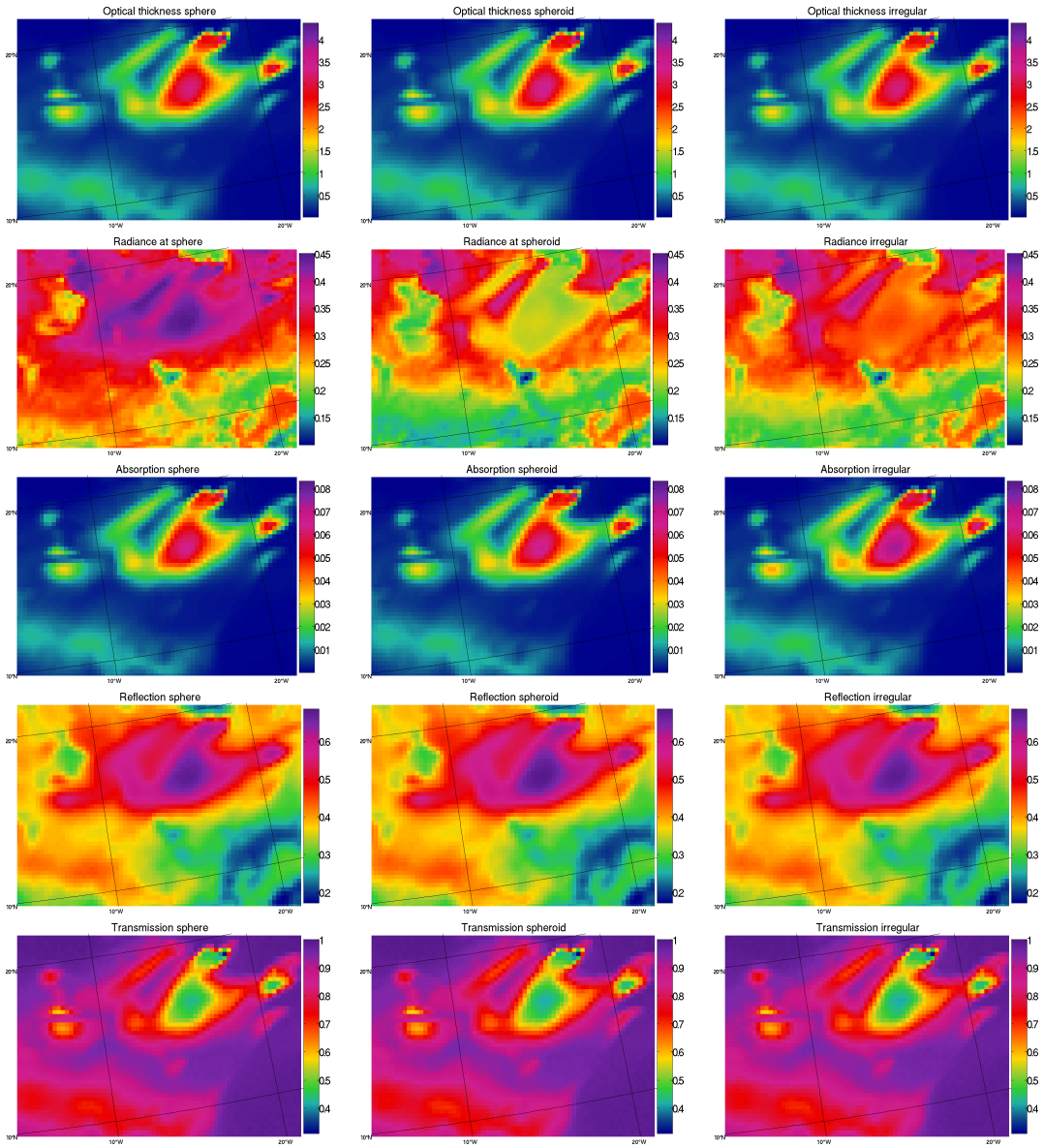

Table 29: Results of radiative transfer simulations with MC-UniK at 0.6μm. The fields are optical thickness, radiance, absorption, reflection and transmission. Simulations are performed for three different shapes, spheres (left column), spheroids (middle column) and irregular shaped particles (right column)

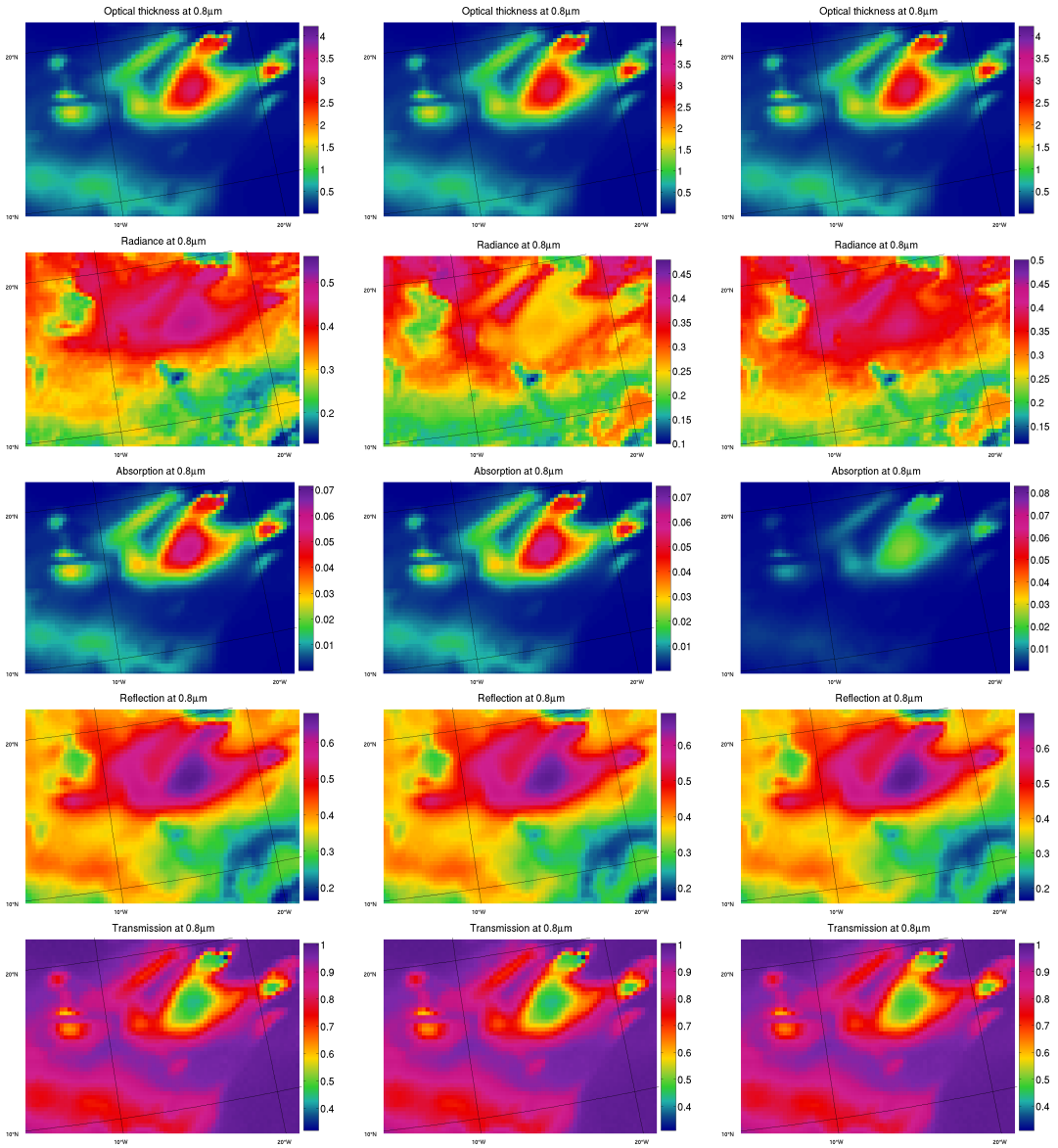

Table 30: Results of radiative transfer simulations with MC-UniK at 0.8µm. The fields are optical thickness, radiance, absorption, reflection and transmission. Simulations are performed for three different shapes, spheres (left column), spheroids (middle column) and irregular shaped particles (right column)

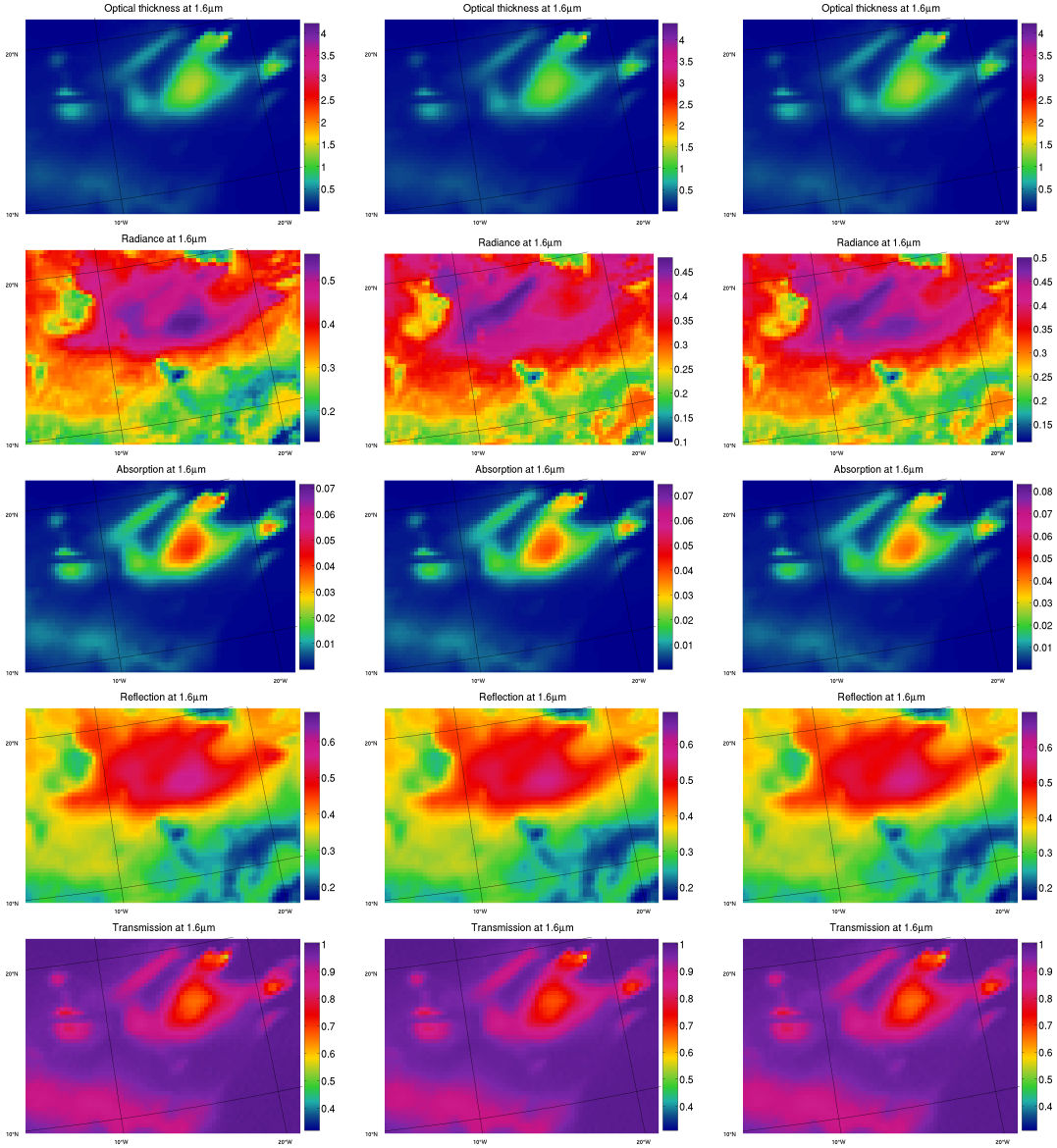

Table 31: Results of radiative transfer simulations with MC-UniK at 1.6µm. The fields are optical thickness, radiance, absorption, reflection and transmission. Simulations are performed for three different shapes, spheres (left column), spheroids (middle column) and irregular shaped particles (right column)

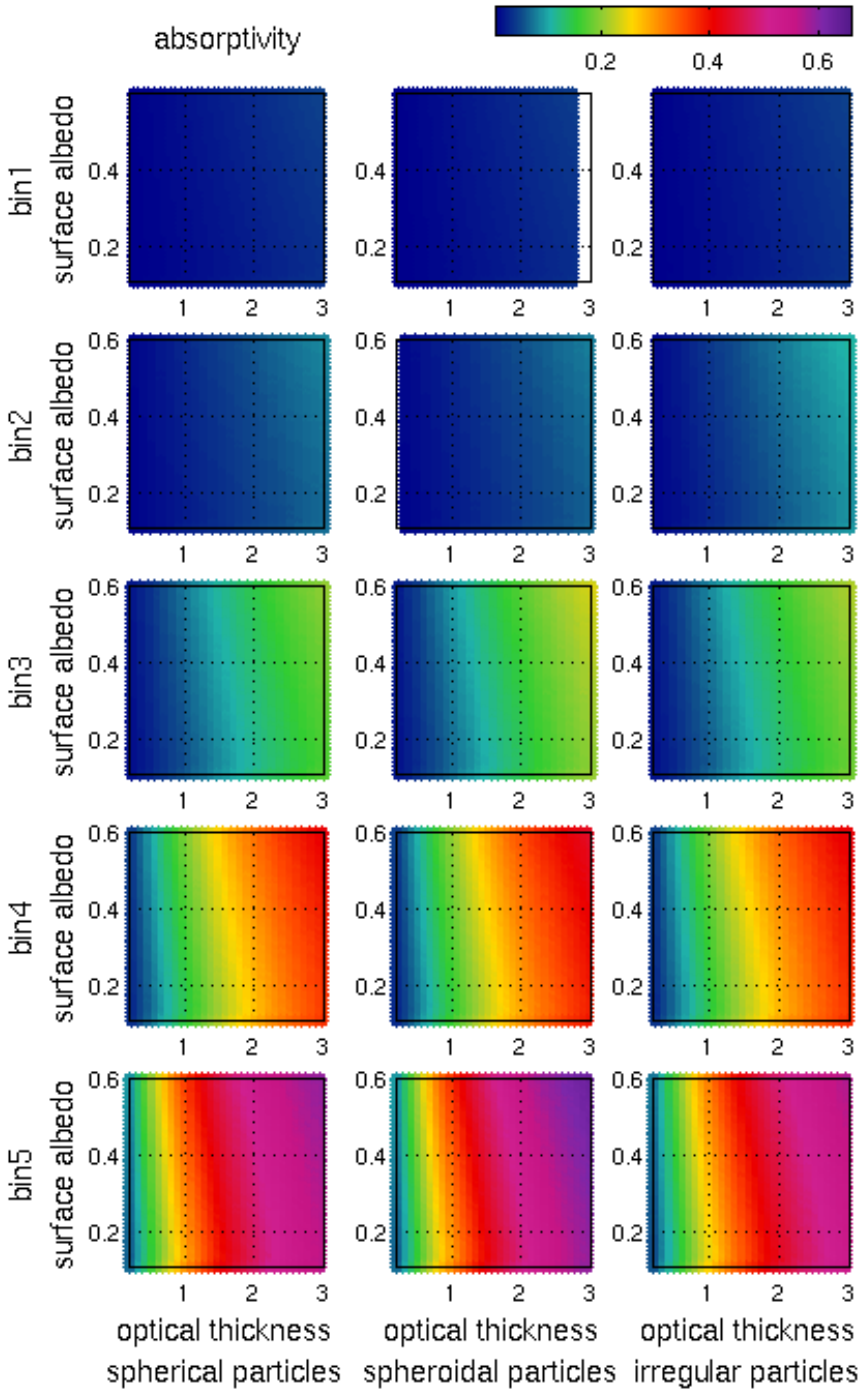

Figure 60: Absorption of the test cloud consisting of spherical, spheroidal and irregular shaped particles depending on the surface albedo and optical thickness, sortetd by particle size.

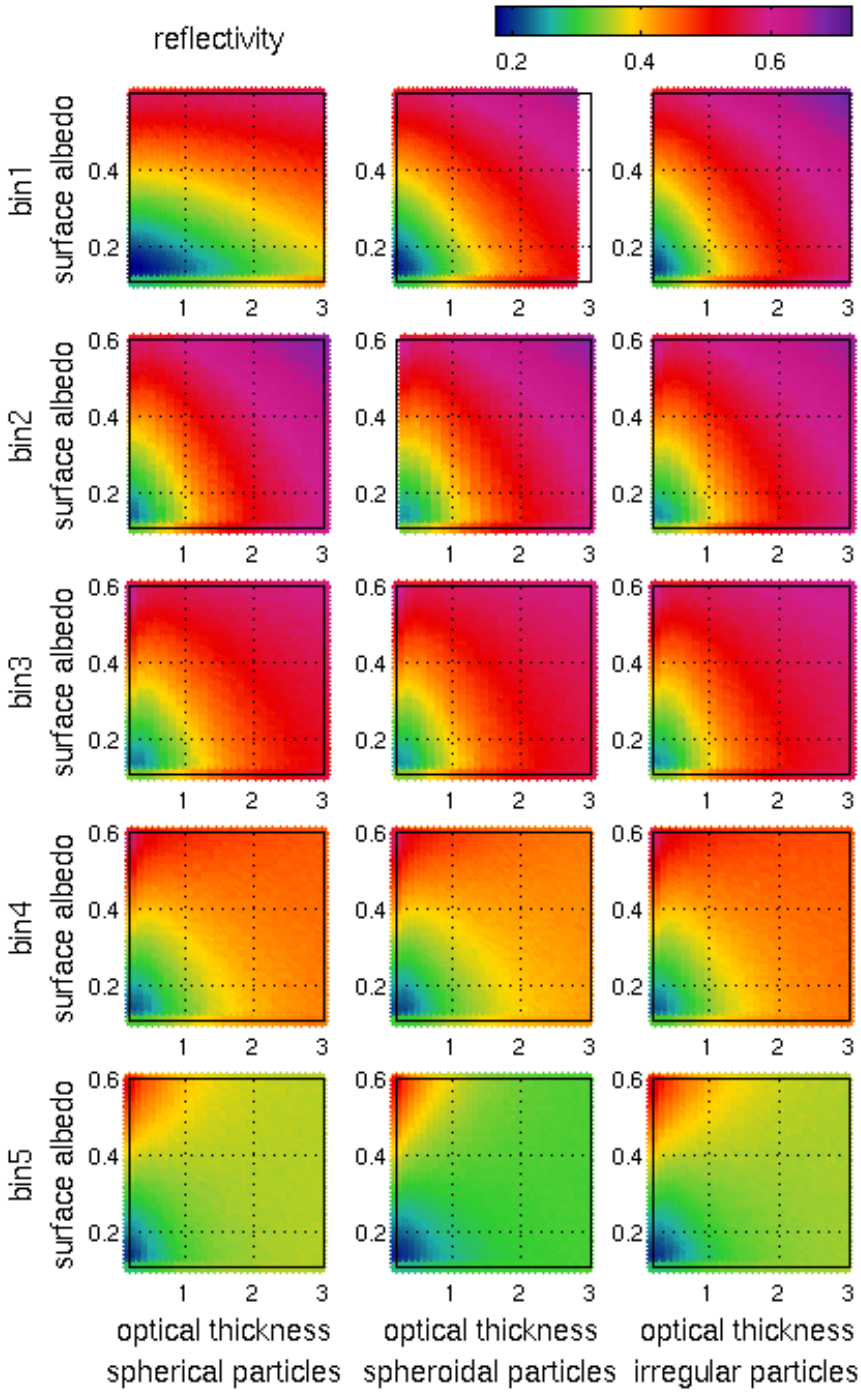

Figure 61: Reflection of the test cloud consisting of spherical, spheroidal and irregular shaped particles depending on the surface albedo and optical thickness, sortetd by particle size.

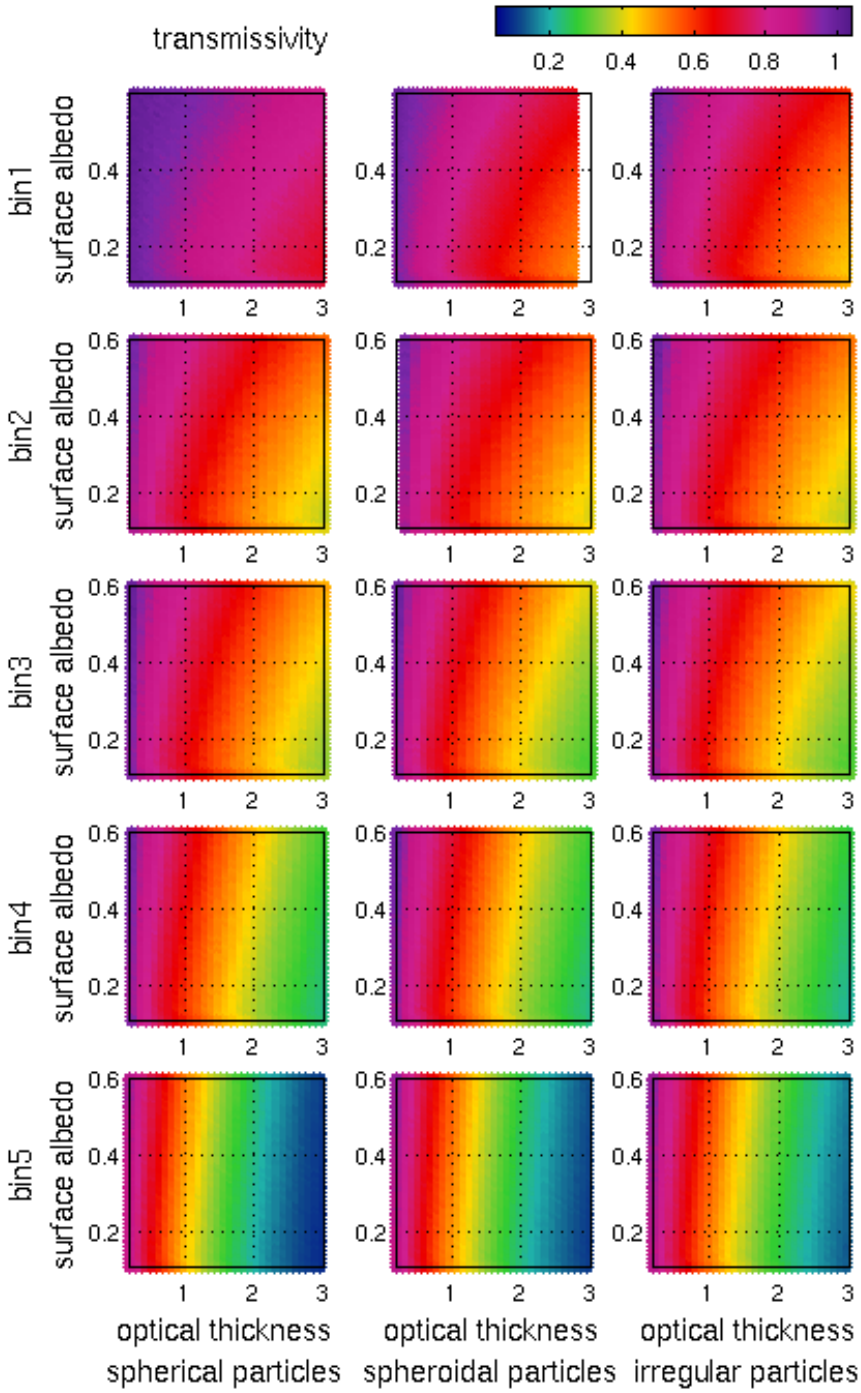

Figure 62: Transmission of the test cloud consisting of spherical, spheroidal and irregular shaped particles depending on the surface albedo and optical thickness, sortetd by particle size.

References

Ackerman, S. A., 1997: Remote sensing aerosols using satellite infrared observations. *Journal of Geophysical Research*, **102**(D14), 17,069–17,079.

Ansmann, A., A. Petzold, K. Kandler, I. Tegen, M. Wendisch, D. Müller, B. Weinzierl, T. Müller, and J. Heintzenberg, 2011: Saharan mineral dust experiments samum–1 and samum–2: what have we learned? *Tellus B*, **63**(4), 403–429.

Arimoto, R., 2001: Eolian dust and climate: relationships to sources, tropospheric chemistry, transport and deposition. *Earth-Science Reviews*, **54**(1-3), 29 – 42.

Balkanski, Y., M. Schulz, T. Claquin, and S. Guibert, 2006: Reevaluation of mineral aerosol radiative forcings suggests a better agreement with satellite and aeronet data. *Atmospheric Chemistry and Physics Discussions*, **6**(5), 8383–8419.

Bauer, E. and A. Ganopolski, 2010: Aeolian dust modeling over the past four glacial cycles with climber-2. *Global and Planetary Change*, **74**(2), 49 – 60.

Bauer, S., E. Bierwirth, M. Esselborn, A. Petzold, A. Macke, T. Trautmann, and M. Wendisch, 2011: Airborne spectral radiation measurements to derive solar radiative forcing of saharan dust mixed with biomass burning smoke particles. *Tellus B*, **63**(4), 742–750.

Benner, T. C. and K. F. Evans, 2001: Three-dimensional solar radiative transfer in small tropical cumulus fields derived from high-resolution imagery. *Journal of Geophysical Research*, **106**, 14,975–14,984.

Birch, K. P. and M. J. Downs, 1993: An updated edlén equation for the refractive index of air. *Metrologia*, **30**(3), 155.

Bristow, C. S., N. Drake, and S. Armitage, 2009: Deflation in the dustiest place on earth: The bodele depression, chad. *Geomorphology*, **105**(1-2), 50 – 58. Contemporary research in aeolian geomorphology - 6th International Conference on Aeolian Research (ICAR VI).

Bristow, C. S., K. A. Hudson-Edwards, and A. Chappell, 2010: Fertilizing the amazon and equatorial atlantic with west african dust. *Geophysical Research Letters*, **37**, 5 PP.

Cahalan, R. F., L. Oreopoulos, A. Marshak, K. F. Evans, A. B. Davis, R. M. Pincus, K. H. Yetzer, B. Mayer, R. Davies, T. P. Ackerman, H. W. Barker, E. E. Clothiaux, R. G. Ellingson, M. J. Garay, E. I. Kassianov, S. Kinne, A. Macke, W. O'Hirok, P. T. Partain, S. M. Prigarin, A. N. Rublev, G. L. Stephens, F. Szczap, E. E. Takara, T. Varnai, G. Wen, and T. B. Zhuravleva, 2005: The i3rc: Bringing together the most advanced radiative transfer tools for cloudy atmospheres. *Bull. Amer. Meteor. Soc.*, **86**, 1275–1293.

Christopher, S. A. and T. A. Jones, 2010: Satellite and surface-based remote sensing of saharan dust aerosols. *Remote Sensing of Environment*, **114**(5), 1002 – 1007.

Clerbaux, N., 2006: Imager processing : Data dictionary. *Technical Note MSG-RMIB-GE-TN-0024*, p. 33 pp.

Davis, A. B., A. Marshak, W. J. Wiscombe, and R. F. Cahalan, 1997: Insight into three-dimensional radiation transport processes from diffusion theory, with applications to the atmosphere. *ICHMT DIGITAL LIBRARY ONLINE*, **6**.

Di Giuseppe, F. and A. M. Tompkins, 2003: Effect of spatial organization on solar radiative transfer in three-dimensional idealized stratocumulus cloud fields. *Journal of Atmospheric Science*, **60**, 1774–1794.

EDLÉN, B., 1953: The dispersion of standard air. *J. Opt. Soc. Am.*, **43**(5), 339–344.

Engelstaedter, S., I. Tegen, and R. Washington, 2006: North african dust emissions and transport. *Earth-Science Reviews*, **79**(1-2), 73 – 100.

Evan, A. T., J. Dunion, J. A. Foley, A. K. Heidinger, and C. S. Velden, 2006: New evidence for a relationship between Atlantic tropical cyclone activity and African dust outbreaks. *Geophysical Research Letters*, **331**, L19813.

Evans, K. F., 1998: The spherical harmonics discrete ordinate method for three-dimensional atmospheric radiative transfer. *Journal of the Atmospheric Sciences*, **55**(3), 429–446.

Fu, Q., T. Thorsen, J. Su, J. Ge, and J. Huang, 2009: Test of mie-based single-scattering properties of non-spherical dust aerosols in radiative flux calculations. *Journal of Quantitative Spectroscopy and Radiative Transfer*, **110**(14-16), 1640 – 1653. <ce:title>XI Conference on Electromagnetic and Light Scattering by Non-Spherical Particles: 2008</ce:title>.

Garrison, V. H., E. A. Shinn, W. T. Foreman, D. W. Griffin, C. W. Holmes, C. A. Kellogg, M. S. Majewski, L. L. Richardson, K. B. Ritchie, and G. W. Smith, 2003: African and asian dust: From desert soils to coral reefs. *BioScience*, **53**(5), 469–480.

Giles, J., 2005: Climate science: The dustiest place on earth. *Nature*, **434**, 816–819.

Ginoux, P., J. M. Prospero, O. Torres, and M. Chin, 2004: Long-term simulation of global dust distribution with the gocart model: correlation with north atlantic oscillation. *Environmental Modelling and Software*, **19**(2), 113 – 128. Modelling of Wind Erosion and Aeolian Processes.

Goudie, A. S. and N. J. Middleton, 2001: Saharan dust storms: nature and consequences. *Earth-Science Reviews*, **56**(1-4), 179 – 204.

Griffin, D., V. Garrison, J. Herman, and E. Shinn, 2001: African desert dust in the caribbean atmosphere: Microbiology and public health. *Aerobiologia*, **17**, 203–213. 10.1023/A:1011868218901.

Griffin, D., C. Kellogg, V. Garrison, and E. Shinn, 2002: The Global Transport of Dust An intercontinental river of dust, microorganisms and toxic chemicals flows through the Earth's atmosphere. *American Scientist*, **90**(3), 228–235.

Hansen, J. E. and L. D. Travis, 1974: Light scattering in planetary atmospheres. *Space Science Reviews*, **16**, 527–610. 10.1007/BF00168069.

Harrison, S. P., K. E. Kohfeld, C. Roelandt, and T. Claquin, 2001: The role of dust in climate changes today, at the last glacial maximum and in the future. *Earth-Science Reviews*, **54**(1-3), 43 – 80.

Haywood, J. and O. Boucher, 2000: Estimates of the direct and indirect radiative forcing due to tropospheric aerosols: A review. *Reviews of Geophysics*, **38**(4), 513–543.

Heinold, B., I. Tegen, S. Bauer, and M. Wendisch, 2011a: Regional modelling of saharan dust and biomass-burning smoke. *Tellus B*, **63**(4), 800–813.

Heinold, B., I. Tegen, K. Schepanski, M. Tesche, M. Esselborn, V. Freudenthaler, S. Gross, K. Kandler, P. Knippertz, D. Müller, A. Schladitz, C. Toledano, B. Weinzierl, A. Ansmann, D. Althausen, T. Müller, A. Petzold, and A. Wiedensohler, 2011b: Regional modelling of saharan dust and biomass-burning smoke. *Tellus B*, **63**(4), 781–799.

Heintzenberg, J., 2009: The samum-1 experiment over southern morocco: overview and introduction. *Tellus B*, **61**(1), 2–11.

Hirsch, J., 2005: *Reflexion des Lichtes*, volume hg. von Manfred von Ardenne, Gerhard Musiol und Uwe Klemradt. 3. Auflage.

Holmes, J. A., 2008: How the sahara became dry. *Science*, **320**(5877), 752–753.

House, L. and L. Avery, 1969: The monte carlo technique applied to radiative transfer. *Journal of Quantitative Spectroscopy and Radiative Transfer*, **9**(12), 1579 – 1591.

Hovenier, J., 2011: Scattering matrix elements. *Amsterdam light scattering data base*.

Jickells, T. D., Z. S. An, K. K. Andersen, A. R. Baker, G. Bergametti, N. Brooks, J. J. Cao, P. W. Boyd, R. A. Duce, K. A. Hunter, H. Kawahata, N. Kubilay, J. laRoche, P. S. Liss, N. Mahowald, J. M. Prospero, A. J. Ridgwell, I. Tegen, and R. Torres, 2005: Global iron connections between desert dust, ocean biogeochemistry, and climate. *Science*, **308**(5718), 67–71.

Kalashnikova, O. and I. Sokolik, 2004: Modeling the radiative properties of nonspherical soil-derived mineral aerosols. *Journal of Quantitative Spectroscopy and Radiative Transfer*, **87**(2), 137 – 166.

Kalashnikova, O. V. and I. N. Sokolik, 2002: Importance of shapes and compositions of wind-blown dust particles for remote sensing at solar wavelengths. *Geophysical Research Letters*, **29**(10), 1398.

Kandler, K., L. Schütz, C. Deutscher, M. Ebert, H. Hofmann, S. Jäckel, R. Jaenicke, P. Knippertz, K. Lieke, A. Massling, A. Petzold, A. Schladitz, B. Weinzierl, A. Wiedensohler, S. Zorn, and S. Weinbruch, 2009: Size distribution, mass concentration, chemical and

mineralogical composition and derived optical parameters of the boundary layer aerosol at tinfou, morocco, during samum 2006. *Tellus B*, **61**(1), 32–50.

Kaufman, Y. J., I. Koren, L. A. Remer, D. Rosenfeld, and Y. Rudich, 2005: The effect of smoke, dust, and pollution aerosol on shallow cloud development over the atlantic ocean. *Proceedings of the National Academy of Sciences of the United States of America*, **102**(32), 11207–11212.

Kellogg, C. A. and D. W. Griffin, 2006: Aerobiology and the global transport of desert dust. *Trends in Ecology and Evolution*, **21**(11), 638 – 644.

Kiehl, J. T. and K. E. Trenberth, 1997: Earth's annual global mean energy budget. *Bull. Amer. Meteor. Soc*, pp. 197–208.

Koren, I., Y. J. Kaufman, R. Washington, M. C. Todd, Y. Rudich, J. V. Martins, and D. Rosenfeld, 2006: The bodele depression: a single spot in the sahara that provides most of the mineral dust to the amazon forest. *Environmental Research Letters*, **1**(1), 014005.

Kroepelin, S., 2006: Revisiting the age of the sahara desert. *Science*, **312**(5777), 1138–1139.

Macke, A. and M. I. Mishchenko, 1996: Applicability of regular particle shapes in light scattering calculations for atmospheric ice particles. *Appl. Opt.*, **35**(21), 4291–4296.

Macke, A., M. I. Mishchenko, K. Muinonen, and B. E. Carlson, 1995: Scattering of light by large nonspherical particles: ray-tracing approximation versus t-matrix method. *Opt. Lett.*, **20**(19), 1934–1936.

Macke, A., D. Mitchell, and L. Bremen, 1999: Monte carlo radiative transfer calculations for inhomogeneous mixed phase clouds. *Physics and Chemistry of the Earth, Part B: Hydrology, Oceans and Atmosphere*, **24**(3), 237 – 241.

Maring, H., D. L. Savoie, M. A. Izaguirre, L. Custals, and J. S. Reid, 2003: Mineral dust aerosol size distribution change during atmospheric transport. *Journal of Geophysical Research*, **108**(D19), 6 PP.

Marshak, A. and A. Davis, 2005: 3d radiative transfer in cloudy atmospheres. *PHYSICS OF EARTH AND SPACE ENVIRONMENTS*.

Meyer, S., 2006: Einfluss der Wolkenstruktur auf die reflektierte solare Strahldichte inhomogener Bewölkung. *Dissertation am IFM-GEOMAR der Universität Kiel*.

Mie, G., 1908: Beiträge zur optik trüber medien, speziell kolloidaler metallösungen. *Annalen der Physik*, **330**(3), 377–445.

Moulin, C. and I. Chiapello, 2004: Evidence of the control of summer atmospheric transport of african dust over the atlantic by sahel sources from toms satellites (1979–2000). *Geophysical Research Letters*, **31**, 4 PP.

Otto, S., E. Bierwirth, B. Weinzierl, K. Kandler, M. Esselborn, M. Tesche, A. Schladitz, M. Wendisch, and T. Trautmann, 2009: Solar radiative effects of a saharan dust plume observed during samum assuming spheroidal model particles. *Tellus B*, **61**(1), 270–296.

Pope, C. A., 2000: Review: Epidemiological basis for particulate air pollution health standards. *Aerosol Science and Technology*, **32**(1), 4–14.

Prospero, J. M., 1999: Long-range transport of mineral dust in the global atmosphere: Impact of african dust on the environment of the southeastern united states. *Proceedings of the National Academy of Sciences*, **96**(7), 3396–3403.

Prospero, J. M. and P. J. Lamb, 2003: African droughts and dust transport to the caribbean: Climate change implications. *Science*, **302**(5647), 1024–1027.

Rosenfeld, D., Y. Rudich, and R. Lahav, 2001: Desert dust suppressing precipitation: A possible desertification feedback loop. *Proceedings of the National Academy of Sciences*, **98**(11), 5975–5980.

Scheirer, R., 2001: Solarer strahlungstransport in der inhomogenen atmosphäre. *Berichte aus dem Institut für Meereskunde an der Universität Kiel*, (322).

Schepanski, K., I. Tegen, B. Laurent, B. Heinold, and A. Macke, 2007: A new saharan dust source activation frequency map derived from msg-seviri ir-channels. *Geophysical Research Letters*, **34**, L18803.

Schepanski, K., I. Tegen, and A. Macke, 2009: Saharan dust transport and deposition towards the tropical northern atlantic. *Atmospheric Chemistry and Physics*, **9**(4), 1173–1189.

Schewski, M., 2006: Photonenweglängen in konvektiver bewölkung unter berücksichtigung der räumlichen wolkeninhomogenität. *Dissertation am IFM-GEOMAR*.

Schmetz, J., Y. Govaerts, M. König, H.-J. Lutz, A. Ratier, and S. Tjemkes, 2011: A short introduction to meteosat second generation (msg). *EUMETSAT*.

Schmidt, K., J. Wauer, T. Rother, and T. Trautmann, 2009: Scattering database for spheroidal particles. *Appl. Opt.*, **48**(11), 2154–2164.

Schuster, M., P. Duringer, J.-F. Ghienne, P. Vignaud, H. T. Mackaye, A. Likius, and M. Brunet, 2006: The age of the sahara desert. *Science*, **311**(5762), 821.

Shao, Y., K.-H. Wyrwoll, A. Chappell, J. Huang, Z. Lin, G. H. McTainsh, M. Mikami, T. Y. Tanaka, X. Wang, and S. Yoon, 2011: Dust cycle: An emerging core theme in earth system science. *Aeolian Research*, **In Press, Corrected Proof**.

Sokolik, I. N., 2002: The spectral radiative signature of wind-blown mineral dust: Implications for remote sensing in the thermal ir region. *Geophysical Research Letters*, **29**(24), 2154.

Sokolik, I. N. and O. B. Toon, 1999: Incorporation of mineralogical composition into models of the radiative properties of mineral aerosol from uv to ir wavelengths. *Journal of Geophysical Research*, **104**(D8), 9423–9444.

Solmon, F., M. Mallet, N. Elguindi, F. Giorgi, A. Zakey, and A. Konaré, 2008: Dust aerosol impact on regional precipitation over western africa, mechanisms and sensitivity to absorption properties. *Geophysical Research Letters*, **35**.

Solomon, S., D. Qin, M. Manning, Z. Chen, M. Marquis, K. Averyt, M. Tignor, and H. Miller, 2007: Contribution of working group i to the fourth assessment report of the intergovernmental panel on climate change. *Cambridge University Press, Cambridge, United Kingdom and New York, NY, USA,*, p. 996 pp.

Stamnes, K. and R. A. Swanson, 1981: A new look at the discrete ordinate method for radiative transfer calculations in anisotropically scattering atmospheres. *Journal of Atmospheric Sciences*, **38**, 387–399.

Tanaka, T. Y. and M. Chiba, 2006: A numerical study of the contributions of dust source regions to the global dust budget. *Global and Planetary Change*, **52**(1-4), 88 – 104. Monitoring and Modelling of Asian Dust Storms.

Tegen, I., 2003: Modeling the mineral dust aerosol cycle in the climate system. *Quaternary Science Reviews*, **22**(18-19), 1821 – 1834. Loess and the Dust Indicators and Records of Terrestrial and Marine Palaeoenvironments (DIRTMAP) database.

Tegen, I., S. P. Harrison, K. Kohfeld, I. C. Prentice, M. Coe, and M. Heimann, 2002: Impact of vegetation and preferential source areas on global dust aerosol: Results from a model study. *Journal of Geophysical Research*, **107**(D21), 4576.

Tegen, I., A. A. Lacis, and I. Fung, 1996: The influence on climate forcing of mineral aerosols from disturbed soils. *Nature*, **380**, 419–422.

Thomas, G. E. and K. Stamnes, 1999: *Radiative Transfer in the Atmosphere and Ocean (Cambridge Atmospheric and Space Science Series)*, volume Reprint (28. Januar 2002). ISBN ISBN-10: 0521890616.

Timo and Nousiainen, 2009: Optical modeling of mineral dust particles: A review. *Journal of Quantitative Spectroscopy and Radiative Transfer*, **110**(14-16), 1261 – 1279. <ce:title>XI Conference on Electromagnetic and Light Scattering by Non-Spherical Particles: 2008</ce:title>.

Torge, A., A. Macke, B. Heinold, and J. Wauer, 2011: solar radiative transfer simulations in saharan dust plumes: Particle shapes and 3-d effect. *Tellus B*, **63**(4), 770–780.

van de Hulst, H. C., 1958: Light scattering by small particles. by h. c. van de hulst. new york (john wiley and sons), london (chapman and hall), 1957. pp. xiii, 470; 103 figs.; 46 tables. 96s. *Quarterly Journal of the Royal Meteorological Society*, **84**(360), 198–199.

Voiland, A. and R. Simmon, 2010: Aerosols: Tiny particles, big impact.

Volten, H., O. Muñoz, J. Hovenier, and L. Waters, 2006: An update of the amsterdam light scattering database. *Journal of Quantitative Spectroscopy and Radiative Transfer*, **100**(1-3), 437 – 443. <ce:title>VIII Conference on Electromagnetic and Light Scattering by Nonspherical Particles</ce:title> <xocs:full-name>VIII Conference on Electromagnetic and Light Scattering by Nonspherical Particles</xocs:full-name>.

Volten, H., O. Muñoz, E. Rol, J. de Haan, W. Vassen, J. Hovenier, K. Muinonen, and T. Nousiainen, 2001: Scattering matrices of mineral aerosol particles at 441.6 nm and 632.8 nm. *Journal of Geophysical Research*, **106**(D15), 17375–17401.

Wald, A. E., Y. J. Kaufman, D. Tanré, and B.-C. Gao, 1998: Daytime and nighttime detection of mineral dust over desert using infrared spectral contrast. *Journal of Geophysical Research*, **103**(D24), 32,307–32,313.

Wauer, J., K. Schmidt, T. Rother, T. Ernst, and M. Hess, 2004: Two software tools for plane-wave scattering on nonspherical particles in the german aerospace center's virtual laboratory. *Appl. Opt.*, **43**(35), 6371–6379.

Yang, P., Q. Feng, G. Hong, G. W. Kattawar, W. J. Wiscombe, M. I. Mishchenko, O. Dubovik, I. Laszlo, and I. N. Sokolik, 2007: Modeling of the scattering and radiative properties of nonspherical dust-like aerosols. *Journal of Aerosol Science*, **38**(10), 995 – 1014.

Zdunkowski, W. G. and G. Korb, 1974: An approximate method for the determination of short-wave radiative fluxes in scattering and absorbing media (application to solar radiation in earth atmosphere). *Beitraege zur Physik der Atmosphaere*, **47**(2), 129–144.

9 Erklärung

Hiermit bestätige ich, dass ich die vorliegende Dissertation selbstständig verfasst und keine anderen als die angegebenen Quellen und Hilfsmittel verwendet habe. Ich versichere, dass diese Arbeit noch nicht zur Erlangung eines Doktorgrades an anderer Stelle vorgelegen hat. Ich erkläre, dass die vorliegende Arbeit gemäß der Grundsätze zur Sicherung guter wissenschaftlicher Praxis der Deutschen Forschungsgemeinschaft erstellt wurde.

Kiel, Februar 2013 Antje Torge